AD A124725

DTIC
ELECTE
FEB 2 3 1983
S D
E

DEPARTMENT OF THE AIR FORCE

AIR UNIVERSITY (ATC)

AIR FORCE INSTITUTE OF TECHNOLOGY

Wright-Patterson Air Force Base, Ohio

DTIC FILE COPY

This document has been approved for public release and sale; its distribution is unlimited.

83 02 022 097

AFIT/GE/EE/82D-70

A124725

DUAL-SEEKER MEASUREMENT PROCESSING FOR TACTICAL MISSILE GUIDANCE

THESIS

AFIT/GE/EE/82D-70 Andrew C. Weston
2Lt USAF

Approved for public release; distribution unlimited

DTIC
SELECTED
E

AFIT/GE/EE/82D-70

DUAL-SEEKER MEASUREMENT PROCESSING FOR TACTICAL MISSILE GUIDANCE

THESIS

Presented to the Faculty of the School of Engineering
of the Air Force Institute of Technology
Air University
in Partial Fulfillment of the
Requirements for the Degree of
Master of Science in
Electrical Engineering

Accession For
NTIS GRA&I [X]
DTIC TAB [ ]
Unannounced [ ]
Justification
By
Distribution/
Availability Codes
Dist | Avail and/or Special
A

By

Andrew C. Weston, BSEE
2Lt USAF

December 1982

DTIC COPY INSPECTED 2

Approved for Public Release; Distribution Unlimited

Acknowledgements

This thesis has been perhaps the most challenging task I have ever faced. Understanding the theory involved; putting the necessary work into the programming, analysis, and writing; and maintaining the required interest and motivation all seemed impossible at times and were, in reality, beyond my capabilities alone. I recognize, and am profoundly grateful for, the strength I have received and the love I have felt from the Lord my God, the Father, Son, and Holy Spirit. Without His help, I could never have completed this thesis.

I also wish to extend my thanks to my advisor, Ltc Robert Edwards, for his patience and understanding throughout this project, and to my other committee members, Dr. Peter Maybeck and Capt Aaron Dewispelare, for their time and support. Thanks also goes to my sponsor, Mr. Phil Richter of the Armament Laboratory, Eglin AFB, for providing this interesting topic and his support. I am also very grateful to Mr. Stan Musick of the Avionics Laboratory, Wright-Patterson AFB, and to Mr. Marshall Watson and Lt Scott Trimbali of the Armament Lab for their invaluable help on the software for this project.

I also want to extend special thanks and recognition to some very important people. Capts Hank Worsley and

Don Stiffler gave me immeasurable help during some of the hardest times. They provided practical guidance and helped me gain the insight that I needed, and I know that I could not have achieved the satisfaction I feel towards this thesis without them. They also provided inspiration and encouragement when I needed it most. I will always be indebted to them. I am also very appreciative of the counsel of Capts Dave Wilson and Sam Barr who were always open and helpful to me, while doing their own work on a related subject. Thanks goes to Lt Al Moseley for his support and friendship. My typist, Mrs. Sheila Finch, put in many long, trying hours on this work, was always understanding, and was very concerned about the quality of the finished product. I extend my special thanks to her.

Finally, I want to express my gratitude to my fiancee, Miss Rita Bachman. Her love and understanding have been a lamp of inspiration and strength, and the light of her caring and concern is very much a part of this thesis work.

Contents

		Page
Acknowledgements		i
List of Figures		v
List of Tables		vii
List of Symbols		viii
Abstract		x
I.	Introduction	1
	Background	1
	Theory	2
	Statement of Problem and Objectives	8
	Assumptions	9
	Organization	9
II.	Truth Model	11
	Introduction	11
	Assumptions	11
	Missile Model	12
	Measurement Model	20
	Strapdown Seeker Model	23
	Gimballed Seeker Model	33
	Truth State Model	39
III.	Kalman Filter Design	46
	Introduction	46
	Filter Equations	47
	EKF Design	50
	EKF Noise Strengths and Initial Conditions	55
IV.	Model Implementation/Method of Evaluation	59
	Introduction	59
	Software Implementation	59
	Filter Tuning	64
	Method of Evaluation	69
V.	Results	76
	Introduction	76
	General Performance of the Filter	76
	Measurement Policy Comparisons	80
	Summary	84

Contents

	Page
VI. Conclusions and Recommendations	85
Introduction	85
Conclusions	85
Recommendations	87
Bibliography	88
Appendix A: Calculating LOS Angles	91
Appendix B: Filter Measurement Matrix	93
Appendix C: Filter Tuning Plots	98
Appendix D: Plots for the Results	135
VITA	160

List of Figures

Figure		Page
1-1	Basic Gimballed Seeker	4
1-2	Basic Types of Strapdown Seekers	6
2-1	Earth-Fixed Frame	13
2-2	LLLGB Simulation Missile Flight Path	14
2-3	Body-Fixed Frame	15
2-4	Missile Body Dynamics	17
2-5	LOS Frame and Azimuth and Elevation Angles . .	21
2-6	Strapdown Seeker Model	24
2-7	Strapdown Seeker -- Radome Geometry	28
2-8	Effect of Radome Distortion on Strapdown Seeker	29
2-9	Strapdown Seeker Block Diagram	32
2-10	Gimballed Seeker Model	34
2-11	Gimballed Seeker Dynamics	35
2-12	Gimballed Seeker -- Radome Geometry	37
2-13a	Gimballed Seeker Block Diagram	40
2-13b	Gimballed Seeker Radome Distortion Block Diagram	41
4-1	Sample SOFEPL Plot	60
C-1 to C-6	Both Seekers, Initial Tuning Plots	99 to 104
C-7	Both Seekers, 50 Runs	105
C-8	Both Seekers, Different Seed for Random Number Generator	106
C-9 to C-14	Strapdown Seeker Only, $R_1 = .00125$ rad^2	107 to 112

List of Figures

Figure		Page
C-15	Strapdown Seeker Only, R_1=.0028 rad^2	113
C-16 to C-21	Gimballed Seeker, Angle Only, R_3=.00125 rad^2	114 to 119
C-22	Gimballed Seeker, Angle Only, R_3=.00556 rad^2	120
C-23 to C-28	Gimballed Seeker, Angle-Rate Only, R_5=.00125 rad^2	121 to 126
C-29 to C-34	Gimballed Seeker, Angle-Rate Only, R_5=.0078 rad^2	127 to 132
C-35 to C-36	Gimballed Seeker, Angle-Rate Only, R_5=.01125 rad^2	133 to 134
D-1 to D-6	Both Seekers Throughout Flight	136 to 141
D-7 to D-12	Strapdown Only Initially, Switch to Gimballed at 16 sec	142 to 147
D-13 to D-18	Both Seekers Initially, Strapdown Off at 16 sec	148 to 153
D-19 to D-24	Strapdown Only Initially, Gimballed On at 16 sec	154 to 159

List of Tables

Table		Page
I.	Statistics of Strapdown Seeker Truth Model Noises	31
II.	Statistics of Gimballed Seeker Truth Model Noises	39
III.	Measurement Policies	71
IV.	Statistics of Plots for the Results	77

List of Symbols

Symbol	Description
α	azimuth angle
b	denotes body-fixed frame, also boresight error truth state
C_A^B	coordinate transformation matrix from frame A to frame B
c	cross-coupling error truth state
e	denotes earth-fixed frame
EKF	extended Kalman filter
ϵ	elevation angle, also seeker error angle for planar radome geometry
f	refers to filter
$\underline{f}$	EKF dynamics vector
g	glint truth state, also refers to gimballed seeker
$\underline{h}$	measurement vector in terms of filter states
$\underline{H}$	EKF measurement matrix
L	denotes LOS frame
LOS	line-of-sight
m	denotes inertially-stabilized missile frame
$\underline{P}$	EKF covariance matrix
$\underline{P}_0$	covariance of filter state initial conditions
ϕ	roll angle
ψ	yaw angle
ψ_s	inertially-referenced seeker azimuth angle
$\underline{Q}$	driving noise strength matrix
$\underline{R}$	measurement noise strength matrix

List of Symbols

Symbol	Description
s	scale factor error truth state, also refers to strapdown seeker, also to truth model
σ	standard deviation
t	time
t_i	discrete-time instant
τ	time constant
θ	pitch angle, also inertially-referenced LOS angle for planar radome geometry
θ_m	inertially-referenced missile angle for planar radome geometry
θ_r	radome distortion angle
θ_s	inertially-referenced seeker elevation angle
$\underline{u}$	deterministic forcing function in EKF dynamics
$\underline{v}$	zero-mean white measurement noise vector
v_x, v_y, v_z	velocity states in x, y, and z directions
$\underline{w}$	zero-mean white driving noise vector
x, y, z	position states
$\underline{x}$	state vector
$\underline{z}$	truth measurement vector

Abstract

The available measurements from a strapdown seeker and a gimballed seeker onboard an air-to-ground anti-radiation missile are analyzed through an extended Kalman filter simulation. Detailed models of both seekers are developed. Only angular measurements are assumed available from the seekers: angle measurements from the strapdown seeker and angle and angle-rate measurements from the gimballed seeker. A 6-state extended Kalman filter model is used to estimate the ground target's position and relative velocity using the seekers' measurements. Four measurement policies are compared to analyze use of the gimballed seeker early in the missile flight and loss of the strapdown seeker in midflight.

The results revealed an observability problem in one channel of the filter, that along the range vector. Analyses were made only by comparisons of performance in the other two channels. The comparisons showed insignificant degradation to filter performance through loss of the strapdown seeker at midflight, and substantial benefit from use of the gimballed seeker as early as possible in the flight.

DUAL-SEEKER MEASUREMENT PROCESSING FOR TACTICAL MISSILE GUIDANCE

I. INTRODUCTION

Background

The air-to-ground anti-radiation missile, or ARM, is a weapon typically intended for use against active enemy radar sites. Guidance for the ARM after launch is dependent upon a seeker which provides information about the relative position of the target with respect to the missile. The seeker information may be supplemented by other information such as missile inertial accelerations from an inertial measuring unit (IMU). Present anti-radiation missiles, such as the AGM-45A Shrike and the AGM-78 Standard ARM, employ passive radar seekers to provide guidance information. Since a passive radar seeker relies solely on target emissions for successful operation, an inherent problem in present anti-radiation missiles is target emitter shutdown.

A possible solution to the emitter shutdown problem is the use of two separate seekers, one of which is semi-active or passive electro-optical and, therefore, not dependent on radar emissions from the target. One such dual-seeker configuration under consideration by the Air Force Armament Test Laboratories (AFATL), Eglin AFB,

Florida, is a body-fixed, or strapdown, passive radar seeker installed on an AGM-65 Maverick missile. The AGM-65 missiles are already equipped with a gimballed seeker that is either passive television, passive infrared, or semi-active laser. The concept of employing a strapdown seeker for missile guidance is relatively new. At present, strapdown seeker guidance is being explored at AFATL and has only been implemented in the limited case of an anti-ship missile (Ref 10). If the dual-seeker missile were to be implemented, a major design consideration is how to use the information from both seekers. The motivation for this thesis is to explore the possibilities in guidance transition between the two seekers.

Theory

The major difference between gimballed and strapdown seekers is that the information provided mechanically by a gimballed seeker is derived electronically in a strapdown seeker. Such information may be the azimuth and elevation angles of the line-of-sight (LOS) to the target, the rates of change of these angles, target range, and target range-rate. The other important difference is the coordinate frame to which the information is referenced. To implement most guidance techniques, inertially referenced angle information is necessary. Further explanation of the operation of gimballed and strapdown seekers will clarify the importance of their differences.

A gimballed seeker is characterized by the ability to rotate its sensitive axis with respect to the missile. This rotation is typically about two gimbals which are rotated by torquer motors to keep the seeker antenna centerline on the LOS to the target. The LOS can then be quantitized by potentiometer measurements of the two gimbal angles. Inertially-referenced azimuth and elevation angle rates can be measured directly from rate gyroscopes on the inner gimbal.

The basic gimballed seeker is depicted in Figure 1-1. As shown in the figure, the instantaneous field of view (FOV) is the angular region about the seeker boresight from which it receives usable energy. The total FOV is the region swept out by the instantaneous FOV as the gimbals are rotated to their limits.

A strapdown seeker, on the other hand, is fixed to the body of the missile. Such a seeker operates by electronically measuring the LOS angles with respect to the missile body and, possibly, the range and/or range-rate to the target. Inertial LOS rates cannot be measured directly from a strapdown seeker. Theoretically, LOS rates can be derived from LOS angles and body rate-gyro outputs, but usually a derivative network is involved, leading to stability problems (Ref 8:1). This fact is an inherent problem in strapdown seeker guidance and will be discussed further.

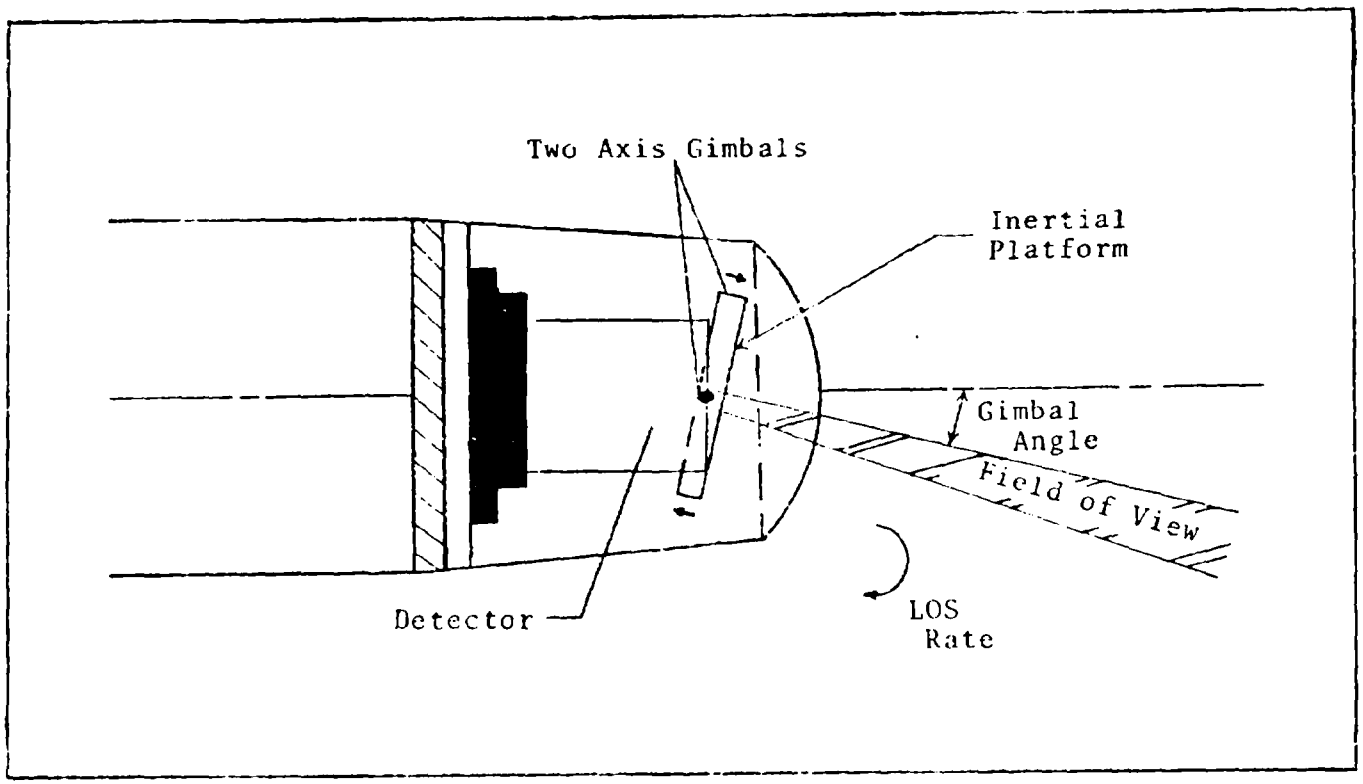

Figure 1-1. Basic Gimballed Seeker (Ref 12)

There are two basic types of strapdown seekers: "staring" and "beam steered." Sketches of these are presented in Figure 1-2. The beam steered is like a gimballed seeker in that it has a small instantaneous FOV which can be moved relative to the missile body. An active radar seeker with phased array antenna is an example of beam steering. The staring type has an instantaneous FOV equal to the total FOV. An example of a staring strapdown seeker is the semi-active laser seeker with a wide FOV. Another kind of strapdown seeker that has been investigated is the "multiarm flat spiral antenna" interferometer seeker (Refs 10;13).

Since the missile concept explored in this thesis is an ARM equipped with both a strapdown passive radar seeker and a gimballed passive electro-optical or semi-active laser, the specific information available from these seekers must be specified. Active or semi-active radar seekers are the only ones which currently provide missile-to-target range and/or range rate (Ref 12:3-4). Since neither seeker considered here is active or semi-active radar, range and range-rate are not considered available from either. As discussed earlier, the gimballed seeker is capable of providing direct measurements of LOS angles and inertially-referenced angle-rates. Therefore, this information is assumed available from the gimballed seeker. Although work has been done towards deriving LOS angle-rates from the LOS angle measurements of a strapdown

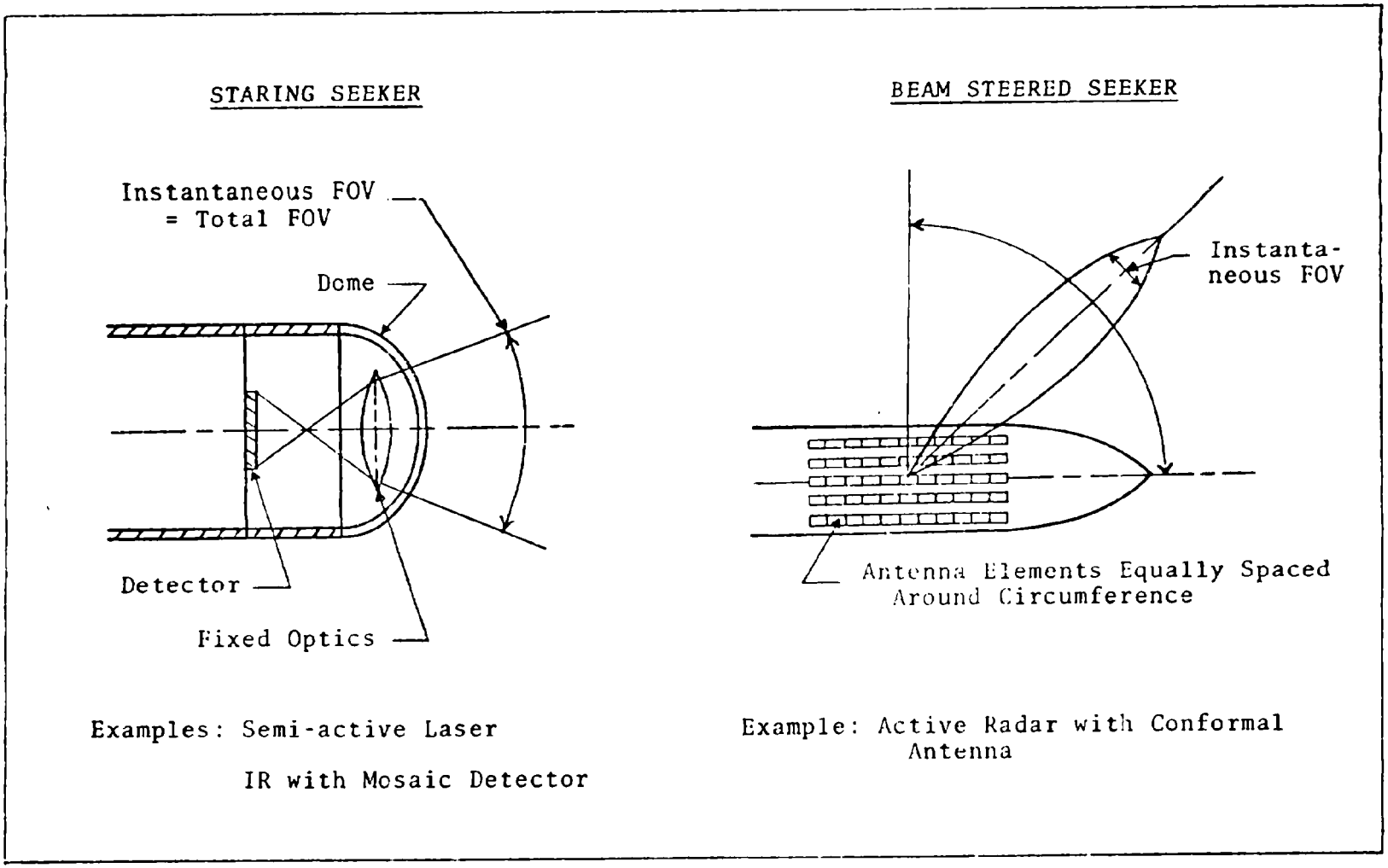

Figure 1-2. Basic Types of Strapdown Seekers (Ref 6)

seeker (Refs 6;8), the methods explored are still not fully developed or tested. For this reason, only the LOS angles directly measured by the strapdown seeker are assumed to be available from it. Through the course of this study, however, if the lack of angle-rate measurements from the strapdown seeker prevents a realistic analysis of the two seekers, pseudo angle-rate measurements may be considered for the strapdown seeker model.

The dual seeker missile proposed by AFATL would have inherent flexibility, but the guidance information available to it at any given time during flight would be constrained by the limitations of both seekers. Typically, a radar seeker would be capable of acquiring the target at longer ranges than an optical seeker. Again, however, the radar seeker may lose track due to target emitter shutdown, so that the missile would then have to depend on the information from the optical seeker. Depending on the trajectory, the optical seeker may acquire the target at launch or not until midflight. Therefore, the information available is a function of range-to-target and detection of the approaching missile by the target. Conceptually, the measurement policies to be examined are:

1) both seekers operative throughout flight.

2) strapdown only initially, switch on gimballed at time of target shutdown.

3) both seekers initially, loss of strapdown at time of target shutdown.

4) strapdown only initially, both seekers when gimballed acquires target.

To accomplish this study, some means of simulating the use of the guidance information available must be developed. A Kalman filter implementation was chosen because of its ability to use all the information available to it and to weight the information according to the confidence afforded it. Also, Kalman filters have been used successfully in numerous missile guidance applications (Refs 3;5;14;17;25). The specific Kalman filter chosen for this study and the rationale for this choice will be discussed in Chapter III. Given the preceding development of the motivation for this study, the theory involved, and a means for achieving the desired comparisons, the specific problem and objectives of this thesis can now be presented.

Statement of Problem and Objectives

The bulk of the work done for this thesis was in the development of adequate models for the seekers involved and in incorporating these models into a working filter design. The goal was to implement a simulation on a digital computer to perform the desired analyses of the dual-seeker measurement policies given in the preceding section. The objectives of this thesis can be summarized as follows:

1) Develop detailed "truth" models of the missile and the two seekers.

2) Develop a tractable reduced order Kalman filter design to use the measurements available from the seeker models.

3) Run analyses of the proposed dual-seeker measurement policies using this filter design.

4) Discuss the results of the above three.

Assumptions

The maximum time of flight of the missile simulated in this thesis is approximately 28 seconds. For this relatively short time of flight, an earth-fixed navigation frame was assumed to be essentially inertial. Such a frame consists of three axes, typically in north, east, and down directions, and is fixed at a point on the surface of the earth. For the accelerations involved in this study, an analysis of this assumption, using nominal values of range and missile velocity and acceleration, showed that it introduced an inertial acceleration error of, at most, four percent. This small error is assumed to be negligible in the comparison of the two seekers since they are mounted together on the same missile and since their relative errors are much larger.

In order to concentrate the major effort of this thesis on the seeker models and filter design, an inertial navigation system (INS) is assumed to provide nearly perfect inertial accelerations of the missile and perfect Euler angles between the missile body frame and the local level frame. Hence, an error model of the INS is not employed in this thesis beyond that of white Gaussian noise modelling the error in the INS accelerations.

Organization

Chapter II of this thesis is the explanation of the missile model employed and the development of the two seeker truth models. Chapter III presents the Kalman

filter theory for the specific filter used and the filter design. Chapter IV is a discussion of the method used for implementing the filter and truth models and for evaluating the performance of the filter for the proposed measurement policies. Chapter V presents the results of the analyses, and Chapter VI summarizes this work with conclusions drawn from the results and with recommendations for future study. The appendices include the development of the detailed mathematics of the truth model and filter implementation and the graphs depicting the results of the analyses.

II. TRUTH MODEL

Introduction

A truth model is the best mathematical model of the systems involved in problem of interest, given knowledge of their operation in the "real world." It is developed to provide a baseline for the Kalman filter design and a model against which the filter can be run. The particular truth model used in this thesis is based on an air-to-ground missile flight simulation provided by AFATL, the Low-Level Laser-Guided Bomb (LLLGB) program (Ref 16). The LLLGB output used is a detailed computer simulation of a typical non-thrusting, guided air-to-ground missile run. It provides missile position, velocity, and acceleration with respect to an earth-fixed inertial frame and Euler angles and angle-rates of the missile with respect to the local, noninertially rotating frame. The use of this simulation as a missile truth model and as input to the seeker models is facilitated by making the following assumptions.

Assumptions

Since the target is earth-fixed, it will be assumed to be located at the origin used in the LLLGB simulation. Therefore, measurements which are functions of the relative position and velocity of the target with respect to the missile are also functions of the inertial position and

velocity of the missile. The seekers are assumed to be located at the same point on the missile, the missile's center of gravity, in order to simplify the measurement equations. The seekers are assumed to operate independently and not to influence the missile trajectory. In other words, the seekers will only provide measurements to the filter algorithm and are not in the closed loop of the missile's true dynamics. Inclusion of the seekers in a closed loop guidance law is a considerably more complex study. Since the development of good seeker models and the implementation of the filter design presented a distinct challenge in themselves, such a guidance law study was not attempted for this thesis.

Missile Model

As stated previously, the missile model is defined as the one used in the LLLGB simulation. In this program, the earth-fixed coordinate frame is defined by the missile release conditions as shown in Figure 2-1. The x_e-axis is parallel to the initial velocity vector in the earth frame. The x_e-y_e plane is tangent to the earth plane, and the z_e-axis points to the center of the earth. As explained in the assumptions section of Chapter I, this earth-fixed frame is considered to be the inertial frame in this thesis and will be referred to as the inertial frame from now on. The missile flies from initial release conditions of (-20000., 0., -500.) ft at an initial velocity vector of

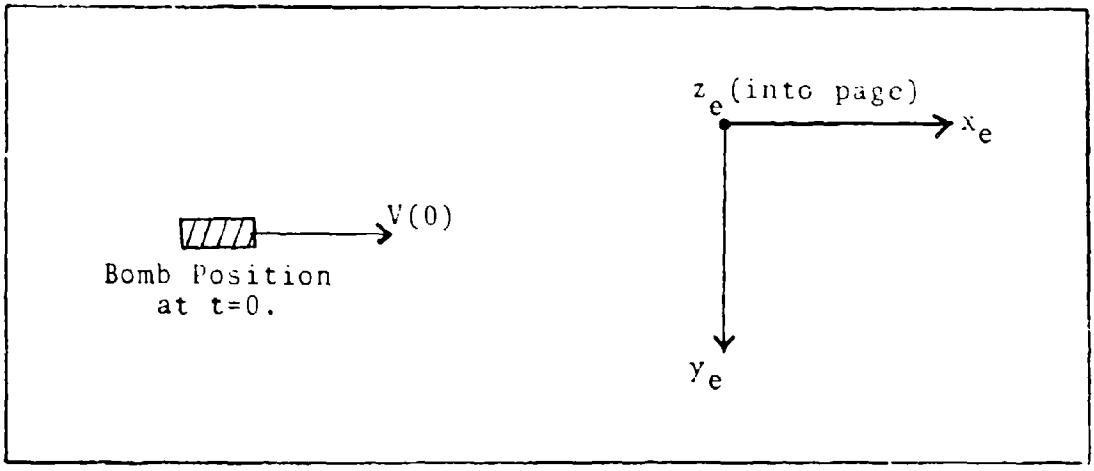

Figure 2-1. Earth-Fixed Frame

(843.9, 0., 0.) ft/sec (about Mach 0.75 in the x_e -direction) to a point at a slantrange of 529.8 ft to the earth-frame origin, with less than one second left until impact. The dominant motion of the missile is in the x_e-z_e plane, the largest deviation in the y_e -direction being 45 ft. A plot of the missile flight path in the x_e -z_e plane is found in Figure 2-2. The trajectory was terminated short of impact because the final conditions of the simulation are classified. As it is, the simulation run is 28.5 sec long with data points provided every 0.1 sec, which will be the sample period used for this study.

A frame that was not used in the LLLGB simulation but which will be incorporated into this thesis is the missile frame. The origin of the missile frame is located at the

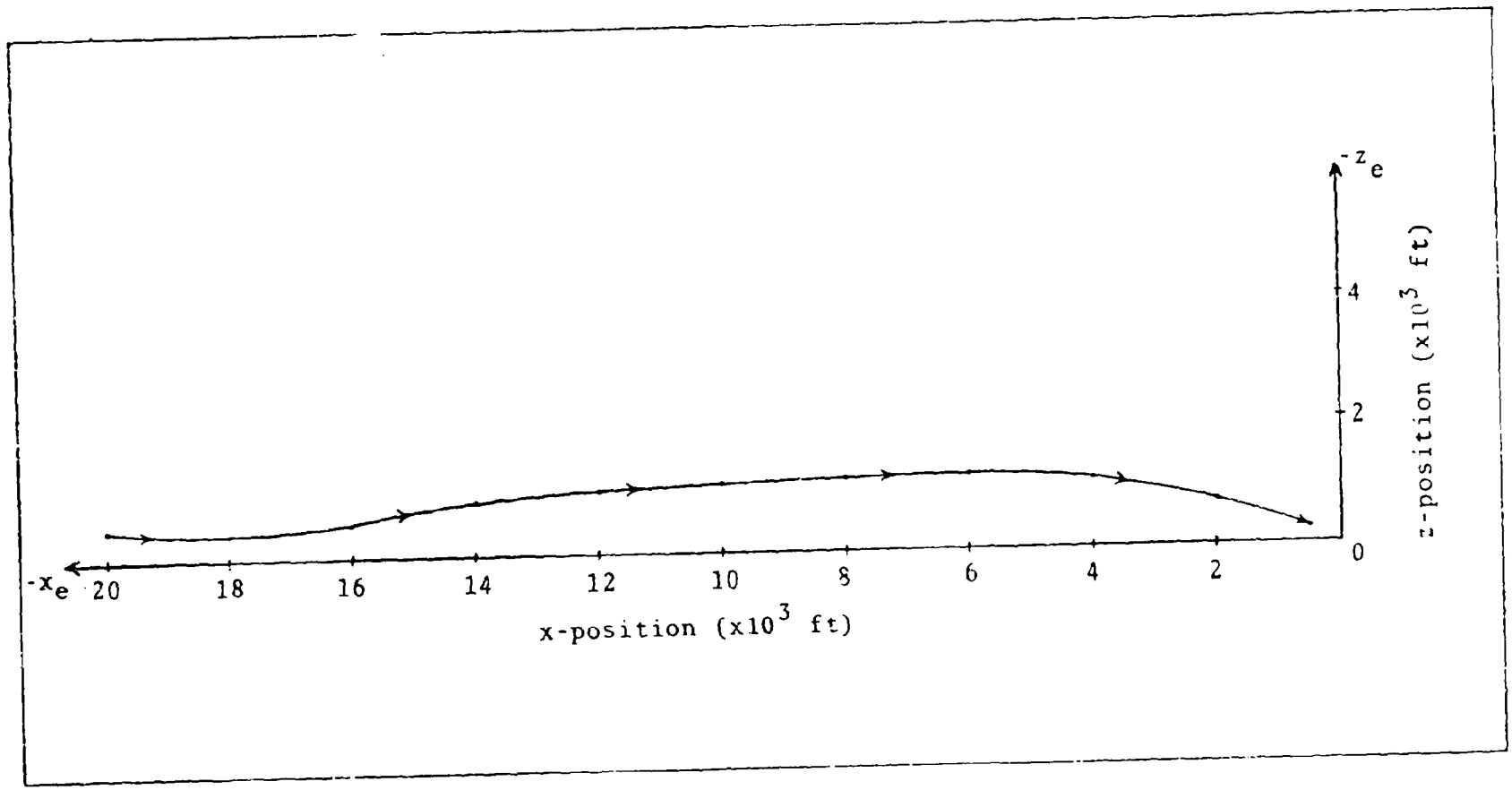

Figure 2-2. LLLGB Simulation Missile Flight Path

center of gravity of the missile, and the frame does not rotate with respect to the inertial frame. The missile frame, therefore, translates with the missile in flight, but its three axes, x_m, y_m, and z_m, are always parallel to the three corresponding inertial axes. The missile frame provides a reference for the next coordinate frame to be discussed, the body frame.

The body-fixed coordinate frame, as used in the LLLGB simulation and in this thesis, is depicted in Figure 2-3.

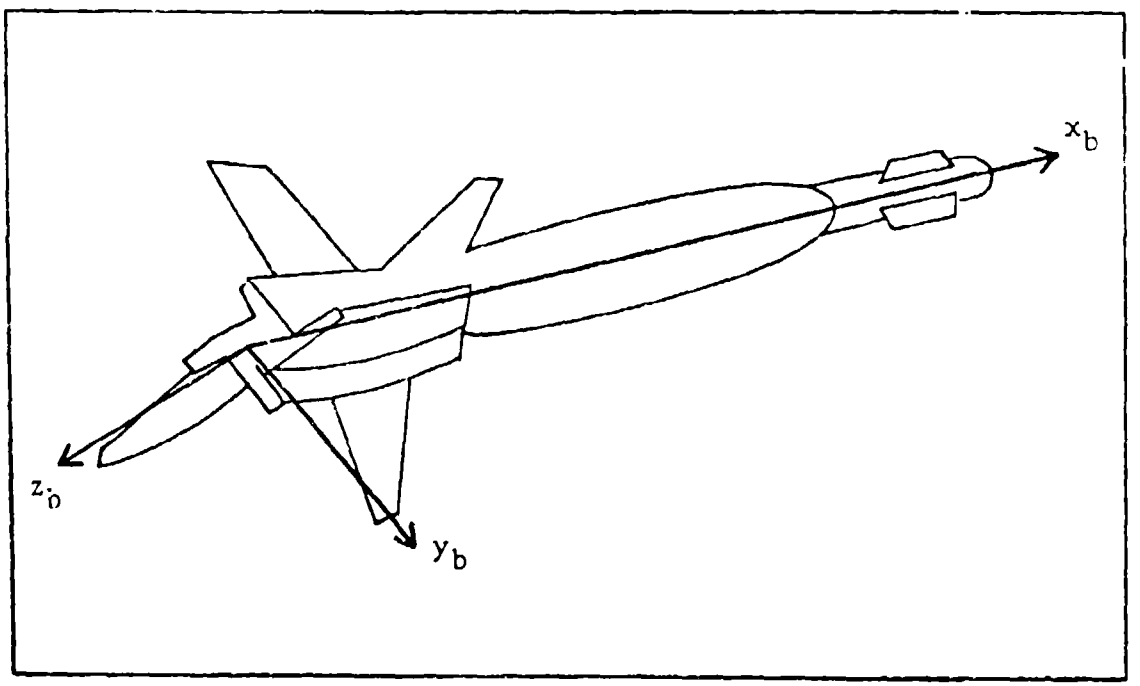

Figure 2-3. Body-Fixed Frame

The body frame also has its origin at the missile center of gravity and translates with respect to the inertial frame,

but rotates with the missile with respect to the inertial and missile frames. In the usual mounting configuration on an airplane in level flight, the y_b and z_b axes make angles of 45° with the x_m-y_m plane.

The missile Euler angles relate the orientation of the body-fixed frame with respect to the missile frame and are defined as θ, ψ, and ϕ for pitch, yaw, and roll. The order of rotation used is pitch, yaw, and roll, so that the transformation matrix from the missile frame is given by

$$\underline{V}^b = \begin{bmatrix} 1 & 0 & 0 \\ 0 & \cos\phi & \sin\phi \\ 0 & -\sin\phi & \cos\phi \end{bmatrix} \begin{bmatrix} \cos\psi & \sin\psi & 0 \\ -\sin\psi & \cos\psi & 0 \\ 0 & 0 & 1 \end{bmatrix} \begin{bmatrix} \cos\theta & 0 & \sin\theta \\ 0 & 1 & 0 \\ -\sin\theta & 0 & \cos\theta \end{bmatrix} \underline{V}^m = C_m^b \underline{V}^m \quad (1)$$

or

$$C_m^b = \begin{bmatrix} \cos\psi\cos\theta & \sin\psi & \cos\psi\sin\theta \\ -\cos\phi\cos\theta\sin\psi - \sin\phi\sin\theta & \cos\phi\cos\psi & \sin\phi\cos\theta - \cos\phi\sin\theta\sin\psi \\ \cos\theta\sin\phi\sin\psi - \cos\phi\sin\theta & -\sin\phi\cos\psi & \cos\phi\cos\theta + \sin\phi\sin\theta\sin\psi \end{bmatrix}$$

where the superscripts indicate the frame in which the vector is written, $\underline{V}$ is any vector in the given frame, and C_m^b is the coordinate transformation matrix from the missile frame to the body frame. The relationship between the three frames discussed thus far is seen in the following diagram.

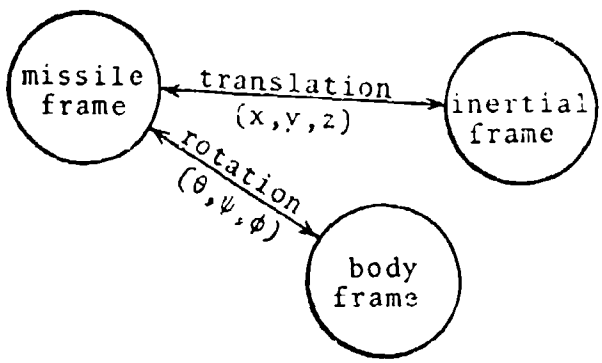

The aerodynamic forces and moments are expressed in the body-fixed frame. The forces are computed as follows:

$$F_x = - Q \cdot S \cdot C_a \quad (2)$$

$$F_y = - Q \cdot S \cdot C_{nb} \quad (3)$$

$$F_z = - Q \cdot S \cdot C_{na} \quad (4)$$

where Q is the dynamic pressure, S is the reference surface area, and C_a, C_{nb}, and C_{na} are the axial force, normal force along y, and normal force along z aerodynamic coefficients, respectively. The subscripts x, y, and z indicate the axis along which the forces are directed.

These forces and the body velocities, accelerations, angular velocities, and angular accelerations are depicted in Figure 2-4. The angular accelerations (derivatives of

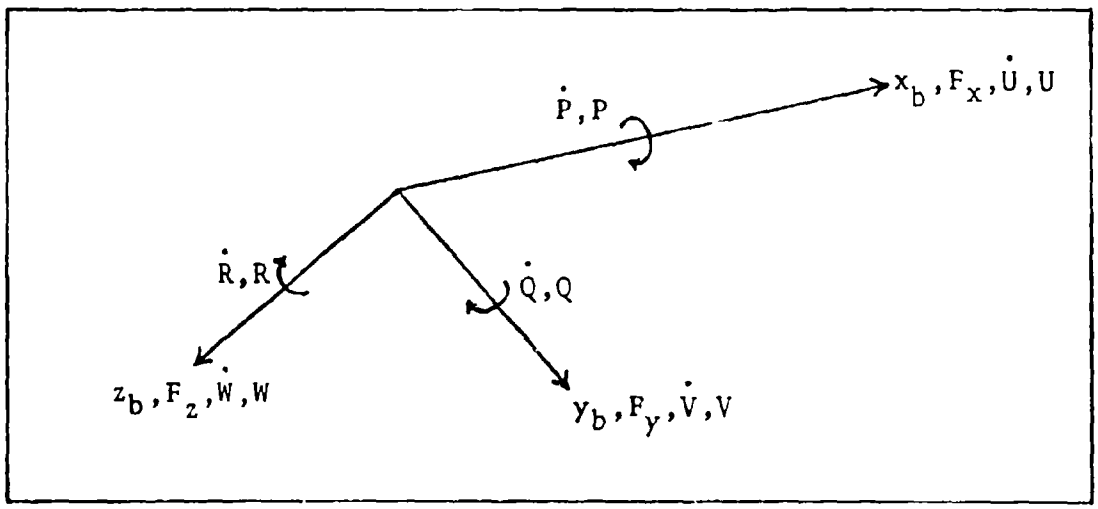

Figure 2-4. Missile Body Dynamics

angular rates P about x_b, Q about y_b, and R about z_b) are

computed by:

$$\dot{P} = M_X / I_X \tag{5}$$

$$\dot{Q} = [M_y - R \cdot P \cdot (I_X - I_o)] / I_o \tag{6}$$

$$\dot{R} = [M_z + P \cdot Q \cdot (I_X - I_o)] / I_o \tag{7}$$

where I_X is moment of inertia about the x_b -axis and I_o is moment of inertia about either the y_b- or z_b- axis. The body moments M_X, M_y, and M_z are given by:

$$M_X = 0 \tag{8}$$

$$M_y = QSD\left[C_{ma}(\alpha, \delta_p) + (C_{m\dot{\alpha}}\dot{\alpha} + C_{m\dot{\theta}}Q)\frac{D}{2V}\right] + F_z \cdot X_{cg} \tag{9}$$

$$M_z = QSD\left[C_{mb}(\beta, \delta_y) + (-C_{m\dot{\alpha}}\dot{\beta} + C_{m\dot{\theta}}R)\frac{D}{2V}\right] - F_y \cdot X_{cg} \tag{10}$$

where D is the reference diameter and X_{cg} is the shift of center of gravity along the x_b -axis. δ_p and δ_y are pitch and yaw canard positions, respectively, and V is the velocity magnitude. The angle of attack, α, and sideslip, β, are given by:

$$\alpha = \tan^{-1}(W/U) \tag{11}$$

$$\beta = \tan^{-1}(V/U) \tag{12}$$

C_{ma} and C_{mb} are the static moment coefficients about y and z, respectively; and $C_{m\dot{\alpha}}$ and $C_{m\dot{\theta}}$ are the dynamic moment coefficients for the rate of change of angle of attack and

for the rate of change of the pitch angle, respectively.

The accelerations in the body frame are computed by the following:

$$\dot{U} = F_{x/m} + (C_i^b)_{13} \cdot g - Q \cdot W + R \cdot V \qquad (13)$$

$$\dot{V} = F_{y/m} + (C_i^b)_{23} \cdot g - R \cdot U + P \cdot W \qquad (14)$$

$$\dot{W} = F_{z/m} + (C_i^b)_{33} \cdot g - P \cdot V + Q \cdot U \qquad (15)$$

where m is the body mass and g is acceleration due to gravity. The rotational velocity terms are due to taking the derivatives in a noninertial reference frame using the theorem of Coriolis. In the simulation, $\dot{U}$, $\dot{V}$, and $\dot{W}$ are integrated using a 4th-order Runge-Kutta method to give U, V, and W which are then rotated to the earth-fixed frame. These inertial velocities are then integrated to give inertial position.

Similarly, $\dot{P}$, $\dot{Q}$, and $\dot{R}$ are integrated to produce P, Q, and R, the angular velocities in the body frame. These are transformed via C_b^m (see eq. (1)) to give $\dot{\theta}$, $\dot{\psi}$, and $\dot{\phi}$, the angular velocities in the inertial frame, which are then integrated to compute the missile's orientation.

In order to understand the equations of motion, the following description of the aerodynamic coefficients is given. The sense of the moment coefficients are such that:

<u>for $\alpha = \beta = 0$</u>

a positive δ_p gives a positive C_{ma}
a positive δ_y gives a positive C_{mb}

for $\delta_p = \delta_y = 0$

a positive α gives a negative C_{ma}
a positive β gives a negative C_{mb}

The sense of the normal force coefficients are such that:

for $\alpha = \beta = 0$

a positive δ_p gives a positive C_{na}
a positive δ_y gives a positive C_{nb}

for $\delta_p = \delta_y = 0$

a positive α gives a positive C_{na}
a positive β gives a positive C_{nb}

$C_{m\dot{\alpha}}$ and $C_{m\dot{\theta}}$ have negative values and are only a function of mach number.

Given the preceding description of the LLLGB simulation, the reader should recognize the complexity of a detailed missile simulation. Using such a simulation made it possible to take advantage of a good missile truth model and yet concentrate most of the original design work on the seeker models. The LLLGB simulation was chosen by the sponsor of this thesis to be a typical trajectory for the conceptual dual-seeker missile. The constant parameters in eqs. (2) through (15) are documented in Ref 7.

Measurement Model

As mentioned in Chapter I, missile seekers provide information about the target relative to the missile. This information can most readily be quantized in the line-of-sight (LOS) frame as depicted in Figure 2-5. In

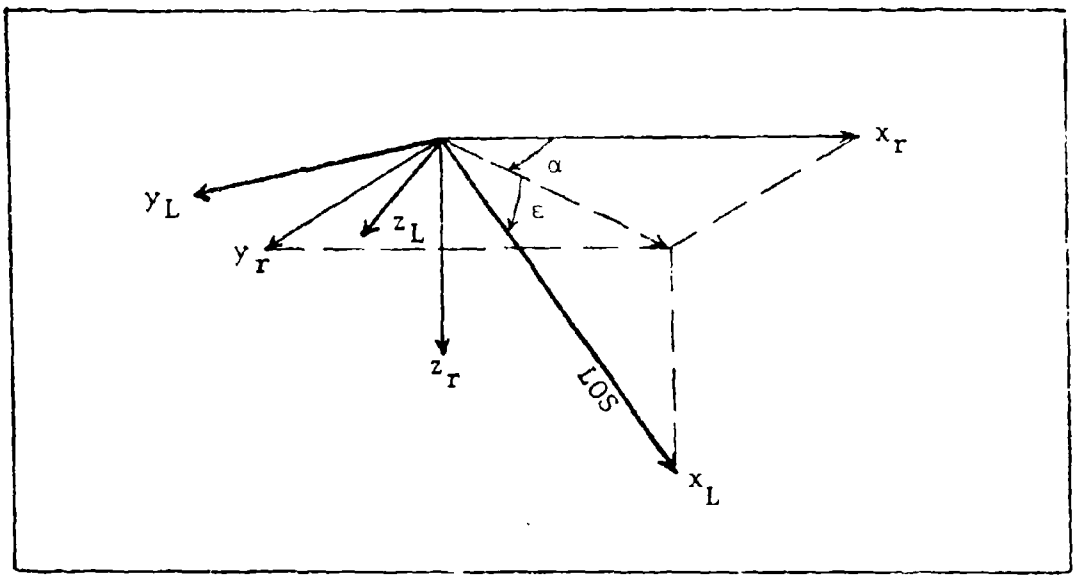

Figure 2-5. LOS Frame and Azimuth and Elevation Angles

the above figure, the subscripts "L" and "r" refer to the LOS frame axes and the axes of some arbitrary reference frame, respectively. The angle α is the azimuth angle of the LOS with respect to the reference frame; ε is the elevation angle* of the LOS with respect to the reference frame. Typically, the reference frame is the missile frame or the body frame, depending on the seeker. The coordinate transformation between the LOS frame and the reference frame is given in Appendix A.

*The knowledgeable reader will note that ε is actually the depression angle. ε was chosen positive as shown to simplify the measurement equations and will be referred to as elevation for simplicity henceforth.

As noted before, some seekers provide both azimuth and elevation angles and azimuth and elevation angle-rates. An active seeker, such as an active radar seeker, provides information about range along the LOS. Since such a seeker is not modelled in this thesis, discussion about measurements is restricted to angular information only.

The azimuth angle, therefore, is defined as the angle between the LOS and its projection into the x_r-z_r plane. Elevation is defined as the angle between the LOS projected into the x_r-z_r plane and the x_r axis. Numerically, the angles are given by the following:

$$\alpha = \tan^{-1}\left[\frac{y_r}{x_r}\right] \tag{16}$$

$$\varepsilon = \tan^{-1}\left[\frac{z_r}{(x_r^2 + y_r^2)^{\frac{1}{2}}}\right] \tag{17}$$

The angle rates can be found by taking the first derivative of eqs. (16) and (17) with respect to time. The resulting azimuth rate and elevation rate are given by the following:

$$\dot{\alpha} = \frac{x_r v_{y_r} - y_r v_{x_r}}{(x_r^2 + y_r^2)} \tag{18}$$

$$\dot{\varepsilon} = \frac{(x_r^2 + y_r^2) v_{z_r} - (x_r v_{x_r} + y_r v_{y_r}) z_r}{(x_r^2 + y_r^2)^{\frac{1}{2}} (x_r^2 + y_r^2 + z_r^2)} \tag{19}$$

where V_{x_r}, V_{y_r}, V_{z_r} are the components of the velocity of the target with respect to the missile in the reference frame.

The relationship between all the frames used in this

thesis is seen in the following diagram.

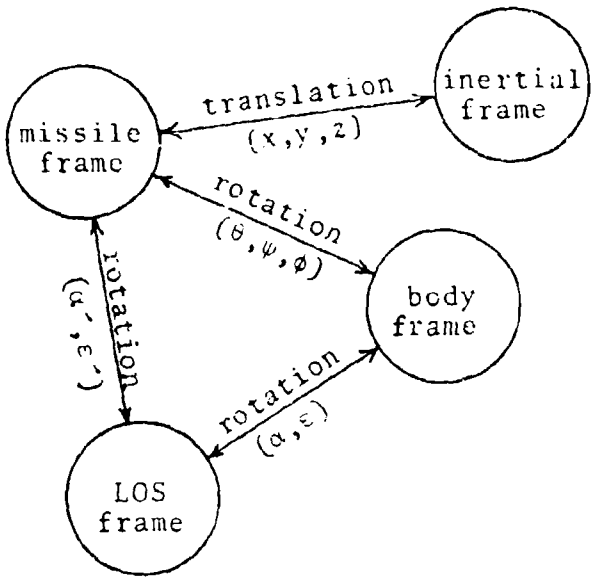

With this description of the measurements, the two seeker models are now developed as parts of the system (overall) truth model.

Strapdown Seeker Model

As discussed previously, one of the seekers modeled in this thesis is a body-fixed passive radar seeker. A model for this seeker was provided by the sponsor at AFATL (Refs 6;8), and is shown in Figure 2-6. This model was developed for a strapdown seeker study done by the Missile Systems Division of Rockwell International for AFATL. It simulates the measurements generated by a strapdown passive radar seeker and the noises which would corrupt such measurements.

The measurements are seen to be derived from the true target position in inertial coordinates. This position is

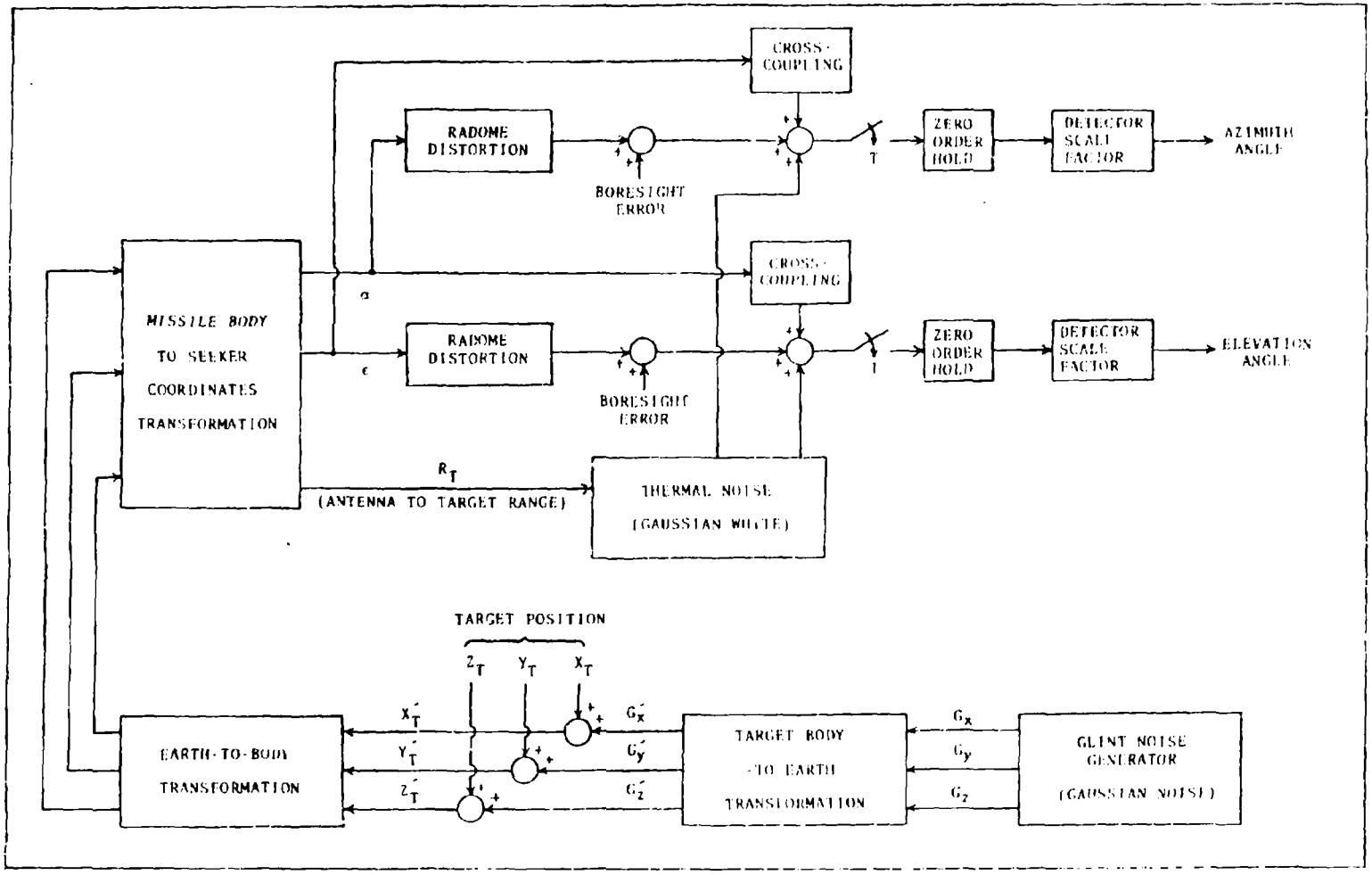

Figure 2-6. Strapdown Seeker Model

first corrupted by additive glint noise, then rotated by an orthogonal transformation to missile-body coordinates. The azimuth and elevation angles of the target with respect to the missile are calculated from the glint-corrupted target position in body coordinates. Finally, two other additive noises: thermal noise and boresight error; and three multiplicative noises: cross-coupling, radome distortion, and detector scale-factor; all corrupt the azimuth and elevation angles. A description of these six noises follows.

Glint Noise. Glint noise has been referred to as "angle scintillation" in previous studies (Refs 5:23; 17:28). Glint noise is the disturbance in apparent angle of arrival of the received signal due to interferences (i.e., phase distortions). Physically, glint can be thought of as wandering of the apparent center of radar signal source. Because of glint noise, the apparent target center may often lie well outside the physical limits of the target (Ref 2). The importance of glint can be easily seen in that a large, abrupt variation in measured radar angle will be interpreted as a change in the angular velocity of the target relative to the missile (Ref 17:28).

Lutter found that a first order Gauss-Markov process provides a good fit to the ensemble statistics of the glint spectrum, the same model used for glint noise in the Rockwell study (Ref 17:28). Modelling glint noise as the

output of a first order lag driven by white Gaussian noise allows for varying target sizes and velocities through the choice of appropriate lag time constant and input noise strength. In general, glint will vary inversely with range and the instantaneous cross section of the target. Since the target is assumed to be a point mass, varying target aspect will not be included in the glint noise. The time constant chosen was 0.1 sec since it was used both by Rockwell and Lutter. The input noise standard deviation was chosen to be 2 ft/sec, the nominal value used by Rockwell.

Thermal Noise. Thermal noise is generated by the background radiation from environmental and receiver effects. Thermal noise varies inversely with signal-to-noise ratio, which in turn varies inversely with range (Ref 17:29). Therefore, thermal noise is directly proportional to range. The model for thermal noise shown in Figure 2-6 is discrete-time white Gaussian noise, which is the typically used model (Ref 17:29). The strength of the thermal noise can be expressed as:

$$\sigma_t^2 = (K \times \text{range})^2 \qquad (20)$$

The coefficient K in eq. (20) was calculated using a nominal value at a given range in (Ref 8:117) and was found to be 1.0×10^{-7} ft^{-1}.

Boresight Error. This noise models the error introducted by calibration inaccuracies in seeker mounting. It can be considered to be constant for any one seeker mounting, so that a good model for boresight error is a random bias. This is the model incorporated in this thesis, and determination of the initial conditions for this and some of the following bias noises came from the Rockwell study. These initial conditions are summarized in Table I following the discussion of the three multiplicative noises.

Radome Distortion. This multiplicative noise must be considered first as it affects the actual energy received by the seeker antenna. Also called aberration error, radome distortion is caused by the protective covering of the antenna. The geometry of the strapdown seeker in one dimension is shown in Figure 2-7. The antenna is assumed to be aligned with the missile body frame so that the seeker centerline is along the x_b-axis. The angle ε represents either the azimuth or elevation angle measured by the seeker. The inertially referenced LOS angle is defined to be θ, and the angle between the missile centerline and inertial reference in the azimuth or elevation angle plane is θ_m. Radome distortion is the result of nonlinear distortion in the received energy as it passes through the antenna cover. This aberration produces a false

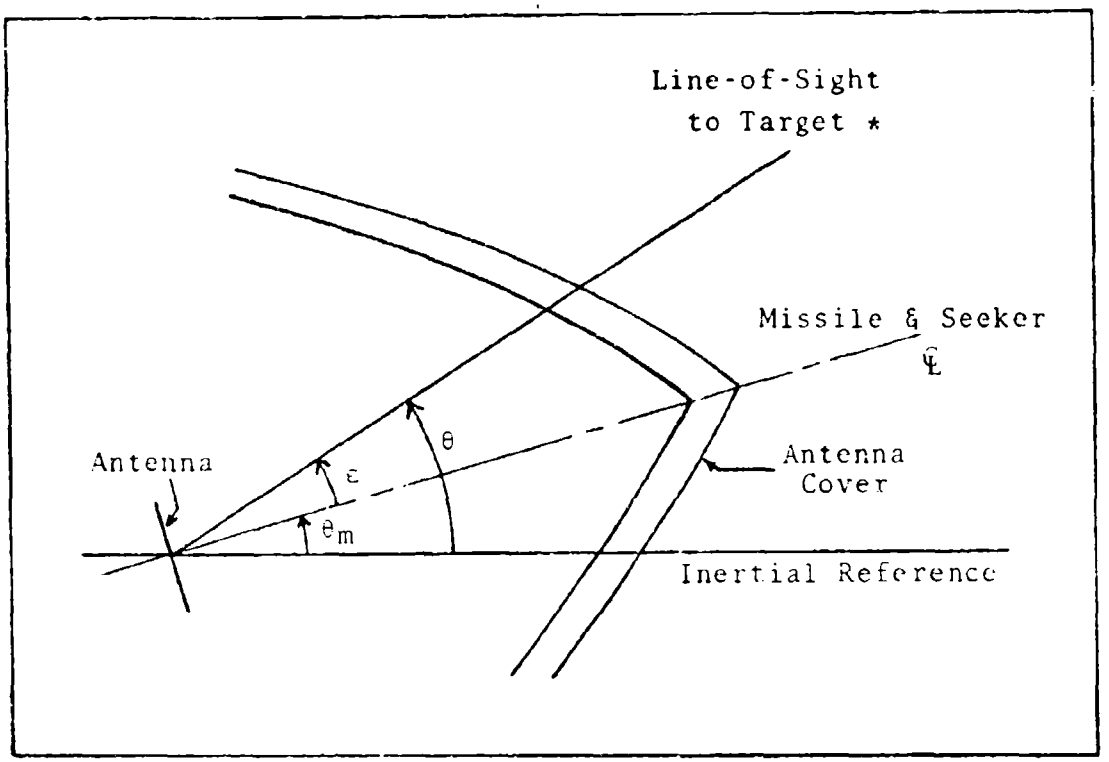

Figure 2-7. Strapdown Seeker -- Radome Geometry

measurement ε', which is interpreted as target motion by the missile guidance system. As shown in Figure 2-8,

$$\varepsilon' = \theta + \theta_r - \theta_m \qquad (21)$$

*Note: The LOS is corrupted by glint and thermal noise at this point.

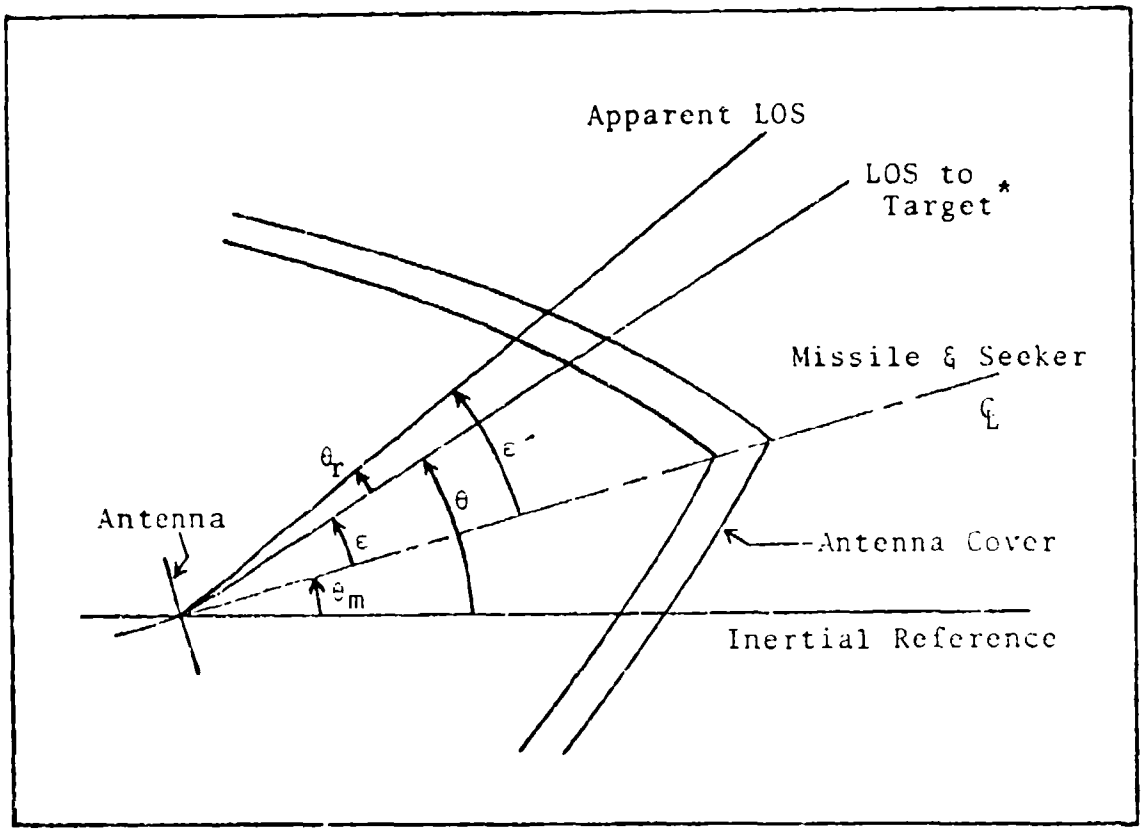

Figure 2-8. Effect of Radome Distortion on Strapdown Seeker

θ_r can be a nonlinear function of several error sources: ε, physical and geometrical properties of the antenna cover, polarization of the received signal, and erosion of the antenna cover's surface during flight. Lutter found that, due to the wide ranges of variation in

*Note: Again, the LOS is corrupted by glint and thermal noise at this point.

these error sources, aberration error is adequately described by a constant slope model (Refs 13; 17:12). Therefore, a linear model for the error due to radome distortion is given by

$$\theta_r = \theta_{rb} + k_r \varepsilon \tag{22}$$

where θ_{rb} is the aberration error bias and k_r is the error slope. Because of the lack of specific data to indicate otherwise, θ_{rb} will be assumed to be zero for this study. The nominal value of k_r was found by Lutter to be 0.001 rad/rad, which correlates well with the Rockwell study (Ref 8:117).

Scale Factor Error. Detector scale factor error is a function of the seeker receiver's resolution, sensitivity, and electronics. Quantitatively, it is the difference between the best straight line fit of the seeker transfer function and unity (Ref 8:13). In the Rockwell study, scale factor error was modelled as a deterministic constant. In order to implement as generic a model as possible, scale factor error is modelled here as a random bias. The maximum value of scale factor error employed by Rockwell was considered to be a 3σ value for the initial condition for the bias. The one-sigma value is given in Table I, which follows the discussion of the last noise in the strapdown seeker model, cross-coupling.

Cross-Coupling. This noise is also caused by seeker receiver effects and appears as a bias in the output signal. The strength of this bias, however, is a function of the measurement in the other channel of the seeker. In other words, the amount of cross-coupling error in the azimuth measurements depends upon the elevation measurement magnitude and vice-versa. This noise is also well-modelled as a random bias, and the one-sigma value for the initial condition was determined in the same way as that for scale factor error. The statistics of the strapdown seeker truth model noises are summarized in Table I.

Table I

Statistics of Strapdown Seeker Truth Model Noises

Noise	σ	τ
Glint	2 ft/sec	0.1 sec
Thermal	$(1 \times 10^{-3}$ rad/ft) x range	--
Boresight error I.C.	0.0006 rad	--
Scale factor error I.C.	0.03	--
Cross-coupling error I.C.	0.003	--

Incorporating the modelling for the strapdown measurements, the model for the strapdown seeker is given in detail in Figure 2-9.

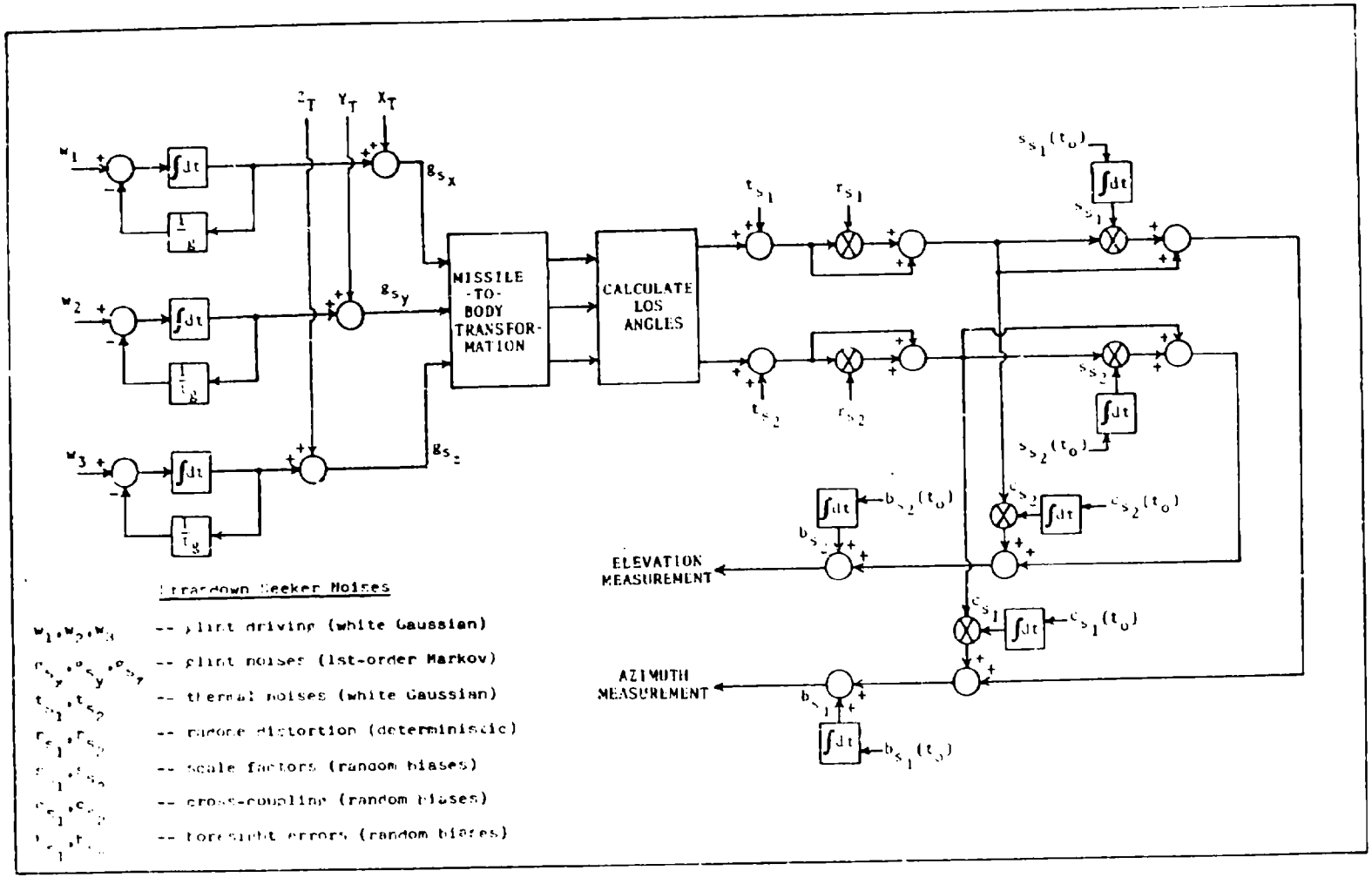

Figure 2-9. Strapdown Seeker Block Diagram

Gimballed Seeker Model

The gimballed seeker model used in this thesis is a generic model designed to be approximately the same order of complexity as the strapdown seeker model of Figure 2-6. As discussed in Chapter I, a gimballed seeker provides inertial measurements of LOS and LOS rate from the seeker boresight. Therefore, the major difference between the gimballed seeker model and the previously developed strapdown seeker model is the inclusion of seeker dynamics. These dynamics will be incorporated assuming an inertially referenced seeker. In other words, the gimbal angles are referenced to the missile frame, not the body frame, in the dynamics model. The gimbal angles relative to the body frame are calculated as necessary using the Euler rotation matrix of eq. (1) and the inertially referenced gimbal angles.

A general diagram of the gimballed seeker model is given in Figure 2-10. This model includes all of the noises used in the strapdown seeker model. It also adds one additive noise, rate gyro noise, which corrupts the gimbal angle rates from the seeker dynamics. Also, the LOS angles are calculated from the target location plus glint noise, both in the missile frame; this is in contrast to the strapdown seeker model in which the LOS angles are calculated from the target location plus glint noise in the body frame. The seeker dynamics will be discussed next.

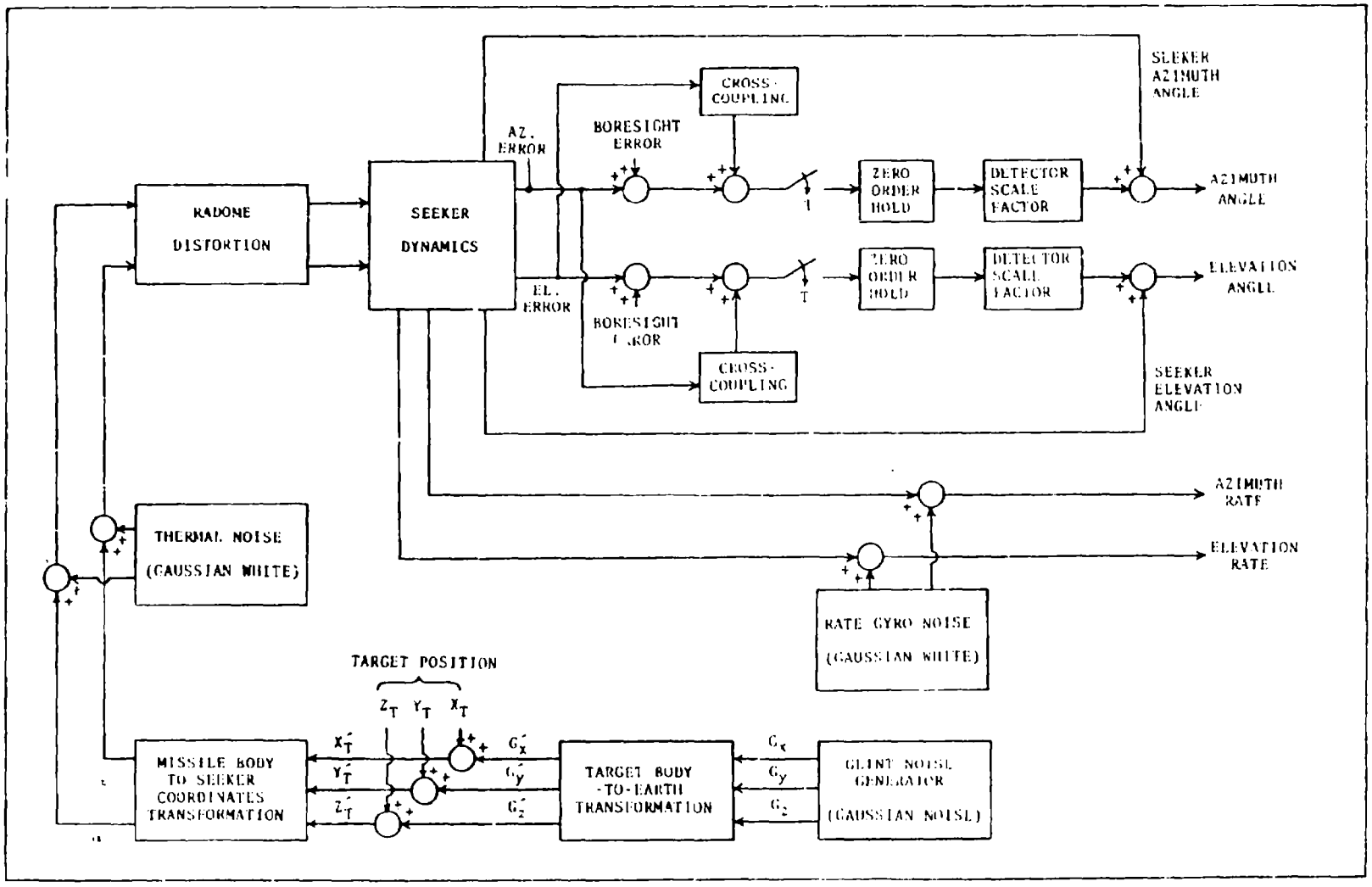

Figure 2-10. Gimballed Seeker Model

Gimballed Seeker Dynamics. The seeker dynamics are the result of the seeker antenna tracking loop. The tracking model used in this thesis is shown in one dimension in Figure 2-11.

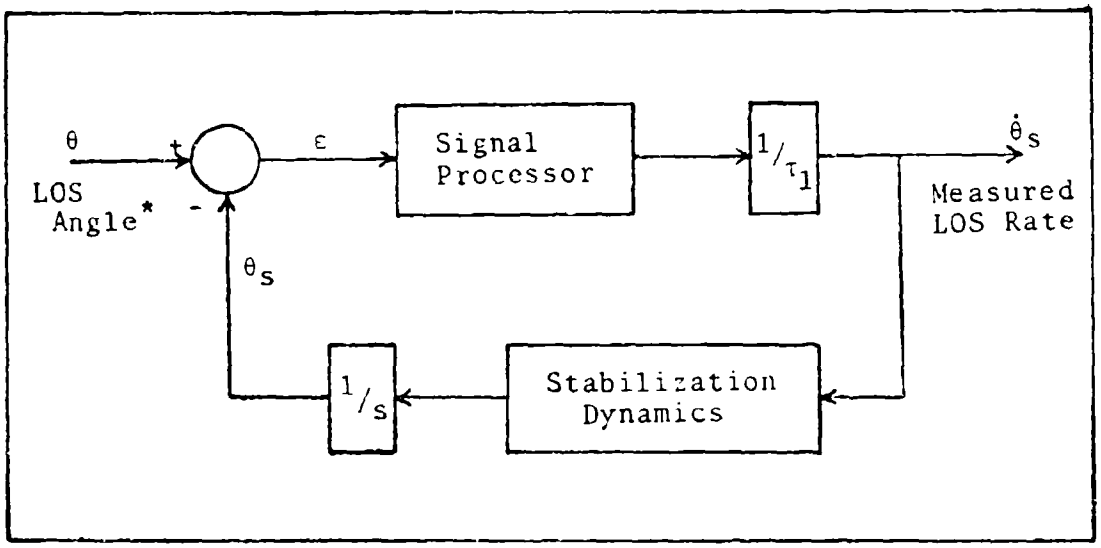

Figure 2-11. Gimballed Seeker Dynamics

In the figure, ε is the error angle between the seeker boresight and the LOS and θ_s is the seeker angle referenced to the missile frame. The gimbal servo motor, the gimbals, and the rate gyro are the key physical subsystems influencing the stabilization dynamics. The loop tracks by commanding a gimbal rate proportional to the error angle, ε. The loop attempts to drive ε to zero, thereby causing the antenna to track the target (Ref 17:13).

*Note: Again, this angle is corrupted by glint noise and thermal noise.

Assuming unity low-frequency (DC) gain for the signal processor and stabilization dynamics, the assumed model for the seeker dynamics is given by the transfer function:

$$\frac{\theta_s}{\theta} = \frac{1}{1 + s\tau_1} \tag{23}$$

so that the error angle is given by:

$$\varepsilon = \frac{1}{s + 1/\tau_1}\,\theta \tag{24}$$

a first order lag of the input angle. The lag constant τ_1, is chosen to be .075 sec from a previous study in which a similar seeker model was used (Ref 5:31). With the seeker dynamics thus defined, a discussion of the gimballed seeker noises follows.

Gimballed Seeker Noises. In general, the noises in Figure 2-10 have the same effect and are modelled in the same way as in the strapdown seeker model. Glint noise enters the gimballed seeker model in the same way and, conceptually, has the same effect as in the strapdown seeker model. Therefore, in order to make as fair a comparison between the two seekers as possible, glint noise is also modelled as a first order Gaussian process with an input noise of σ = 2 ft/sec. For the same reasons, thermal noise in the gimballed seeker model is also modelled as discrete-time white Gaussian noise with the same standard deviation as in Table I. Scale factor, cross-coupling, and boresight error are again biases,

except that their effect is on the measured error angles. Their standard deviations are also chosen to be the same as for the strapdown seeker's values given in Table I. Radome distortion is affected by body motion, and its introduction in the gimballed seeker model is less straightforward than in the strapdown seeker model.

As shown in Figure 2-8, radome distortion is a function of the LOS angle off of the missile centerline. In the gimballed seeker model, however, the seeker centerline rotates with respect to the missile centerline, and the error angle ε is as shown in Figure 2-12. Since

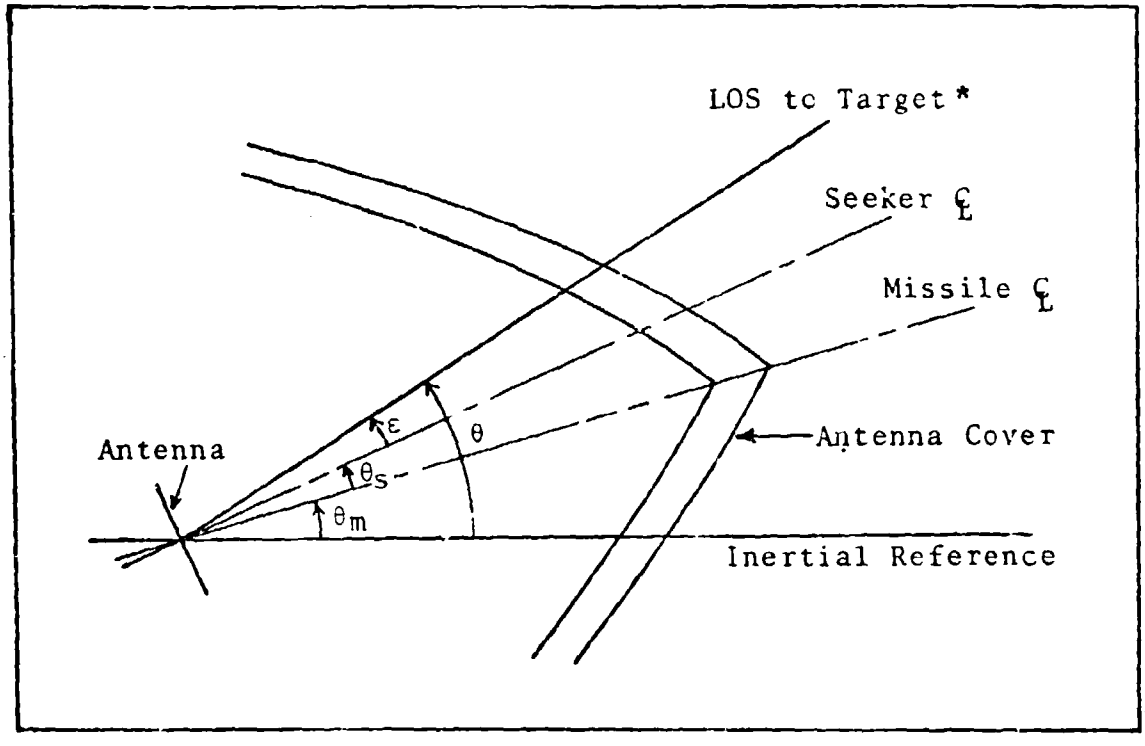

Figure 2-12. Gimballed Seeker -- Radome Geometry

*Note: Again, this angle is corrupted by glint noise and thermal noise.

θ_m is not included in the gimballed seeker model, θ_s and the transformation matrix C_m^b are used to find the azimuth and elevation angles of the LOS with respect to the missile centerline. The procedure for introducing radome distortion in the gimballed seeker model is as follows:

1) Find the unit vector along the LOS in the missile frame.

2) Rotate this vector to the body frame.

3) Find the azimuth and elevation angles of the LOS with respect to the body axes.

4) Corrupt these angles by as in (22).

5) Find the unit vector of the distorted LOS in the body frame.

6) Rotate this vector back to the missile frame.

7) Find the azimuth and angles of the distorted LOS with respect to the missile axes.

The procedure for accomplishing Steps 1-3 is found in Appendix A.

The only noise included in Figure 2-10 which is unique to the gimballed seeker model is the rate gyro noise which corrupts the LOS rate. This noise is included for completeness since a rate gyro cannot provide exact rate measurements. A discrete-time white Gaussian noise is chosen as the model for rate gyro noise. This model is used because it captures the dominant effects of short term rate gyro noise. For the time of flight considered here, long term gyro drift effects are negligible. The standard deviation for the rate gyro noise was chosen to be 1.0 mrad/sec.

With the gimballed seeker model thus described, a detailed block diagram is given in Figure 2-13. The noises and their standard deviations are summarized in Table II.

Table II

Statistics of Gimballed Seeker Truth Model Noises

Noise	σ	τ
Glint	2 ft/sec	0.1 sec
Thermal	(1×10 rad/ft) x range	--
Boresight error I.C.	0.0006 rad	--
Scale factor error I.C.	0.03	-
Cross-coupling error I.C.	0.003	--
Rate Gyro	0.001 rad/sec	--

Truth State Model. The system truth model can now be expressed as a vector, stochastic, ordinary differential equation of the form:

$$\dot{\underline{x}}_S(t) = \underline{g}(\underline{x}_S, t) + \underline{u}_S(t) + \underline{w}_S(t) \qquad (25)$$

in which:

t is time

$\underline{x}_S(t)$ is the truth system state vector

$\underline{g}(\underline{x}_S, t)$ is the truth system dynamics vector

$\underline{w}_S(t)$ is a zero-mean white Gaussian random process with

$$E\{\underline{w}_S(t)\ \underline{w}_S^T(x+\tau)\} = Q_S(t)\ \delta(\tau)$$

$Q_S(t)$ is the truth system noise strength

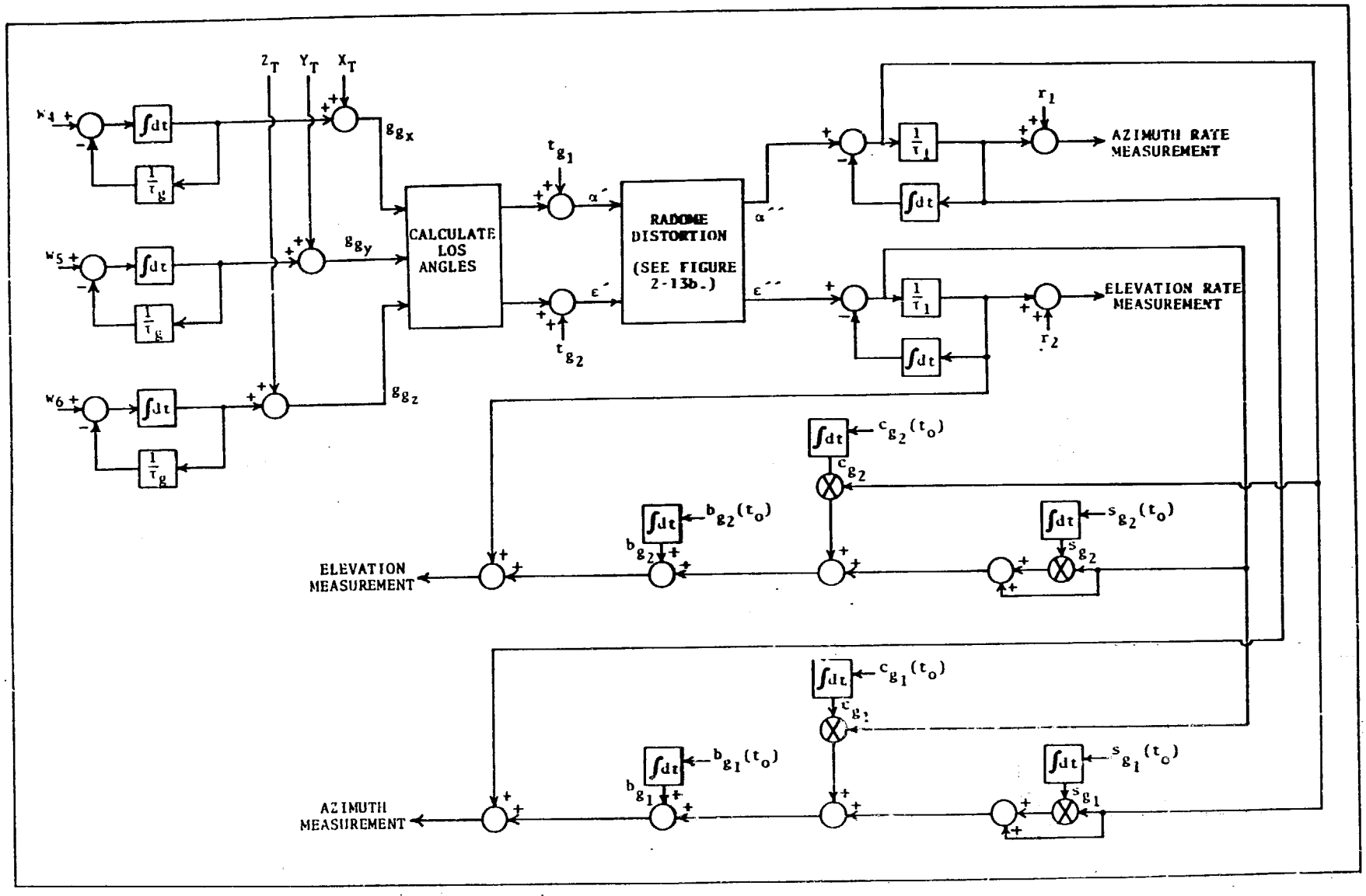

Figure 2-13a. Gimballed Seeker Block Diagram

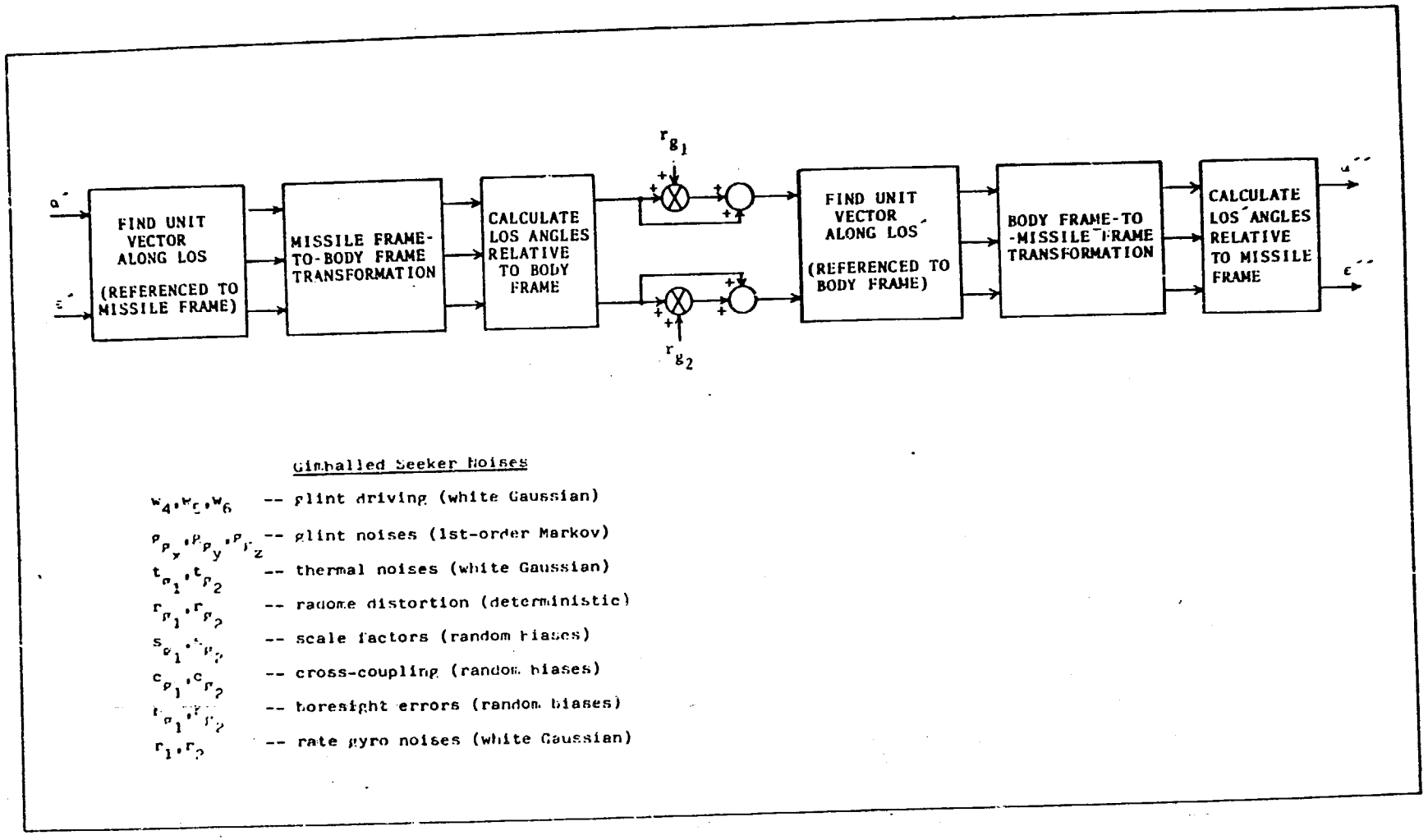

Figure 2-13b. Gimballed Seeker Radome Distortion Block Diagram

In the above, $E\{\ \}$ is the expectation operation and $\delta(\tau)$ is the Dirac delta function. The truth state vector is comprised of the six position and velocity states defined by the LLLGB simulation and the noise states of the two seeker models. The truth state vector is found on the following page.

In the truth state vector; x, y, and z are the coordinates of the target in the missile frame; v_x, v_y, and v_z are the velocities of the target relative to the missile along the missile frame x_m, y_m, and z_m-axes, respectively; ψ_s is the azimuth angle between the gimballed seeker boresight and the x_m-axis; θ_s is the elevation angle between the gimballed seeker boresight and the x_m-axis; g, b, s, and c represent glint, boresight error, scale factor, and cross-coupling states, respectively; and the subscripts s a i g represent the model, strapdown or gimballed, in which the noises appear.

The truth state dynamics equation is defined in eq. (26) on the page following the truth state vector. In eq. (26), τ_1 is the time constant of the glint noises in the strapdown seeker model, τ_2 is the time constant of the gimballed seeker dynamics model, τ_3 is the time constant of the glint noises in the gimballed seeker model. Also in eq. (26); w_1, w_2, and w_3 are the white noises driving the strapdown seeker glint noises; w_{t_1} and w_{t_2} are the white noises representing the thermal noises driving the gimballed seeker dynamics; and w_4, w_5, and w_6 are the white

$$\underline{x}_s = \begin{bmatrix} x \\ v_x \\ y \\ v_y \\ z \\ v_z \\ g_{s_x} \\ g_{s_y} \\ g_{s_z} \\ b_{s_1} \\ b_{s_2} \\ s_{s_1} \\ s_{s_2} \\ c_{s_1} \\ c_{s_2} \\ \psi_s \\ \theta_s \\ g_{g_x} \\ g_{g_y} \\ g_{g_z} \\ b_{g_1} \\ b_{g_2} \\ s_{g_1} \\ s_{g_2} \\ c_{g_1} \\ c_{g_2} \end{bmatrix}$$

$$
\dot{\underline{x}}_s = \begin{bmatrix}
x \\
v_x \\
y \\
v_y \\
z \\
v_z \\
-x_s(7)/\tau_1 \\
-x_s(8)/\tau_1 \\
-x_s(9)/\tau_1 \\
0 \\
0 \\
0 \\
0 \\
0 \\
0 \\
\left[\tan^{-1}\left[\dfrac{x_s(3)+x_s(19)}{x_s(1)+x_s(18)}\right]-x_s(16)\right]/\tau_2 \\
\left[\tan^{-1}\left[\dfrac{x_s(5)+x_s(20)}{\left\{\left[x_s(1)+x_s(18)\right]^2+\left[x_s(3)+x_s(19)\right]^2\right\}^{1/2}}\right]-x_s(17)\right]/\tau_2 \\
-x_s(18)/\tau_3 \\
-x_s(19)/\tau_3 \\
-x_s(20)/\tau_3 \\
0 \\
0 \\
0 \\
0 \\
0 \\
0
\end{bmatrix} + \begin{bmatrix}
0 \\
0 \\
0 \\
0 \\
0 \\
0 \\
w_1 \\
w_2 \\
w_3 \\
0 \\
0 \\
0 \\
0 \\
0 \\
0 \\
w_{t_1} \\
w_{t_2} \\
w_4 \\
w_5 \\
w_6 \\
0 \\
0 \\
0 \\
0 \\
0 \\
0
\end{bmatrix} \qquad (26)
$$

noises driving the gimballed seeker glint noises. Stationarity is assumed in the initial conditions of the glint states. The random constant initial conditions for states (10) through (15) are defined in Table I, and those for states (21) through (26) are defined in Table II.

III. KALMAN FILTER DESIGN

Introduction

This chapter presents the Kalman filter design for incorporating the measurements from the truth model. As will be seen, either the filter dynamics equations or measurement equations are nonlinear in this application, depending on the type of coordinate frame used. For this reason, the basic Kalman filter is not applicable, and either a higher order filter or an approximate Kalman filter, such as the extended Kalman filter, must be used. The extended Kalman filter (EKF) is the filter chosen for application here, for several reasons. Primarily, the first order linearization in the EKF formulation has been shown to be a good approximation to many nonlinear problems (Ref 19:42). Also, the EKF has been applied successfully in previous studies similar to this work (Refs 3;5;14;17;25). Finally, the EKF gain and covariance propagation equations have the same form as the Kalman filter equations, but are linearized about the current state estimate; in effect, providing sufficient accuracy at a level of computational complexity consistent with the design already accomplished. The use of higher order filters, such as Gaussian or truncated second order filters, would achieve somewhat better

performance, but with substantially greater computational loading (Ref 19:225).

The extended Kalman filter does involve an approximation to the actual nonlinear system, however. The accuracy of the filter's state estimates is limited by how well the true system has been modelled. Therefore, as much effort as possible must be spent on developing good system models. Since the EKF gains and estimation error covariance matrices depend on the time history of the state estimates, the actual filter performance must be verified by a Monte Carlo analysis. A Monte Carlo simulation is the method employed in this thesis for examining the EKF's performance. This simulation was facilitated by an available software package (Ref 20).

The EKF equations are not derived here, but good references for the derivations are (Refs 11 and 19). The equations are given and explained in the next section.

Filter Equations

The EKF equations can be placed in these categories: the system dynamics and measurement equations upon which the filter is based, the propagation equations, and the update equations. The filter state equation can be expressed in the form

$$\dot{\underline{x}}(t) = \underline{f}[\underline{x}(t), \underline{u}(t), t] + \underline{G}(t)\underline{w}(t) \qquad (27)$$

where

$\underline{x}(t)$ is the n-state filter vector

$\underline{f}[\underline{x}(t),\underline{u}(t),t]$ is the filter dynamics vector

$\underline{u}(t)$ is a deterministic forcing function

$\underline{w}(t)$ is a zero-mean white Gaussian noise process independent of $\underline{x}(t_o)$, of strength $\underline{Q}(t)$, such that

$$E\{\underline{w}(t)\underline{w}^T(t+\tau)\} = \underline{Q}(t)\delta(\tau) \tag{28}$$

and where $\underline{x}(t_o)$ is modelled as a Gaussian random variable with mean $\hat{\underline{x}}_o$ and covariance $\underline{P}_o$. Note that the dynamic driving noise is assumed to enter in a linear additive fashion (Ref 17:53). The measurement equations can be expressed as

$$\underline{z}(t_i) = \underline{h}[\underline{x}(t_i),t_i] + \underline{v}(t_i) \tag{29}$$

where

$\underline{z}(t_i)$ is the m-dimensional measurement vector

$\underline{v}(t_i)$ is a zero-mean white Gaussian noise sequence, independent of $\underline{x}(t_o)$ and $\underline{w}(t)$, with strength $\underline{R}(t_i)$ such that

$$E\{\underline{v}(t_i)\underline{v}^T(t_j)\} = \underline{R}(t_i)\delta_{ij} \tag{30}$$

The filter state propagation equation is

$$\hat{\underline{x}}(t/t_i) = \underline{f}[\hat{\underline{x}}(t/t_i),\underline{u}(t),t] \tag{31}$$

where the notation $\hat{\underline{x}}(t/t_i)$ means the optimal (filter) estimate of the state, $\underline{x}$, at time, t, given the estimates up to and including time t_i. The covariance propagation

equation is

$$\dot{\underline{P}}(t/t_i) = \underline{F}[t;\hat{\underline{x}}(t/t_i)]\underline{P}(t/t_i) + \underline{P}(t/t_i)\underline{F}^T[t;\hat{\underline{x}}(t/t_i)] + \underline{G}(t)\underline{Q}(t)\underline{G}^T(t) \quad (32)$$

where $\underline{F}[t;\hat{\underline{x}}(t/t_i)]$ is the linearization of the filter dynamics vector about the current estimate given by

$$\underline{F}[t;\hat{\underline{x}}(t/t_i)] \triangleq \left.\frac{\partial \underline{f}[\underline{x}(t),\underline{u}(t),t]}{\partial \underline{x}}\right|_{\underline{x} = \hat{\underline{x}}(t/t_i)} \quad (33)$$

where the notation $\triangleq$ denotes "defined to be." The initial conditions of eqs. (31) and (32) are given by

$$\hat{\underline{x}}(t_i/t_i) = \hat{\underline{x}}(t_i^+) \quad (34)$$

$$\underline{P}(t_i/t_i) = \underline{P}(t_i^+) \quad (35)$$

i.e., the result of the measurement at time t_i, where t_i^+ denotes the time t_i after update.

The extended Kalman filter gain, $\underline{K}(t_i)$, is defined by

$$\underline{K}(t_i) = \underline{P}(t_i^-)\underline{H}^T[t_i;\hat{\underline{x}}(t_i^-)] \cdot \{\underline{H}[t_i;\hat{\underline{x}}(t_i^-)]\underline{P}(t_i^-)\underline{H}^T[t_i;\hat{\underline{x}}(t_i^-)] + \underline{R}(t_i)\}^{-1} \quad (36)$$

in which $\underline{H}[t_i;\hat{\underline{x}}(t_i)]$ is the linearization of $\underline{h}[\underline{x}(t_i),t_i]$ given by

$$\underline{H}[t_i;\hat{\underline{x}}(t_i^-)] = \left.\frac{\partial \underline{h}[\underline{x}(t_i),t_i]}{\partial \underline{x}}\right|_{\underline{x} = \hat{\underline{x}}(t_i^-)} \quad (37)$$

and t_i^- denotes the time t_i just before update. The update equations are

$$\underline{x}(t_i^+) = \underline{x}(t_i^-) + \underline{K}(t_i)\{\underline{z}_i - \underline{h}[\underline{x}(t_i^-), t_i]\} \quad (38)$$

$$\underline{P}(t_i^+) = \underline{P}(t_i^-) - \underline{K}(t_i)\,\underline{H}[t_i; \underline{x}(t_i^-)]\,\underline{P}(t_i^-) \quad (39)$$

in which $\underline{z}_i$ is the realization of the measurement $\underline{z}(t_i)$ given in eq. (29). Note that the measurement update provides the initial conditions for the following propagation and the quantities propagated to time t_i^- are the values which are then updated.

The extended Kalman filter equations will now be applied in the filter design used for this thesis.

EKF Design

The primary concern now is to achieve a practical and workable filter design for analyzing the use of the truth model measurements and dynamics outputs. A filter design in which all the states are completely observable is also desirable (Ref 18:43-6). These considerations must be taken into account when selecting the filter states, the filter coordinate frame, and the initial conditions for the filter.

Realistically, one would consider an air-to-ground, tactical missile to be driven by the available measurements from all onboard sensors, initialized by signals from the launching aircraft. In the case of the dual-seeker missile with onboard INS, the number of seeker measurements will vary, depending on the number of seekers operating. However, the missile guidance will always be receiving ownship acceleration and orientation information, assuming

a fail-safe INS. Since the emphasis in this thesis is on comparing simulated guidance performance during various seeker-dependent scenarios, the filter design should emphasize use of the seeker measurements. Also, the onboard computer memory and time available to the filter will certainly be limited. All of these considerations led to the following EKF design.

The filter state vector chosen is composed of the three position states and three velocity states of the target with respect to the missile in the missile frame. Accelerations need not be estimated since noisy measurements of acceleration are available from the INS. The time-correlated lag noises and biases of the seeker models are not estimated in consideration of the realistic computer resources of the conceptual missile and because their estimation would not contribute significantly to this study. The filter state vector, therefore, is given as

$$\mathbf{x}_f = \begin{bmatrix} x_1 \\ x_2 \\ x_3 \\ x_4 \\ x_5 \\ x_6 \end{bmatrix} = \begin{bmatrix} x \\ v_x \\ y \\ v_y \\ z \\ v_z \end{bmatrix} \tag{40}$$

where

x is the x_m component of the target position

y is the y_m component of the target position

z is the z_m component of the target position

v_x is the component of target velocity along the x_m-axis

v_y is the component of target velocity along the y_m-axis

v_z is the component of target velocity along the z_m-axis

The state vector is written in inertial rectangular coordinates because the filter dynamics equations are linear in such coordinates, reducing the computational burden during integration (Ref 20:83) and in the local vertical (missile) frame because previous filter studies have shown that there are advantages to local vertical frame implementation (Refs 3:5-13; 5:9; 17:1; 25:99). Also, the filter dynamics equations for this application are straightforward when written in the missile frame since the accelerations in that frame are directly available. This filter model is essentially one good, potential model that will accomplish the aim intended for it in this thesis.

The linear version of eq. (27) is given by

$$\dot{\underline{x}}(t) = \underline{F}(t)\underline{x}(t) + \underline{B}(t)\underline{u}(t) + \underline{G}(t)\underline{w}(t) \tag{41}$$

and is defined for this model to be

$$\begin{bmatrix} \dot{x}_1 \\ \dot{x}_2 \\ \dot{x}_3 \\ \dot{x}_4 \\ \dot{x}_5 \\ \dot{x}_6 \end{bmatrix} = \begin{bmatrix} 0 & 1 & 0 & 0 & 0 & 0 \\ 0 & 0 & 0 & 0 & 0 & 0 \\ 0 & 0 & 0 & 1 & 0 & 0 \\ 0 & 0 & 0 & 0 & 0 & 0 \\ 0 & 0 & 0 & 0 & 0 & 1 \\ 0 & 0 & 0 & 0 & 0 & 0 \end{bmatrix} \begin{bmatrix} x_1 \\ x_2 \\ x_3 \\ x_4 \\ x_5 \\ x_6 \end{bmatrix} + \begin{bmatrix} 0 & 0 & 0 \\ 1 & 0 & 0 \\ 0 & 0 & 0 \\ 0 & 1 & 0 \\ 0 & 0 & 0 \\ 0 & 0 & 1 \end{bmatrix} \begin{bmatrix} a_x \\ a_y \\ a_z \end{bmatrix} + \begin{bmatrix} 0 & 0 & 0 \\ 1 & 0 & 0 \\ 0 & 0 & 0 \\ 0 & 1 & 0 \\ 0 & 0 & 0 \\ 0 & 0 & 1 \end{bmatrix} \begin{bmatrix} w_1 \\ w_2 \\ w_3 \end{bmatrix} \tag{42}$$

in which

a_x is the target acceleration along the x_m-axis from the truth model

a_y is the target acceleration along the y_m-axis from the truth model

a_z is the target acceleration along the z_m-axis from the truth model

w_1, w_2, and w_3 are the zero-mean, white Gaussian noises representing the uncertainties in the three INS channels.*

It should be noted that, given the linear dynamics of eq. (42), the partial derivatives of eq. (33) need not be evaluated during propagation, greatly decreasing integration time.

The measurement vector is 6-dimensional when both seekers are tracking and is given by

$$\underline{z}(t_i) = \begin{bmatrix} z_1 \\ z_2 \\ z_3 \\ z_4 \\ z_5 \\ z_6 \end{bmatrix} = \begin{bmatrix} \alpha_s \\ \varepsilon_s \\ \alpha_g \\ \varepsilon_g \\ \dot{\alpha}_g \\ \dot{\varepsilon}_g \end{bmatrix} \tag{43}$$

where

α_s is the azimuth angle of the target with respect to the x_b-axis as measured by the strapdown seeker

ε_s is the elevation angle of the target with respect to the x_b-y_b plane as measured by the strapdown seeker

*Note: White Gaussian noise has been shown to be an adequate model for short-term accelerometer errors for some purposes (Ref 24:2-4).

α_g is the azimuth angle of the target with respect to the x_m -axis as measured by the gimballed seeker

ε_g is the elevation angle of the target with respect to the x_m-y_m plane as measured by the gimballed seeker

$\dot{\alpha}_g$ is the rate of change of α_g as measured by the gimballed seeker

$\dot{\varepsilon}_g$ is the rate of change of ε_g as measured by the gimballed seeker

With this measurement vector, eq. (29) is written as

$$\underline{z}(t_i) = \begin{bmatrix} \tan^{-1}\left[\dfrac{C_4x_1+C_5x_3+C_6x_5}{C_1x_1+C_2x_3+C_3x_5}\right] \\ \tan^{-1}\left[\dfrac{C_7x_1+C_8x_3+C_9x_5}{\{(C_1x_1+C_2x_3+C_3x_5)^2+(C_4x_1+C_5x_3+C_6x_5)^2\}^{\frac{1}{2}}}\right] \\ \tan^{-1}\left[\dfrac{x_3}{x_1}\right] \\ \tan^{-1}\left[\dfrac{x_5}{(x_1^2+x_3^2)^{\frac{1}{2}}}\right] \\ \dfrac{x_1x_4 - x_2x_3}{x_1^2+x_3^2} \\ \dfrac{(x_1^2+x_3^2)x_6 - (x_1x_2+x_3x_4)x_5}{(x_1^2+x_3^2)^{\frac{1}{2}}(x_1^2+x_3^2+x_5^2)} \end{bmatrix} + \begin{bmatrix} v_1 \\ v_2 \\ v_3 \\ v_4 \\ v_5 \\ v_6 \end{bmatrix} \qquad (44)$$

where $C_m^b = \begin{bmatrix} C_1 & C_2 & C_3 \\ C_4 & C_5 & C_6 \\ C_7 & C_8 & C_9 \end{bmatrix}$ is the orthogonal

transformation matrix from the missile frame to the body frame defined by eq. (1), and v_1, v_2, ..., v_6 are the discrete-time measurement uncertainties defined by eq. (30). The azimuth and elevation angles expressed as a function of the filter states are straightforward from their definition in eqs. (16) and (17). The angle rates as a function of the filter states are found by taking the first derivatives of their corresponding angle expressions as functions of time.

As is easily seen in eq. (44), the measurement vector defined by eq. (43) is a highly nonlinear function of the filter states. For this reason, the partial derivatives of $\underline{h}[\underline{x}(t_i), t_i]$ as defined by eq. (44) must be calculated and are evaluated at each update time. The derivation of it and the resulting measurement matrix $\underline{H}[t_i; \hat{\underline{x}}(t_i^-)]$ are given in Appendix B.

EKF Noise Strengths and Initial Conditions

Again, the strengths of the dynamic driving noises w_1, w_2, and w_3 in eq. (42) represent the uncertainties in the accelerations from the INS. These strengths, in the notation of eq. (28), are given by

$$\underline{Q}(t) = \begin{bmatrix} Q_1 & 0 & 0 \\ 0 & Q_2 & 0 \\ 0 & 0 & Q_3 \end{bmatrix} \qquad (45)$$

The effect of the noise strengths Q_1, Q_2, and Q_3 is seen in the covariance propagation eq. (32). With zero $\underline{Q}(t)$, the

filter's uncertainty in its estimate represented by $\underline{P}(t/t_i)$ will approach zero as t approaches infinity. In order to prevent $\underline{P}(t/t_i)$ from going to zero such that the filter will essentially ignore the measurements $\underline{z}(t_i)$, $\underline{Q}(t)$ must be kept nonzero.

Realistically, $\underline{Q}(t)$ would increase drastically if an accelerometer failure occurs. Neglecting such failures, the expected error in a given accelerometer is relatively constant and a function of the quality of instrument used. Also, the error can be assumed to be much the same for three accelerometers mounted on the same platform. Recognizing that the INS instruments would be of rather poor quality, the strength of each of the noises w_1, w_2, and w_3 was chosen nominally as 1 ft^2/sec^3. This value can be changed for filter tuning as discussed in the next chapter.

The strengths of the measurement noise vector $v(t_i)$ are also a major consideration in filter tuning. Realistically, the only way to gain a priori knowledge of the noise strength matrix $\underline{R}(t_i)$ as defined in eq. (30) is to consider the truth model noise entering each measurement. Since all of the truth states are not included in the filter model, $\underline{R}(t_i)$ must include pseudonoise to account for the neglected states. Assuming that all measurements are independent, $\underline{R}(t_i)$ is a diagonal matrix given by

$$\underline{R}(t_i) = \begin{bmatrix} R_1 & 0 & 0 & 0 & 0 & 0 \\ 0 & R_2 & 0 & 0 & 0 & 0 \\ 0 & 0 & R_3 & 0 & 0 & 0 \\ 0 & 0 & 0 & R_4 & 0 & 0 \\ 0 & 0 & 0 & 0 & R_5 & 0 \\ 0 & 0 & 0 & 0 & 0 & R_6 \end{bmatrix} \quad (46)$$

Since the measurements corresponding to the azimuth and elevation channels of each seeker are generated in an equivalent manner in the truth model, it can be assumed that $R_1 = R_2$, $R_3 = R_4$, and $R_5 = R_6$. Initial choices for the noise strengths are left for discussion in the filter tuning chapter.

As mentioned in the filter equations section, $\underline{x}(t_0)$ is a Gaussian random variable with mean $\hat{\underline{x}}_0$ and covariance $\underline{P}_0$. The mean is conceptually the true initial conditions from the truth model. The covariance $\underline{P}_0$ defines the Gaussian distribution about the true initial conditions that represents the initial state uncertainty. Realistically, the filter would be initialized by the launching aircraft's INS just before launch. Therefore, $\underline{P}_0$ is a measure of the confidence given to the aircraft INS. Considering magnitudes of the launch range of 20,000 ft and initial missile velocity of 843.9 ft/sec, $\underline{P}_0$ was chosen to be

$$\underline{P}_0 = \begin{bmatrix} 10,000 & 0 & 0 & 0 & 0 & 0 \\ 0 & 10 & 0 & 0 & 0 & 0 \\ 0 & 0 & 10,000 & 0 & 0 & 0 \\ 0 & 0 & 0 & 10 & 0 & 0 \\ 0 & 0 & 0 & 0 & 10,000 & 0 \\ 0 & 0 & 0 & 0 & 0 & 10 \end{bmatrix} \quad (47)$$

representing an uncertainty in the INS at launch of about 1%. The initial covariances of the filter states provide reasonable initial conditions for the filter covariance matrix $\underline{P}(t)$ which is propagated to this first update time via eq. (32). The initial $\underline{P}(t)$ is a major filter tuning consideration. It is discussed further in the following chapter which presents the implementation of the model designs accomplished in the past two chapters.

IV. MODEL IMPLEMENTATION/METHOD OF EVALUATION

Introduction

The system truth model developed in Chapter II and the extended Kalman filter developed in Chapter III are designs which lend themselves readily to digital computer implementation. This chapter presents the techniques for accomplishing this implementation with the goal of achieving the best filter performance possible. Following the implementation considerations is a discussion of the way in which the filter will be used to evaluate the four measurement policies.

Software Implementation

The purpose of the preceding Kalman filter development was to implement a practical filter design and compare its performance against the truth model in a Monte Carlo study of the measurement policies given in Chapter I. The software package SOFE developed by Mr. S. H. Musick of the Air Force Avionics Laboratory (Ref 20), provided the skeletal structure for this iimplementation and Monte Carlo analysis. A postprocessor, SOFEPL, also developed by the Avionics Laboratory (Ref 21), provided the capability for producing Calcomp plots of the the results. A sample of the plot type chosen for use in this thesis, shown in Figure 4-1, presents the sample statistics taken from 20 runs of the filter. This number of runs was chosen for

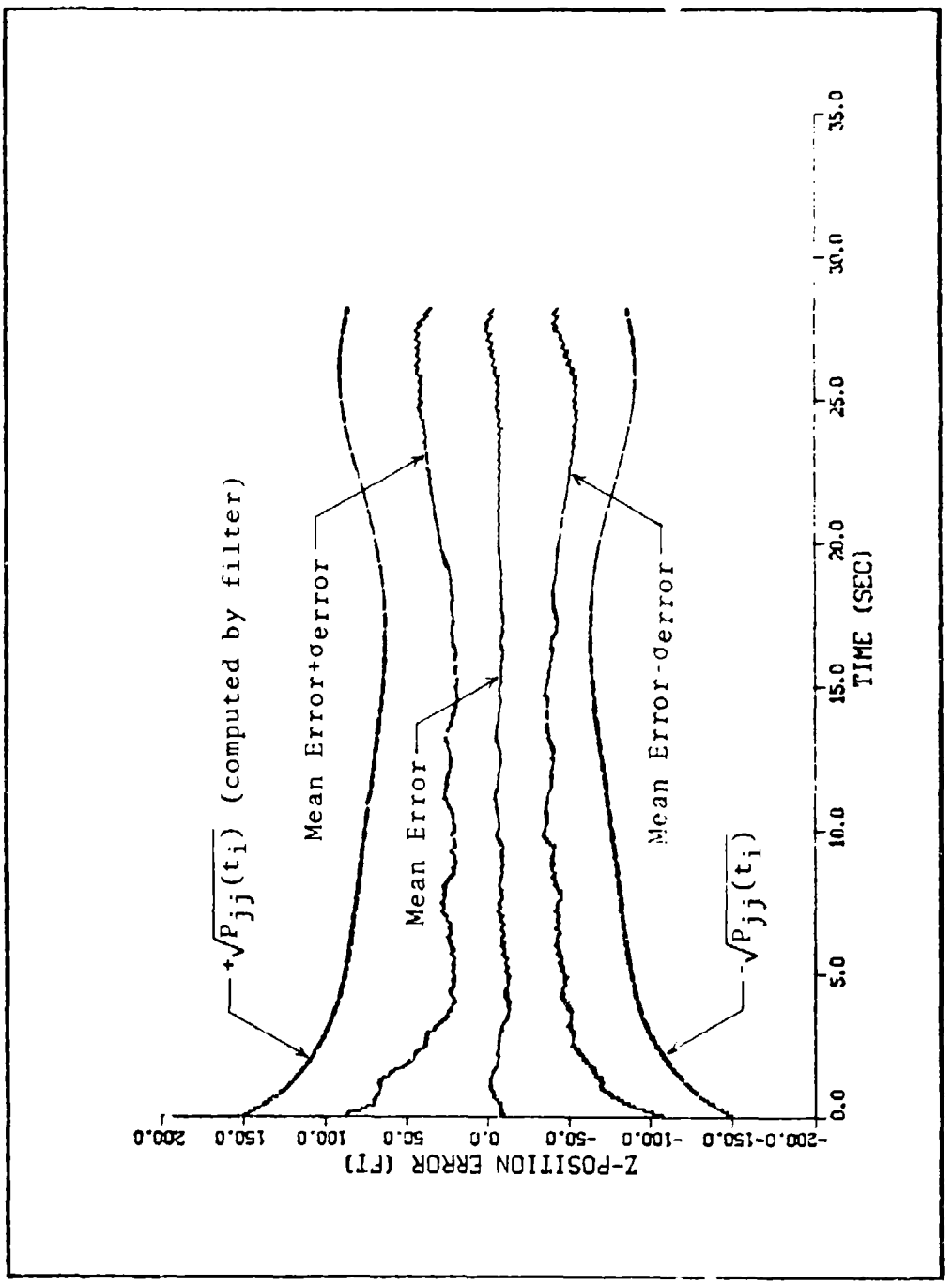

Figure 4-1. Sample SOFEPL Plot

evaluating the filter's performance because previous studies have shown that the statistics are representative over a 20 run ensemble (Refs 5:76; 14:5-7; 25:65).

The plot type chosen gives the mean error of the filter state estimate minus the truth state, the envelope of the mean plus and minus the standard deviation of the actual error, and the envelope of plus and minus the square root of the filter-computed error variance corresponding to the state. From such a plot, one may evaluate the filter's performance by observing whether the error is zero-mean and whether the filter's variance corresponds well to the actual system's mean-squared value. The particular plot shown displays good filter performance since the mean and mean-squared value are well within the filter's variance and because the mean error is approximately zero over the ensemble of runs. This type of plot will be used for filter tuning and performance evaluation as will be seen following the discussion of the rest of the software implementation considerations.

A major factor in implementing the truth model simulation and the extended Kalman filter design is the solution of the differential equations of the truth state, filter state, and filter covariance, eqs. (26), (32), and (42). The integration of the homogeneous parts of these equations is accomplished through the use of a fifth order numerical integrator supplied in SOFE. The effect of the driving noise in the filter dynamics

differential eq. (42) is taken into account by the term "$\underline{G}(t)\underline{Q}(t)\underline{G}^T(t)$" in the filter covariance differential eq. (32). The effect of the truth model noise is taken into account by adding discrete-time samples of the equivalent white Gaussian discrete-time stochastic process for the truth model, at appropriate intervals during the integration cycle.

The eight truth states which are driven by white Gaussian noises are all first order lag models. Assuming independent models, the equivalent discrete-time noise strengths, $Q_d(t_i)$'s, are the solutions to

$$Q_d(t_i) = \int_{t_i}^{t_{i+1}} \Phi(t_{i+1},\tau)G(\tau)Q(\tau)G^T(\tau)\Phi^T(t_{i+1},\tau)\, d\tau \qquad (48)$$

in which $\Phi(t_{i+1},\tau)$ is the element of the system state transition matrix corresponding to the given state (Ref 18:171). For a first order Markov process, $\Phi(t_{i+1},\tau)$ is given by

$$\Phi(t_{i+1},\tau) = e^{-\frac{(t_{i+1},\tau)}{\tau}} \qquad (49)$$

in which τ is the time constant of the model. Therefore, the solution to eq. (48) is

$$\begin{aligned} Q_d(t_i) &= \int_{t_i}^{t_{i+1}} Q\, e^{-2(t_{i+1}-T)/\tau}\, dT \\ &= \frac{\tau Q}{2}\left[1-e^{-2(t_{i+1}-t_i)/\tau}\right] = \sigma^2\left[\ \right] \end{aligned} \qquad (50)$$

where σ is the standard deviation of the state viewed as the output of the first order lag (Ref 18:185). In SOFE,

noise samples of strength Q_d for each truth state are added at one prespecified interval. This interval must be smaller than the shortest time constant in eq. (26) by a factor of at least one-half in order to satisfy the Shannon sampling theorem (Ref 18:295). The period for adding the discrete-time noise samples was chosen to be one-fifth the shortest system time constant, which is 0.075 sec in the gimbal dynamics model. The factor of one-fifth satisfies the Shannon sampling criterion while minimizing the computer burden inherent in interrupting the integration cycle to add the noise samples. With truth model and filter propagations thus accomplished, the remaining implementation consideration is filter update.

The actual filter update formulation used in SOFE is the sequential scalar-measurement, square-root form developed by Carlson. This formulation has implementation advantages in computational speed and accuracy which need not be discussed in detail here but can be found, along with the equations, in Refs 18:385 and 20:26-32. The importance of the update formulation used in SOFE is that measurements are incorporated sequentially and any particular measurement can thus be readily suppressed. Provision was made in the software implementation for this thesis to allow any combinations of strapdown seeker angle measurements, gimballed seeker angle measurements, and gimballed seeker angle-rate measurements over any time interval during the simulation run. This method of

incorporating the measurements provided the flexibility needed for tuning the filter and performing the desired analyses. With the software implementation of the truth model and EKF design thus developed, filter tuning can now be discussed.

Filter Tuning

The intent of filter tuning is to achieve the best possible filter performance in the realistic truth model environment, given the modelling approximations employed in the filter design. In a practical sense, the filter parameters are adjusted to allow it to estimate its state vector as accurately as possible. As mentioned previously, tuning is accomplished by varying the filter dynamic driving noise strength, measurement noise strength, and initial covariance matrix. To begin the tuning process, reasonable first choices for $\underline{Q}(t)$, $\underline{R}(t)$ and $\underline{P}(t_0)$ must be selected. An initial value of $\underline{Q}(t)$, chosen in Chapter III, is 1 ft^2/sec^3 for all three diagonal elements. Initial values for R_1 , R_3 , and R_5 were selected by running the filter with all six measurements over the entire run and examining the measurement residual $\underline{r}(t_i)$ defined as

$$\underline{r}(t_i) = \underline{z}_i - \underline{h}[\underline{x}(t_i^-), t_i] \tag{51}$$

for all the times t_i. The residual vector defines the error between the true measurements and what the filter predicts the measurement to be. This residual vector is multiplied by the filter gain $\underline{K}(t_i)$ to update the filter

state vector as seen in eq. (38).

By examining the resulting residual vector, one gains insight into how strongly the filter should be weighting the measurements. One approach is to consider the maximum residual standard deviation to be a 2 or 3σ value for $\underline{R}(t)$. Using this methodology, the first values for $\underline{R}(t)$ were chosen to be 0.00125 rad^2. Both $\underline{Q}(t)$ and $\underline{R}(t)$ were held constant over the entire missile flight, because the missile dynamics are relatively constant throughout the flight and because the dominant truth model noises are range-independent.

A reasonable initial value for $\underline{P}(t)$, as stated in Chapter III, is the covariance matrix of the filter initial conditions. Therefore, $\underline{P}(0)$ was initially chosen to be

$$\underline{P}(0) = \begin{bmatrix} 10{,}000 & 0 & 0 & 0 & 0 & 0 \\ 0 & 10 & 0 & 0 & 0 & 0 \\ 0 & 0 & 10{,}000 & 0 & 0 & 0 \\ 0 & 0 & 0 & 10 & 0 & 0 \\ 0 & 0 & 0 & 0 & 10{,}000 & 0 \\ 0 & 0 & 0 & 0 & 0 & 10 \end{bmatrix} \qquad (52)$$

corresponding to $\underline{P}_0$ defined in eq. (47). With these values of $\underline{Q}$, $\underline{R}$, and $\underline{P}(0)$, plots of the six filter states' errors over 20 runs with both seekers operative throughout are found in Figures C-1 through C-6. As seen in the plots, the error standard deviation is well bounded by the filter covariance envelope for most of the states. However, the

filter initial conditions are not zero-mean over the 20 runs for all of the states.

The reason for the non-zero-mean initial conditions is the quality of the random number generator used in SOFE. To demonstrate this, a 50-run study was made, and the plot for the v_x state is given in Figure C-7. In comparison to Figure C-2, the mean of the initial conditions for 50 runs is much closer to zero. As a further demonstration, the seed for the random number generator was changed for 20 runs, and the mean of the initial conditions of the same state v_x is seen to change signs in Figure C-8. Although the initial conditions are not zero-mean over 20 runs, this is not adequate motivation for increasing the number of runs of this study. The statistics are still representative at steady-state, and the non-zero-mean initial conditions can be compensated by increasing $\underline{P}(0)$ as demonstrated in Figures C-7 and C-8. For these runs, the square root of each element of $\underline{P}(0)$ was chosen to be 150% of the standard deviations of the filter initial conditions.

The increased value of $\underline{P}(0)$ was used for the rest of the tuning runs and for the result runs. Having a large enough initial covariance for the filter is desirable to prevent the filter from believing the initial filter estimates are better than they truly are. It will be seen that $\underline{P}(0)$ thus chosen is adequate for the rest of the runs made for this study.

The remaining considerations to be made for filter tuning are the values of $\underline{Q}$ and $\underline{R}$. Varying $\underline{Q}$ by factors of 10 and 1/10 revealed that the filter is fairly insensitive to the dynamic driving noise strength, therefore, further tuning was done by varying $\underline{R}$. The most straightforward way to find the best values for R_1, R_3, and R_5 is to tune separately for each set of measurements. Therefore, the filter was run with just the strapdown measurements initially, then just the gimballed angle measurements, and finally just the gimballed angle-rate measurements, selectively choosing a good value for the measurement noise for each. Each set of runs was begun with the value of $R=0.00125$ rad^2, and this R was adjusted up or down to improve the filter performance.

The initial plots for the strapdown seeker are found in Figures C-9 through C-14. The filter is seen to perform well except in the z-position state. Upon varying R_1, it was found that increasing R_1 to 0.0028 rad^2 resulted in the improved performance for that state seen in Figure C-15. Thus, this value was selected for R_1 (and R_2).

The initial plots for the gimballed seeker, angle measurements only, are found in Figures C-16 through C-21. The filter is seen to perform extremely well in all states, therefore R_3 was decreased to examine the filter's weighting of these measurements. Decreasing R_3 to 0.000556 rad^2 increased the transient behavior of the y-position state, as seen in Figure C-22. The filter

errors are still zero-mean and well-bounded for this state and all other states so this value for R_3 would seem to be appropriate, since the lowest possible value is desirable. Decreasing R_3 further would increase the transient behavior in the y-position estimate even more and probably not gain much in filter performance. Therefore, the value for R_3 (and R_4) was selected to be 0.000556 rad^2.

The initial plots for the gimballed seeker, angle-rate measurements only, are found in Figures C-23 through C-28. The filter is seen to diverge in x and z, gradually at first, but with an increasing slope towards the end of the trajectory. This divergent behavior could be due to the lack of observability with the angle-rate measurements only or to the over-weighting of noisy measurements. R_5 was increased to examine the latter possibility. With R_5 at a value of 0.0078 rad^2, further increases do not significantly improve filter performance. The plots for R_5=0.0078 rad^2 are shown in Figures C-29 through C-34. TThe errors are bounded by the filter's covariance for the length of the run but still seem to be divergent at the end. Increasing R_5 to 0.01125 rad^2 did not improve the filter's performance significantly in the two sensitive states, as seen in Figures C-35 and C-36. Therefore, R_5 (and R_6) was selected to be 0.0078 rad^2, and the divergence can be attributed to an observability problem with these measurements.

With this coarse filter tuning thus accomplished, the

resulting measurement noise covariance is given by

$$\underline{R}(t)=\underline{R}=\begin{bmatrix} 0.0028 & 0 & 0 & 0 & 0 & 0 \\ 0 & 0.0028 & 0 & 0 & 0 & 0 \\ 0 & 0 & 0.000556 & 0 & 0 & 0 \\ 0 & 0 & 0 & 0.000556 & 0 & 0 \\ 0 & 0 & 0 & 0 & 0.0078 & 0 \\ 0 & 0 & 0 & 0 & 0 & 0.0078 \end{bmatrix} \quad (53)$$

Again, the state noise strength matrix was chosen to be

$$\underline{Q}(t) = \underline{Q} = \begin{bmatrix} 1.0 & 0 & 0 \\ 0 & 1.0 & 0 \\ 0 & 0 & 1.0 \end{bmatrix} \quad (54)$$

and the initial state covariance was chosen to be

$$\underline{P}(0) = \begin{bmatrix} 22,500 & 0 & 0 & 0 & 0 & 0 \\ 0 & 225 & 0 & 0 & 0 & 0 \\ 0 & 0 & 22,500 & 0 & 0 & 0 \\ 0 & 0 & 0 & 225 & 0 & 0 \\ 0 & 0 & 0 & 0 & 22,500 & 0 \\ 0 & 0 & 0 & 0 & 0 & 225 \end{bmatrix} \quad (55)$$

These values of $\underline{Q}$, $\underline{R}$, and $\underline{P}(0)$ should give adequate filter performance to evaluate the four measurement policies.

Method of Evaluation

As stated in the introductory chapter, the goal of this thesis is to present a reasonable method for, and the results of, evaluating the dual-seeker concept for the

proposed missile. The truth model and EKF design, which were implemented as described in this chapter, provide the means for accomplishing this evaluation. The SOFEPL plots, discussed in the previous section, provide the means for presenting the evaluation graphically. The SOFEPL program outputs summary statistics of each plot so that numerical results are also available. These statistics for the results are presented in tabular form in the next chapter.

The statistics available from the SOFEPL output are the minimum, maximum, and time average of each curve plotted. Of the five curves on the plots used for this thesis, the statistics for the mean error and the mean error plus or minus the standard deviation of the mean error provide the best indication of how the filter is performing. For this reason, the following statistics will be used to evaluate the filter's performance for each measurement policy:

1) the time average of the mean error

2) the magnitude of the maximum mean error

3) the time average of the standard deviation of the mean error

4) the magnitude of the maximum of the mean error plus or minus one standard deviation

Because they include the statistics over the whole trajectory the time averages in 1) and 3) above are the best indication of overall filter performance. The maximums in 2) and 4) indicate the most serious instantaneous error committed by the filter. As will be

seen in the results, however, the random initial conditions often biased the time average of the mean error and both maximum values. Therefore, the comparisons are concentrated on the time average of the standard deviation. These statistics will be used in conjunction with the plots to compare the filter's performance for each measurement policy.

To simplify references to the measurement policies described in Chapter I, the numbers given in Table III will be used.

Table III

Measurement Policies

Policy	Description
1	Both seekers operative throughout flight
2	Strapdown seeker only until midflight, loss of strapdown and switch to gimballed seeker at midflight
3	Both seekers operative initially, loss of strapdown seeker at midflight
4	Strapdown seeker operating alone initially, gimballed seeker on at midflight

The midflight transition point was chosen to be 16 sec, because the semi-active laser seeker implemented in the LLLGB simulation acquired the target at that point in the trajectory. The missile-to-target range is approximately 8400 ft at the transition point. To enable direct comparisons between dissimilar policies, 16 sec is used as

the switching point both when the strapdown seeker loses track and when the gimballed seeker doesn't acquire the target until midflight.

The overall philosophy of performance evaluation can now be discussed. The filter performance will be evaluated both by a visual examination of the results' plots and by a numerical comparison of the statistics of the plots. The plots graphically portray the filter's performance and confidence at the end of the trajectory and the confidence gained (or lost) during the seeker switching points. Since the filter's performance is generally very good in the end conditions for all policies, no attempt will be made to measure numerically these results from the graphs. Instead, direct visual inspections provided adequate comparisons between policies in the end conditions. The tabulated statistics, especially the time average statistics, again, provided the best indication of filter performance over the whole trajectory. The statistics will be used to compare the overall performance in terms of maximum absolute values and percentage differences. Thus, it is important to consider both methods because each provides some information that the other does not.

Although the end conditions give the best indication of the filter's estimation at the impact point, better performance is desirable early in the trajectory because of energy considerations. If the filter's estimates converge very late in the trajectory, the missile may not have

enough energy or the aerodynamic capability to correct for early errors and steer to the target. Therefore, the filter's performance at the end of the trajectory and its performance overall will both be considered. When the filter's performance is described from the plots, "good" filter performance is characterized by the mean errors converging to essentially zero and by convergence of the standard deviations of the mean errors at the end (in the last several seconds) of the trajectory to small values in comparison to the initial errors. "Poorer" filter performance is characterized by non-zero-mean errors and larger standard deviations in the end conditions. Conceptually, the numerical results provided by the plot statistics can be thought of in terms of "error probability." If the average error and standard deviation (or, more exactly, the RMS value of the error) are within the kill radius of the missile warhead, the missile can be considered to have "hit" the target. Since no specific missile is considered in this thesis, an exact kill radius is not available. Therefore, filter performance comparisons derived from the plot statistics are described in terms of "percent improvement," with the realization that differences in small values may not be significant.

One final consideration in evaluating the filter's performance is, which filter states should be considered. In general, there is a direct correspondence between a velocity state and its respective position state. This

correspondence is evident in the tuning plots already discussed, and is due to the coupling between the position and velocity states seen in the filter dynamics equation, eq. (42). Because a comparison between velocity states does not provide any more information than a comparison between the corresponding position states, and vice versa, only the position states will be compared directly in the results. The complete set of plots for each measurement policy is included in the results for completeness, however.

Because of the lack of observability in the x-channel, the filter comparisons will not include consideration of the x-position (or velocity) state. As seen in Figures C-9, C-10, C-16, and C-17, for example, the filter's covariance indicates that the filter is not gaining any information about the x-channel until the very end of the flight. Although the errors are zero-mean for the x-channel in most of the plots, discussion of the x-channel for each of the policies would provide no meaningful comparisons between the policies. As seen in Figure 2-2, the lack of observability in x is due to the fact that the missile-to-target range vector is almost entirely along the x-direction at any point in the flight. Angular variations off this vector, such as provided by the two seekers, give little information about changes in x or v_x. The increase in observability in x at the end of the trajectory is due to the rotation of the range vector away

from the x-direction such that it has significant components in all three directions. The overall lack of observability in x (essentially range for this trajectory) demonstrates the classic problem of angle-only range estimation, which has been studied extensively (Refs 1;9;15;22;23).

Thus, comparisons between measurement policies in the results to follow will be made on the basis of the y-position and z-position states. As seen in their plots already discussed, these states are observable throughout the trajectory. For the filter formulation implemented for this study, comparisons of the filter's performance in the y and z states (filter states x_3 and x_5) provide a realistic basis for performance evaluation.

V. RESULTS

Introduction

This chapter is a discussion of the results of running the EKF designed in Chapter III against the truth model of Chapter II. Four sets of plots for the measurement policies listed in Table III in the previous chapter provide the basis for evaluating the filter design in general and for comparing the filter's performance for each policy. These plots are found in Appendix D. The summary statistics of the plots for states y and z are found in Table IV. As described in the previous chapter, the statistics given are the time average and maximum value of the mean error, the time average of the standard deviation of the mean error, and the maximum of the mean error plus or minus one standard deviation. The discussion of the results begins with an evaluation of the general performance of the filter over all the runs done for this study.

General Performance of the Filter

As seen in the tuning plots of Appendix C and in the results plots of Appendix D, the EKF design performs well except in the case of angle-rate measurements only, due to the observability problem (Figures C-23 through C-36). The tuning accomplished for this case gave reasonably well-bounded filter performance. Also, the angle-rate

Table IV. Statistics of Plots for the Results

State	Measurement Policy	Avg. of Error	Max. Error	Avg. of Std. Dev.	Max. error$\pm 1\sigma$
y	1	0.22 ft	12.1 ft	13.9 ft	96.4 ft
	2	8.33	47.3*	26.6	145.4*
	3	1.24	12.9	15.5	105.3
	4	1.92	33.5*	28.1	145.7*
z	1	3.42	46.5*	32.0	122.9*
	2	8.71	16.4	65.5	114.2
	3	2.64	24.7	30.2	115.3
	4	6.73	20.8	68.4	119.7

Note: All numbers are absolute values.

*These high values are due to the random initial conditions for the filter.

measurements are not used alone, but in conjunction with the angle measurements from the gimballed seeker truth model. The angle measurements are weighted more heavily (see eq. (53)) because of tuning considerations, and will, in effect "smooth" the poor performance due to the angle-rate measurements. The angle-rate measurements do provide some observability of the velocity states (see eq. (44)), which is a benefit of the gimballed seeker model over the strapdown seeker model and may contribute to the performance benefits of the gimballed seeker to be seen.

The general lack of observability in the x-channel no matter what measurement policy is employed, has already been discussed and is not unique to the filter design of this thesis (Ref 23). No attempt will be made here to compare this filter design to other angle-only range estimation algorithms. Although the EKF filter design employed in this thesis does not estimate range states (x-position and velocity) well, the observability of the y and z states does enable this filter design to be used for the desired analyses. This observability in y and z can easily be seen in the plots as the immediate convergence of the filter covariances from the initial uncertainties. The y and z states are observable because, given the relatively small initial uncertainty in x, the angular changes indicated by the measurement vector reflect position and velocity changes perpendicular to the range vector, or changes in y- and z-positions and velocities. The

observability in z decreases somewhat at the end of the trajectory because the range vector rotates and gains a significant component along the z-axis (See Figure 2-2). In general, the y and z state estimates converge well for all cases and are zero-mean at the end conditions.

As indicated by the statistics of Table IV, the overall filter performance for states y and z is quite good for all cases. Note that six values in the table are high due to the random initial conditions' not being zero-mean. Inspection of the plots for these cases show that the initial conditions are the maximum values. Though only the high maximum values are noted in Table IV, the average mean errors for these policies are necessarily increased by the biased initial conditions. As seen in the plots, the standard deviations of the initial conditions are much closer to the values indicated by the P matrix (eq. (47)). This fact alone motivates consideration of the average standard deviations as the most-representative statistics. In addition, even with the biasing on the average mean errors for some policies, all the average mean errors are relatively small (less than 10 ft) with respect to missile kill radii. Therefore, the best indication of filter performance from the statistics is provided by the average standard deviations. Note that the average standard deviation statistics are consistent between the two states, y and z, for corresponding policies, which provides additional confidence in the correctness of the filter

design. These statistics will now be used in conjunction with the plots to compare the filter's performance for each measurement policy.

Measurement Policy Comparisons

Overall. In general, one can expect better filter performance the greater the number of measurements available at each sample time. Given proper filter modelling and tuning, the filter will weight and incorporate each measurement made available to it. The basic Kalman filter is the optimal estimator (Ref 18:206): one is guaranteed better filter performance (in a minimum variance sense) the more measurements available, given proper modelling and tuning. Since the extended Kalman filter formulation is a linearization technique, it is not necessarily "optimal" (Ref 19:39-42). As has been seen, the EKF implemented in this thesis performs very well given the noisy measurements available from the truth model and the specific missile trajectory considered. Care must be exercised in making generalizations about measurement policies, however, since redundant measurements or measurements which are weighted less may not improve, and may perhaps degrade (in the case of mismodelling), the filter estimates for an EKF application. These considerations will be taken into account in making the following comparisons, which is the object of this study.

Between Policy 1 and Policy 3. To a degree, a comparison between measurement policies 1 and 3 demonstrates the degradation possible from additional measurements. Both of these policies involve use of the gimballed seeker throughout the flight, and the difference between them is that policy 1 involves use of the strapdown throughout, while, in policy 3, the strapdown seeker is lost at midflight. One would expect better performance from policy 1 since more measurements are available in it. In reality, the performance is almost exactly the same for both policies. An inspection of the plots (Figures D-1 through D-6 and D-13 through D-18) and the statistics (Table IV) reveal very similar performance for both policies. The inconsistency is seen in a comparison of the average standard deviations for the z-states. Policy 1's average standard deviation of 32.0 ft is 6% higher than that for policy 3, 30.2 ft. The values are so close, however, and the plots so identical, especially in the end conditions, that the filter performance in both cases is essentially the same. These results indicate that loss of the strapdown seeker in midflight does not affect filter performance.

Between Policy 2 and Policy 4. A comparison between the filter's performance for measurement policy 2 and its performance for policy 4 corroborates the results of the previous comparison between policies 1 and 3. The difference between policies 2 and 4 is that the latter set

involves the use of the strapdown seeker throughout the flight, while the strapdown seeker loses track at midflight in the former set. The gimballed seeker comes on in midflight in both policies. Again, the average standard deviations for these two policies indicate that the policy involving the fewest measurements gives slightly (about 5%) better performance. Again, also, the plots for policies 2 and 4 (Figures D-7 through D-12 and D-19 through D-24) are almost identical, and the average standard deviations for both y and z are very close for both policies (5.6% difference for y and 4.4% difference for z). Loss of the strapdown seeker seems to improve the filter performance slightly. However, close comparisons of corresponding plots reveal that the performance is essentially the same for both policies, especially in the end conditions, indicating again that loss of the strapdown seeker does not affect filter performance to any great degree.

The interesting effect to note in the plots for both policy 2 and policy 4 is the marked reduction in the filter covariance, $\underline{P}(t)$, curves when the gimballed seeker comes on at 16 sec. As seen in Figures D-9 and D-21, for example, there is a secondary transient in $\underline{P}(t)$ and the mean error at the transition point and then the statistics close in rapidly to the steady-state end conditions. This effect is due to the greater weighting placed on the gimballed seeker's angle measurements and the increased observability introduced by the gimballed seeker's angle-rate

measurements. Use of the gimballed seeker is assumed always to be possible from midflight on, but the major consideration here is its use before midflight. A comparison between policies 1 and 3 and policies 2 and 4 will provide an assessment of the use of the gimballed seeker early in the flight.

Between Policies 1 and 3 and Policies 2 and 4. Comparing policies 1 and 3, in which the gimballed seeker is used throughout the flight, to policies 2 and 4, in which the gimballed seeker is not used until 16 sec into the flight, shows that there is a distinct advantage to overall performance but very little benefit to the end performance for policies 1 and 3 over policies 2 and 4. The average standard deviations are approximately twice as great for policies 2 and 4, which indicates, as expected, that use of the gimballed seeker beginning at launch time greatly improves filter performance for the whole flight. The fact that both sets of average standard deviations for state y and for state z show a consistent improvement for policies 1 and 3 over policies 2 and 4 adds a great deal of confidence to the indicated benefit. An examination of the end conditions for all the plots reveals that there is really no advantage in policies 1 and 3 over policies 2 and 4 with regard to final errors. There is approximately a 10 to 20 ft improvement in z-position, a 2 to 3 ft/sec improvement in z-velocity, and no real improvement in

y-position or velocity standard deviations at the final time for policies 1 and 3.

The lack of improvement in the end conditions for the policies in which the gimballed seeker is tracking the entire time of flight as opposed to those in which it gains track in midflight is probably due to the length of the flight time remaining after 16 sec. The gimballed seeker is on for 12 sec before the end conditions are reached and has had time to bring the estimates to steady-state. Since the filter is not aware of the exact time-to-impact, use of the gimballed seeker's measurements as soon as they are available would increase the confidence in the end conditions, whenever they are reached. Also, the overall performance improvement indicated by the average standard deviations cannot be ignored. For all these reasons, incorporating the measurements from the gimballed seeker as soon as possible is highly recommended based on these results.

Summary

The results derived from the plots for the measurement policies have revealed important conclusions as to the value to be placed on the use of both seekers at specific times during the flight. The results have also given some insight into the adequacy of the EKF design of this thesis for the truth model and flight trajectory considered. The conclusions derived from these results are summarized in detail in the following chapter.

VI. CONCLUSIONS AND RECOMMENDATIONS

Introduction

The six-state extended Kalman filter designed in Chapter III was simulated as an estimator onboard a missile which flew the air-to-ground trajectory shown in Figure 2-2. The filter was provided with measurements from the strapdown seeker and gimballed seeker truth models (Figures 2-9 and 2-13) developed in Chapter II. The measurements were made available as specified in the measurement policies introduced in Chapter I and tabulated in Table III of Chapter IV. The filter and truth models were implemented as a digital computer simulation according to the implementation considerations presented in Chapter IV. The filter was tuned in a Monte Carlo analysis against the truth model as also discussed in Chapter IV. Simulations were run to obtain comparisons for the four measurement policies as described in Chapter V. This chapter presents the conclusions drawn from the results and the recommendations for expanding on the work done for this study.

Conclusions

The EKF design performed well in estimating the y- and z-position and velocity states. Since the missile velocity vector lay almost completely in the x-direction and only angle and angle-rate measurements were available, the

filter could not estimate the x-position and velocity states until the last 6 sec of the trajectory. It began estimating the x-states at this point because the range vector rotated such that its x-component decreased with respect to its y- and z-components. The observability problem in x was to be expected with only angular measurements available.

The use of simulated, random, Gaussian-distributed initial conditions resulted in a biasing of the statistics taken from the plots for the results. The standard deviations of the initial conditions were very consistent and the average mean errors were less than 10 ft, so that the average standard deviations were the most indicative of performance out of all the statistics considered. Comparisons of the average standard deviations for the y- and z-position states gave good indications of overall filter performance for each policy. Visual comparisons of the plots provided performance evaluations in the end conditions.

The following comparisons provided insight into the potential benefits of the use of the seekers:

1) Between policy 1 and policy 3: gimballed seeker on throughout flight for both, strapdown on initially for both, but off at midflight for policy 3

2) Between policy 2 and policy 4: gimballed seeker on at midflight for both, strapdown seeker on initially for both, but off at midflight for policy 2

3) Between policies 1 and 3 and policies 2 and 4 collectively: gimballed seeker on throughout flight for former set, does not come on until midflight for latter set

The conclusions drawn from these comparisons are as follows:

1) Loss of the strapdown seeker at midflight (16 sec) does not degrade filter performance substantially.

2) Use of the gimballed seeker's measurements starting at the launch point substantially improved overall filter performance over their use beginning at midflight.

3) Use of the gimballed seeker's measurements starting at the launch point rather than at midflight does not appreciably improve filter performance at the end conditions.

Recommendations

Based on the conclusions presented and the insight gained from this work, the following recommendations are made to guide future studies on the dual-seeker concept:

1) Different sets of initial conditions and, perhaps, different trajectories should be used to examine the observability problem more fully.

2) The filter should be implemented in a closed-loop guidance law to analyze further the measurements that are available from the two seekers.

3) Future advances in strapdown seeker technology, especially in deriving inertial LOS rates from a body-fixed sensor, should be considered in future studies on the dual-seeker concept.

Bibliography

1. Aidala, V. J. "Kalter Filter Behavior in Bearings-Only Tracking Application," IEEE Transactions on Aerospace and Electronics Systems, AES-15: 29-39 (January 1979).

2. Barton, David K. Radar System Analysis. Englewood Cliffs, New Jersey: Prentice-Hall, Inc., April 1965.

3. Capps, D. W. and Nelson, D. C. A Comparative Analysis of Kalman Filters Using a Hypervelocity Missile Simulation. MS thesis. Wright-Patterson AFB, Ohio: Air Force Institute of Technology, December 1981.

4. Conversation with Mr. Phil Richter, Senior Engineer, Terminal Guidance, Air Force Armament Test Laboratories, Eglin AFB, Florida.

5. Cusumano, S. J. and De Ponte, M. An Extended Kalman Filter Fire Control System Against Air-to-Air Missiles. MS thesis. Wright-Patterson AFB, Ohio: Air Force Institute of Technology, December 1977. (AD A055 179)

6. Ehrich, R. D. and Vergez, P. "Strapdown Seeker Technology for the Terminal Guidance of Tactical Weapons," AGARD-CP-292 Guidance and Control Aspects of Tactical Air-Launched Missiles. Neuilly Sur Seine, France: AGARD, October 1980. (AD A092 606)

7. Electro-Optics Seeker Department, Low-Level Laser-Guided Bomb Program Technical Report - Analysis Data, Vol IV. Air Force Armament Test Laboratories-sponsored document. Dallas, Texas: Electro-Optics Department, Texas Instruments Corporation, 20 June 1980.

8. Emmert, R. I. and Ehrich, R. D. Strapdown Seeker Guidance for Air-to-Surface Tactical Weapons. AFATL-TR-78-60 Report for Air Force Armament Laboratory. Columbus, Ohio: Missile Systems Division, Rockwell International, May 1978. (AD B030 995)

9. Fagerlund, S. Target Tracking Based on Bearing Only Measurements, Technical Report LIDS-R-1003, Massachusetts Institute of Technology, Laboratory for Information and Decision Systems, June 1980. (AD A100 736)

10. Feagler, E. R. "The Interferometer as a Sensor for Missile Guidance." Short course notes on missile guidance presented to Foreign Technology Division. Wright-Patterson AFB, Ohio, August 11-14, 1981.

11. Gelb, Arthur. Applied Optimal Estimation. Cambridge, Massachusetts: The M.I.T. Press, 1974.

12. Gonzalez, J. "New Methods in the Terminal Guidance and Control of Tactical Missiles," AGARD-LS-101 Guidance and Control for Tactical Guided Weapons with Emphasis on Simulation and Testing. Neuilly Sur Seine, France: AGARD, May 1979. (AD A071 129)

13. Gulick, J. "Angle Measurement and Processing with Body Fixed Antennas." Short course notes on missile guidance presented to Foreign Technology Division. Wright-Patterson AFB, Ohio, August 11-14, 1981.

14. Hlavaty, C. W. A Practical Three Dimensional, 11 State Extended Kalman Filter for Use in a Fire Control System Against Nonthrusting Missiles. MS thesis. Wright-Patterson AFB, Ohio: Air Force Institute of Technology, December 1978. (AD A064 759)

15. Lindgren, A. G. and K. F. Gong. "Position and Velocity Estimation Via Bearing Observations," IEEE Transactions on Aerospace and Electronics Systems, AES-14:564-577 (July 1978).

16. Low-Level Laser-Guided Bomb Six Degree-of-Freedom Flight Simulation. AFATL-TR-82-48. Document to be published by Air Force Armament Test Laboratories, Eglin AFB, Florida.

17. Lutter, R. N. Application of an Extended Kalman Filter to an Advanced Fire Control System. MS thesis. Wright-Patterson AFB, Ohio: Air Force Institute of Technology, December 1976. (AD A035 293)

18. Maybeck, Peter S. Stochastic Models, Estimation, and Control, Vol I. New York: Academic Press, Inc., 1979.

19. Maybeck, Peter S. Stochastic Models, Estimation, and Control, Vol II. New York: Academic Press, Inc., 1982.

20. Musick, Stanton H. SOFE: A Generalized Digital Simulation for Optimal Filter Evaluation, User's Manual, AFWAL-TR-80-1108, Wright-Patterson AFB, Ohio, October 1980.

21. Musick, Stanton, H., et al. SOFEPL: A Plotting Postprocessor for "SOFE," User's Manual, AFWAL-TR-80-1109, Wright-Patterson AFB, Ohio, November 1981.

22. Nardone, S. C. and V. J. Aidala. "Observability Criteria for Bearings-Only Target Motion Analysis," IEEE Transactions on Aerospace and Electronics Systems, AES-17:162-166 (March 1981).

23. Stiffler, D. S. Analysis of Six Algorithms for Bearings-Only Ranging in an Air-to-Air Environment. Unpublished MS thesis. Wright-Patterson AFB, Ohio: Air Force Institute of Technology, December 1982.

24. Wauer, John C. "Practical Considerations in Implementing Kalman Filters," Practical Aspects of Kalman Filtering Implementation. Neuilly Sur Seine, France: Advisory Group for Aerospace Research and Development, March 1976. (AD A024 377)

25. Worsley, William H. Comparison of Three Extended Kalman Filters for Air-to-Air Tracking. MS thesis. Wright-Patterson AFB, Ohio: Air Force Institute of Technology, December 1980. (AD A094 767)

APPENDIX A

Calculating LOS Angles

Given LOS azimuth and elevation angles, α and ε relative to one coordinate axes, calculate LOS angles relative to the desired set of axes. Referring to Figure 2-5, the coordinate transformation matrix between the LOS frame L and an arbitrary reference frame A is given by:

$$\underline{V}^A = \begin{bmatrix} \cos\varepsilon & 0 & -\sin\varepsilon \\ 0 & 1 & 0 \\ \sin\varepsilon & 0 & \cos\varepsilon \end{bmatrix} \begin{bmatrix} \cos\alpha & -\sin\alpha & 0 \\ \sin\alpha & \cos\alpha & 0 \\ 0 & 0 & 1 \end{bmatrix} \underline{V}^L \qquad \text{(A-1)}$$

$$\underline{V}^A = C_L^A \underline{V}^L$$

where $\underline{V}$ is an arbitrary vector coordinatized in the frame indicated by the superscript. The transformation matrix from the LOS frame to the reference frame is, therefore,

$$C_L^A = \begin{bmatrix} \cos\alpha\cos\varepsilon & -\sin\alpha\cos\varepsilon & -\sin\varepsilon \\ \sin\alpha & \cos\alpha & 0 \\ \cos\alpha\sin\varepsilon & -\sin\alpha\sin\varepsilon & \cos\varepsilon \end{bmatrix} \qquad \text{(A-2)}$$

A unit vector (denoted by $\hat{}$) along the LOS coordinatized in the reference frame is expressed as:

$$\hat{LOS}^A = C_L^A \hat{LOS}^L = C_L^A \begin{bmatrix} 1 \\ 0 \\ 0 \end{bmatrix} = \begin{bmatrix} \cos\alpha\cos\varepsilon \\ \sin\alpha \\ \cos\alpha\sin\varepsilon \end{bmatrix} \qquad \text{(A-3)}$$

This vector can be expressed in the coordinates of some

other reference frame B by the Euler transformation between the frames, such as given in eq. (1). Defining the coordinate transformation between frames A and B as:

$$\underline{v}^B = C_A^B \underline{v}^A = \begin{bmatrix} C_{11} & C_{12} & C_{13} \\ C_{21} & C_{22} & C_{23} \\ C_{31} & C_{32} & C_{33} \end{bmatrix} \underline{v}^A \qquad \text{(A-4)}$$

The unit vector $\hat{LOS}^A$ is coordinatized in the B frame by

$$\hat{LOS}^B = \begin{bmatrix} LOS_x^B \\ LOS_y^B \\ LOS_z^B \end{bmatrix} = \begin{bmatrix} C_{11} & C_{12} & C_{13} \\ C_{21} & C_{22} & C_{23} \\ C_{31} & C_{32} & C_{33} \end{bmatrix} \begin{bmatrix} \cos\alpha\cos\varepsilon \\ \sin\alpha \\ \cos\alpha\sin\varepsilon \end{bmatrix}$$

$$= \begin{bmatrix} C_{11}c\alpha c\varepsilon + C_{12}s\alpha + C_{13}c\alpha s\varepsilon \\ C_{21}c\alpha c\varepsilon + C_{22}s\alpha + C_{23}c\alpha s\varepsilon \\ C_{31}c\alpha c\varepsilon + C_{32}s\alpha + C_{33}c\alpha s\varepsilon \end{bmatrix} \qquad \text{(A-5)}$$

using the abbreviations "c" for "cos" and "s" for "sin."

With the components of the unit vector of the LOS referenced to the desired frame B defined by eq. (A-5), the azimuth and elevation angles of the LOS relative to the B-frame axes are given by:

$$\alpha' = \tan^{-1}\left[\frac{LOS_y^B}{LOS_x^B}\right] \qquad \text{(A-6)}$$

$$\varepsilon' = \tan^{-1}\left[\frac{LOS_z^B}{\left[(LOS_x^B)^2 + (LOS_y^B)^2\right]^{1/2}}\right] = \sin^{-1}\left[LOS_z^B\right] \qquad \text{(A-7)}$$

APPENDIX B

Filter Measurement Matrix

This appendix covers the development of the measurement matrix $\underline{H}[t_i;\hat{\underline{x}}(t_i^-)]$ for the filter update.

As given in Chapter III, $\underline{H}[t_i;\hat{\underline{x}}(t_i^-)]$ is defined as:

$$\underline{H}[t_i;\hat{\underline{x}}(t_i^-)] = \left.\frac{\partial \underline{h}[\underline{x}(t_i),t_i]}{\partial \underline{x}}\right|_{\underline{x}=\underline{\hat{x}}(t_i^-)} \tag{37}$$

and, from eq. (44), $\underline{h}[\underline{x}(t_i),t_i]$ is:

$$\underline{h}[\underline{x}(t_i),t_i] = \begin{bmatrix} \tan^{-1}\left[\dfrac{C_4x_1+C_5x_3+C_6x_5}{C_1x_1+C_2x_3+C_3x_5}\right] \\ \tan^{-1}\left[\dfrac{C_7x_1+C_8x_3+C_9x_5}{\{(C_1x_1+C_2x_3+C_3x_5)^2+(C_4x_1+C_5x_3+C_6x_5)^2\}^{\frac{1}{2}}}\right] \\ \tan^{-1}\left[\dfrac{x_3}{x_1}\right] \\ \tan\left[\dfrac{x_5}{(x_1^2+x_3^2)^{\frac{1}{2}}}\right] \\ \dfrac{x_1x_4-x_2x_3}{x_1^2+x_3^2} \\ \dfrac{(x_1^2+x_3^2)x_6-(x_1x_2+x_3x_4)x_5}{(x_1^2+x_3^2)^{\frac{1}{2}}(x_1^2+x_3^2+x_5^2)} \end{bmatrix} \tag{B-1}$$

where, again, the coefficients C_1 through C_9 are the elements of the transformation matrix from the missile frame to the body frame defined in eq. (1) and described on page 16. The partial derivatives as defined by eq. (37) yield a 6 x 6 $\underline{H}[t_i;\underline{\hat{x}}(t_i^-)]$ matrix for the 6-state, 6-measurement filter model of this thesis. An example of the evaluation of $\underline{H}[t_i;\underline{\hat{x}}(t_i^-)]$ is (choosing element H_{33} arbitrarily):

$$H_{33} = \frac{\partial h_3}{\partial x_3} = \frac{\partial}{\partial x_3}\left[\tan^{-1}\left[\frac{x_3}{x_1}\right]\right]$$

$$= \frac{1}{1+\left(\frac{x_3}{x_1}\right)^2}\ \frac{\partial}{\partial x_3}\left[\frac{x_3}{x_1}\right]$$

$$= \frac{1}{1+\left(\frac{x_3}{x_1}\right)^2}\ \left(\frac{1}{x_1}\right)$$

$$= \frac{x_1}{x_1^2+x_3^2} \qquad \text{(B-19)}$$

Following this procedure, all 36 elements of $\underline{H}[t_i;\underline{\hat{x}}(t_i^-)]$ are given as follows:

Defining:

$$x' = C_1x_1+C_2x_3+C_3x_5 \qquad \text{(B-2)}$$

$$y' = C_4x_1+C_5x_3+C_6x_5 \qquad \text{(B-3)}$$

$$z' = C_7x_1+C_8x_3+C_9x_5 \qquad \text{(B-4)}$$

$$H_{11} = \frac{C_1x'-C_1y'}{x'^2+y'^2} \qquad \text{(B-5)}$$

$$H_{12} = 0 \tag{B-6}$$

$$H_{13} = \frac{C_5 x' - C_2 y'}{x'^2 + y'^2} \tag{B-7}$$

$$H_{14} = 0 \tag{B-8}$$

$$H_{15} = \frac{C_6 x' - C_3 y'}{x'^2 + y'^2} \tag{B-9}$$

$$H_{16} = 0 \tag{B-10}$$

$$H_{21} = \frac{C_7(x'^2 + y'^2) - z'(C_1 x' + C_4 y')}{(x'^2 + y'^2)^{\frac{1}{2}}(x'^2 + y'^2 + z'^2)} \tag{B-11}$$

$$H_{22} = 0 \tag{B-12}$$

$$H_{23} = \frac{C_8(x'^2 + y'^2) - z'(C_2 x' + C_5 y')}{(x'^2 + y'^2)^{\frac{1}{2}}(x'^2 + y'^2 + z'^2)} \tag{B-13}$$

$$H_{24} = 0 \tag{B-14}$$

$$H_{25} = \frac{C_9(x'^2 + y'^2) - z'(C_3 x' + C_6 y')}{(x'^2 + y'^2)^{\frac{1}{2}}(x'^2 + y'^2 + z'^2)} \tag{B-15}$$

$$H_{26} = 0 \tag{B-16}$$

$$H_{31} = \frac{-x_3}{x_1^2 + x_3^2} \tag{B-17}$$

$$H_{32} = 0 \tag{B-18}$$

$$H_{33} = \frac{x_1}{x_1^2 + x_3^2} \tag{B-19}$$

$$H_{34} = 0 \tag{B-20}$$

$$H_{35} = 0 \tag{B-21}$$

$$H_{36} = 0 \tag{B-22}$$

$$H_{41} = \frac{-x_1 x_5}{(x_1^2+x_3^2)\ (x_1^2+x_3^2+x_5^2)} \tag{B-23}$$

$$H_{42} = 0 \tag{B-24}$$

$$H_{43} = \frac{-x_3 x_5}{(x_1^2+x_3^2)^{\frac{1}{2}}(x_1^2+x_3^2+x_5^2)} \tag{B-25}$$

$$H_{44} = 0 \tag{B-26}$$

$$H_{45} = \frac{(x_1^2+x_3^2)^{\frac{1}{2}}}{(x_1^2+x_3^2+x_5^2)} \tag{B-27}$$

$$H_{46} = 0 \tag{B-28}$$

$$H_{51} = \frac{2x_1 x_2 x_3 + (x_3^2 - x_1^2)x_4}{(x_1^2+x_3^2)^2} \tag{B-29}$$

$$H_{52} = \frac{-x_3}{x_1^2+x_3^2} \tag{B-30}$$

$$H_{53} = \frac{(x_3^2 - x_1^2)x_2 - 2x_1 x_3 x_4}{(x_1^2+x_3^2)^2} \tag{B-31}$$

$$H_{54} = \frac{x_1}{x_1^2+x_3^2} \tag{B-32}$$

$$H_{55} = 0 \tag{B-33}$$

$$H_{56} = 0 \tag{B-34}$$

$$H_{61} = \frac{(x_1^2+x_3^2+x_5^2)(2x_1x_6-x_2x_5)+x_1[\cdot]\left[2+\frac{x_1^2+x_3^2+x_5^2}{x_1^2+x_3^2}\right]}{(x_1^2+x_3^2)^{\frac{1}{2}}(x_1^2+x_3^2+x_5^2)^2} \tag{B-35}$$

$$[\cdot] = [(x_1x_2+x_3x_4)x_5-(x_1^2+x_3^2)x_6]$$

$$H_{62} = \frac{-x_1x_5}{(x_1^2+x_3^2)^{\frac{1}{2}}(x_1^2+x_3^2+x_5^2)} \tag{B-36}$$

$$H_{63} = \frac{(x_1^2+x_3^2+x_5^2)(2x_3x_6-x_4x_5)+x_3[\cdot]\left[2+\frac{x_1^2+x_3^2+x_5^2}{x_1^2+x_3^2}\right]}{(x_1^2+x_3^2)^{\frac{1}{2}}(x_1^2+x_3^2+x_5^2)} \tag{B-37}$$

$$H_{64} = \frac{-x_3x_5}{(x_1^2+x_3^2)^{\frac{1}{2}}(x_1^2+x_3^2+x_5^2)} \tag{B-38}$$

$$H_{65} = \frac{2x_5[\cdot]-(x_1^2+x_3^2+x_5^2)(x_1x_2+x_3x_4)}{(x_1^2+x_3^2)^{\frac{1}{2}}(x_1^2+x_3^2+x_5^2)} \tag{B-39}$$

$$H_{66} = \frac{(x_1^2+x_3^2)^{\frac{1}{2}}}{x_1^2+x_3^2+x_5^2} \tag{B-40}$$

In summary, this appendix is the development of the measurement matrix $\underline{H}[t_i;\hat{\underline{x}}(t_i^-)]$ for the filter update. The elements of the $\underline{H}$ matrix listed as eqs. (B-5) through (B-40) are evaluated at t_i^- with $\hat{\underline{x}}(t_i^-)$ each filter update cycle. The matrix $\underline{H}$ thus calculated is then used to calculate the filter gain $\underline{K}(t_i)$ and to update $\underline{P}(t_i^-)$ as shown in eqs. (36) and (39).

APPENDIX C

Filter Tuning Plots

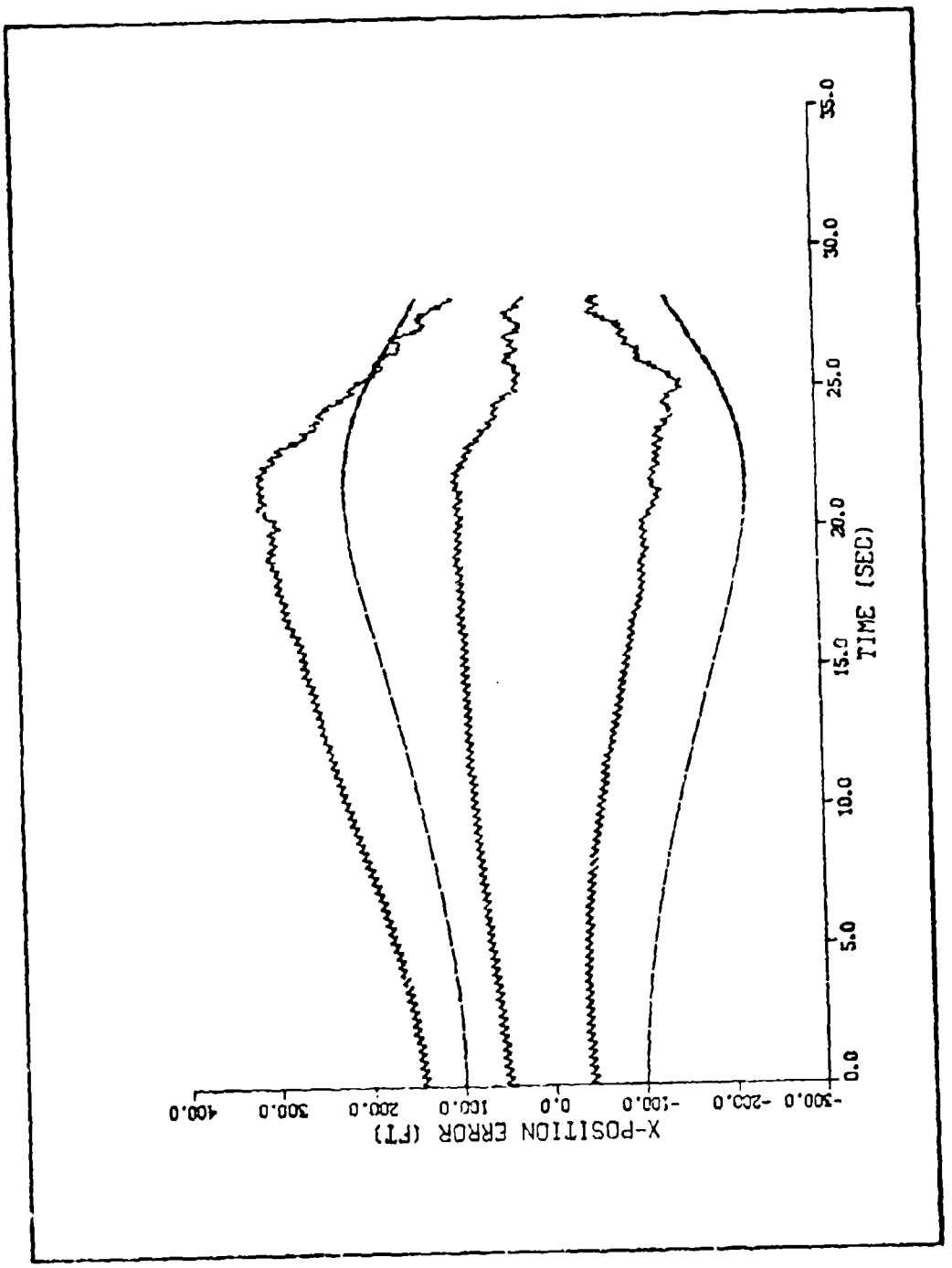

Figure C-1. Both Seekers, Initial Tuning Plots

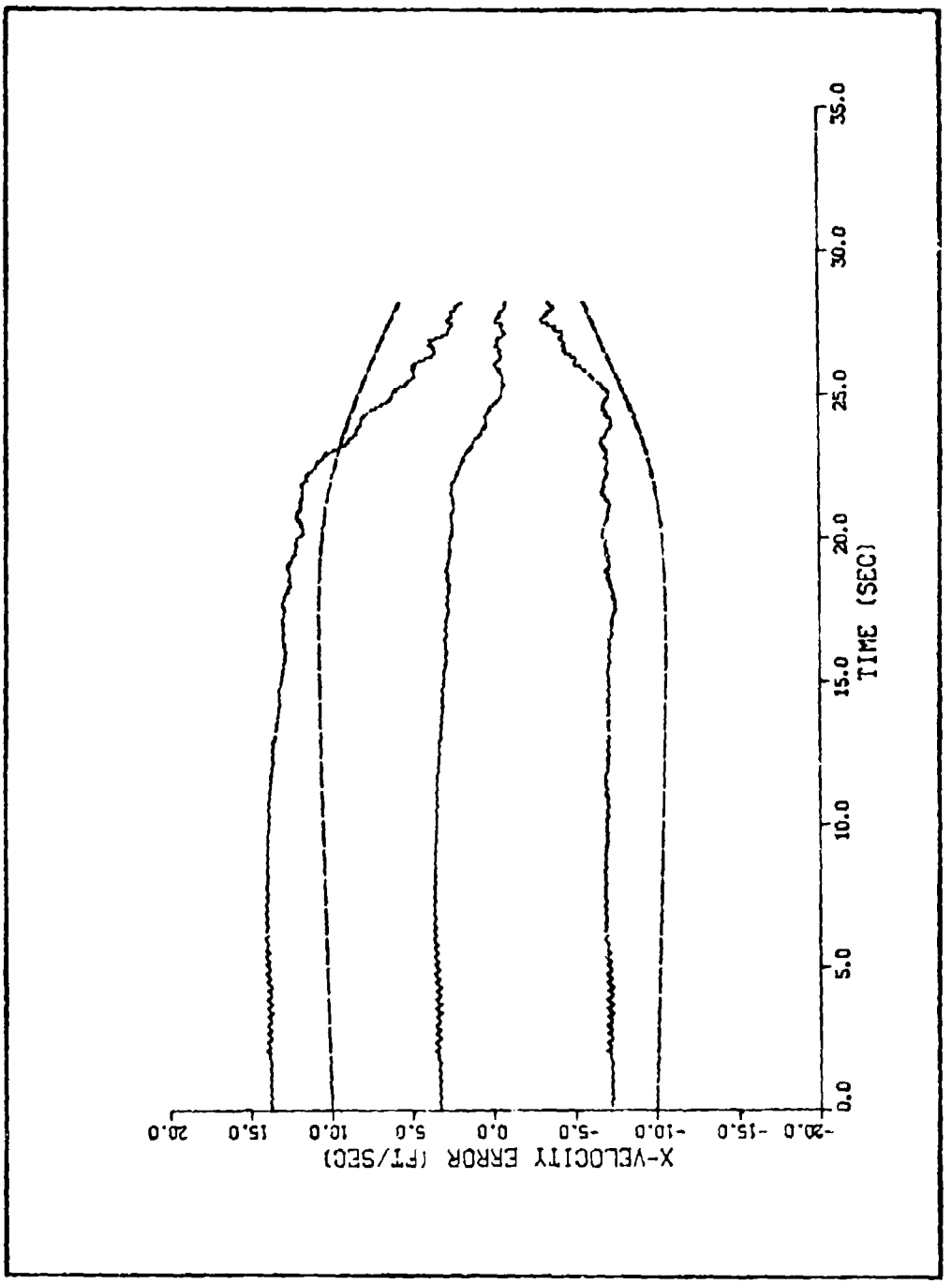

Figure C-2. Both Seekers, Initial Tuning Plots

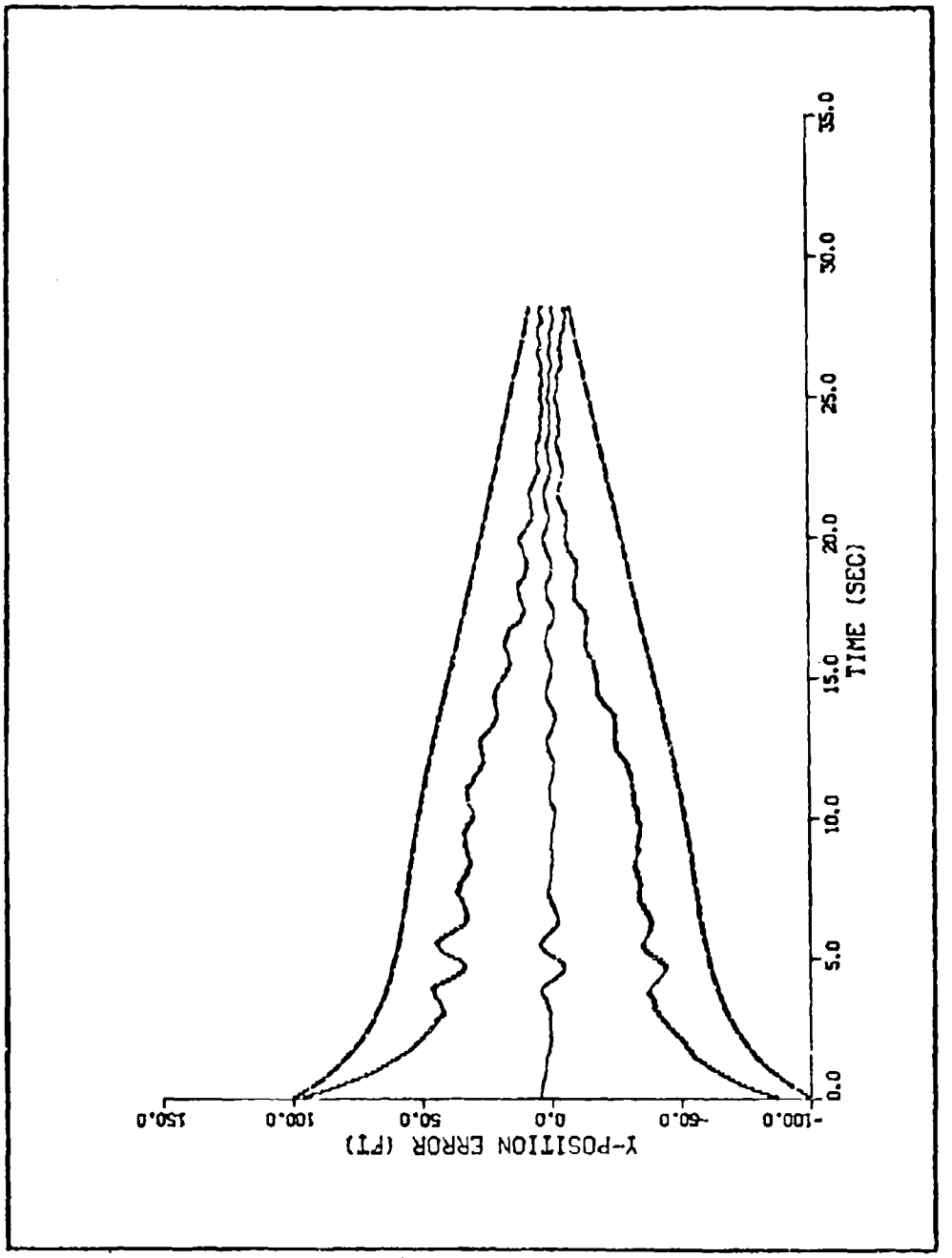

Figure C-3. Both Seekers, Initial Tuning Plots

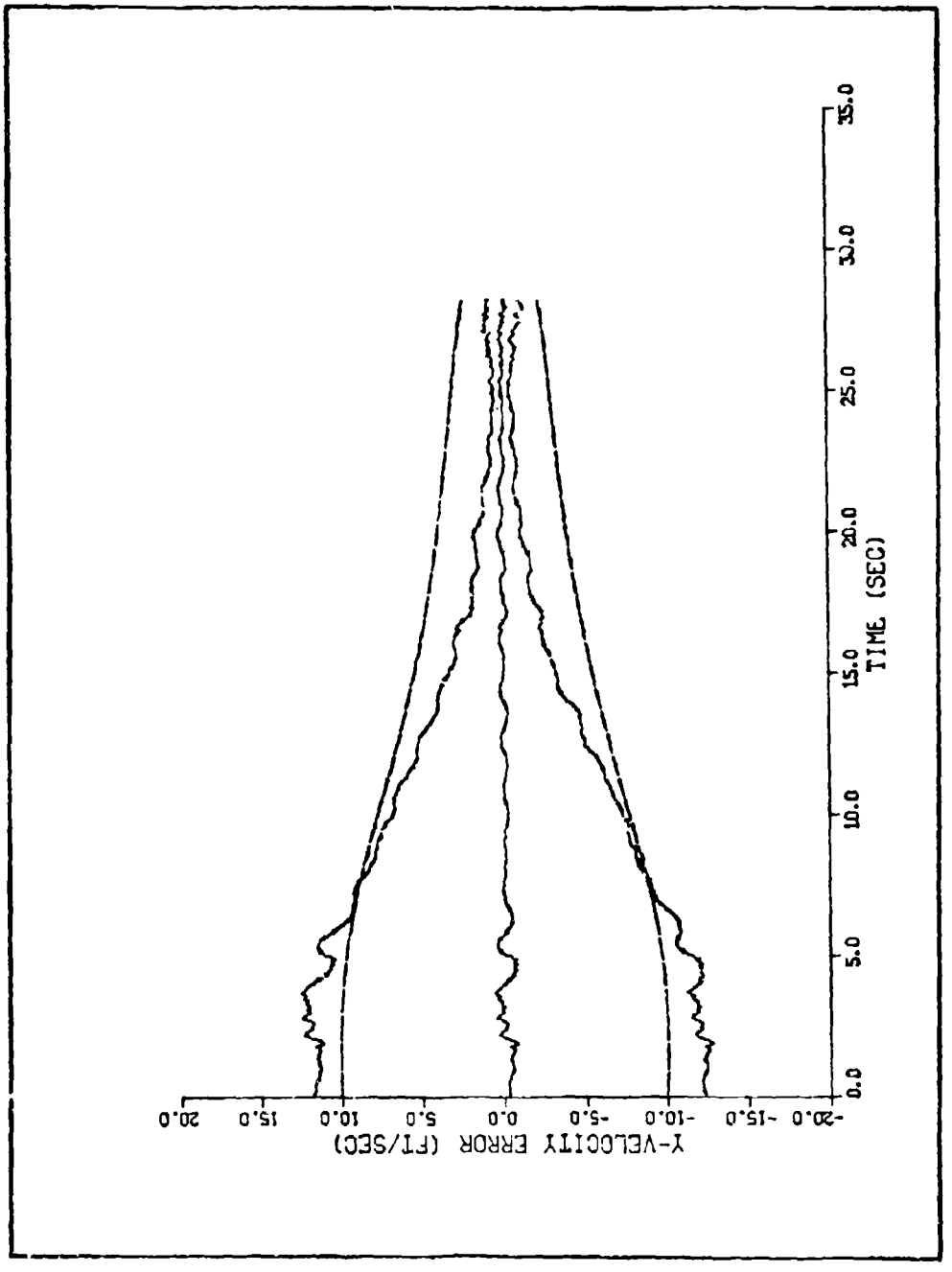

Figure C-4. Both Seekers, Initial Tuning Plots

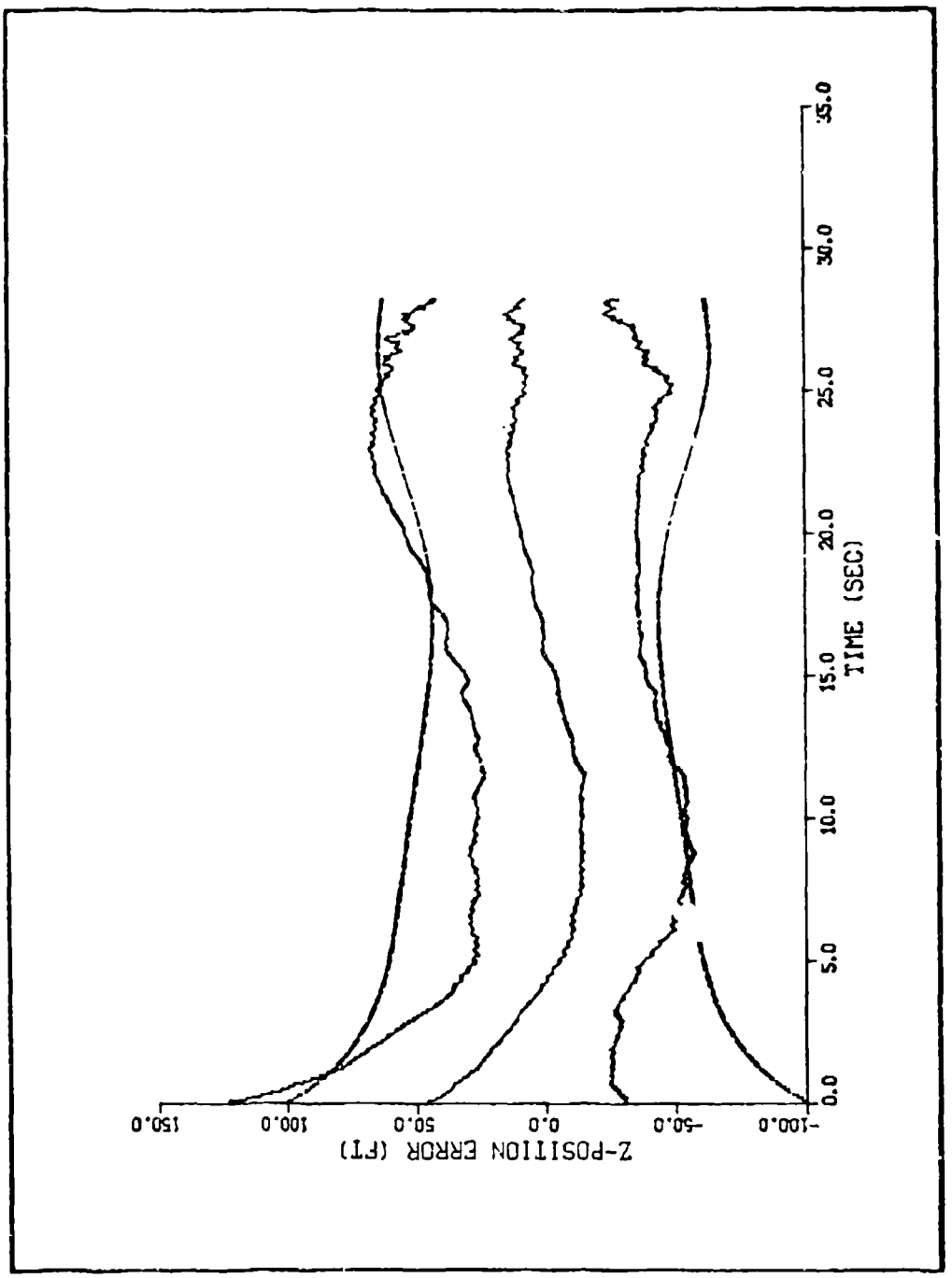

Figure C-5. Both Seekers, Initial Tuning Plots

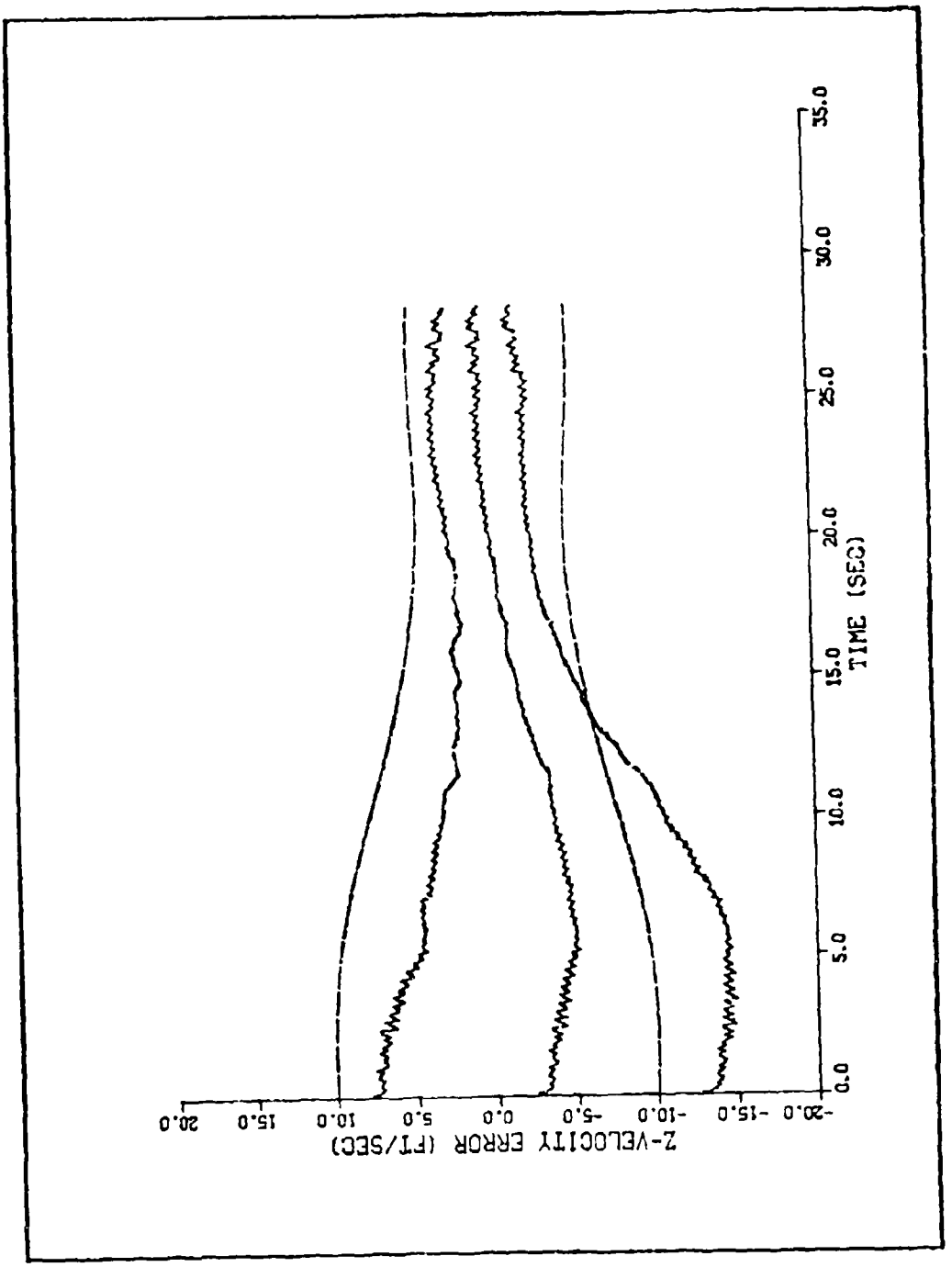

Figure C-6. Both Seekers, Initial Tuning Plots

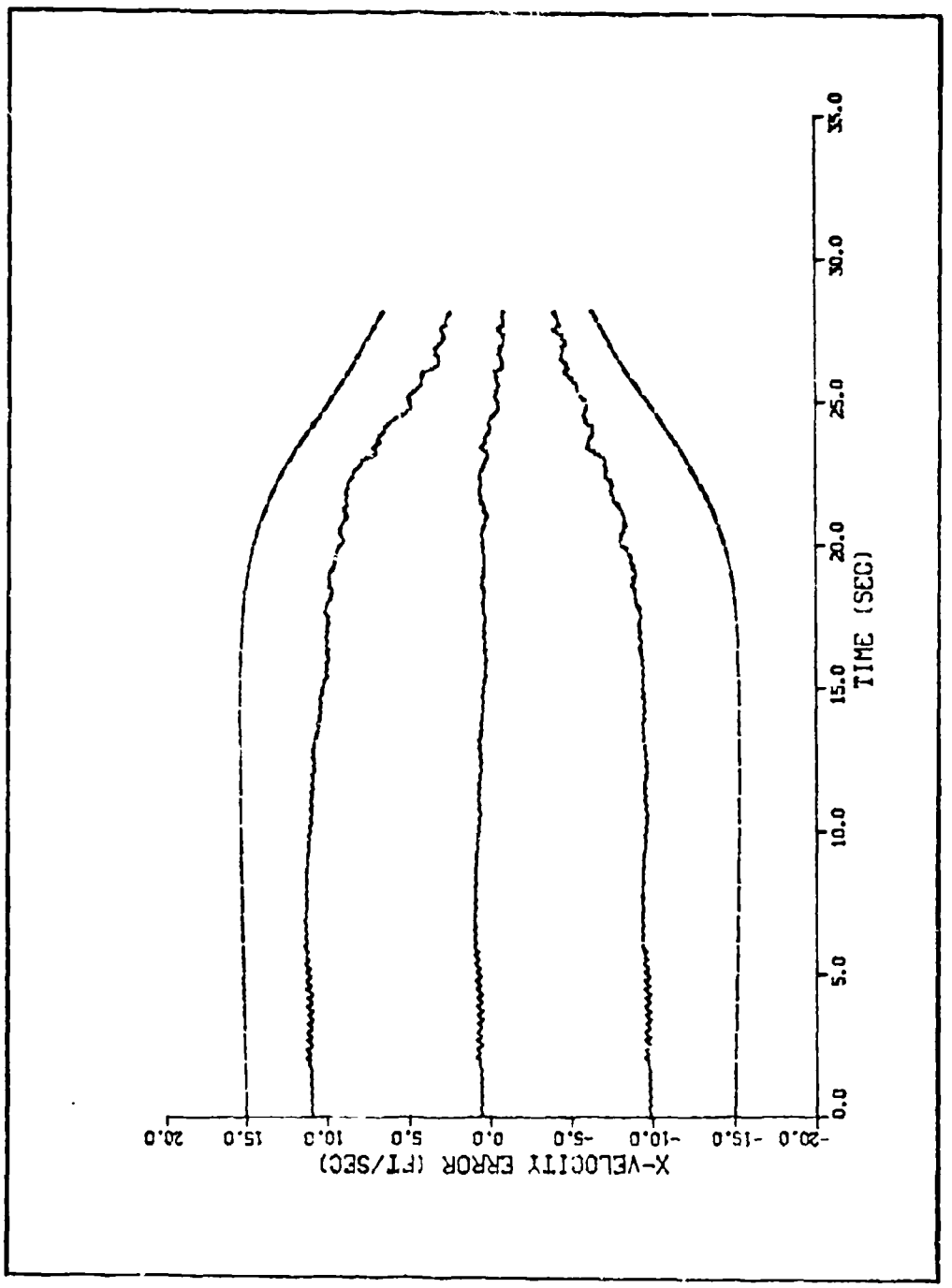

Figure C-7. Both Seekers, 50 Runs

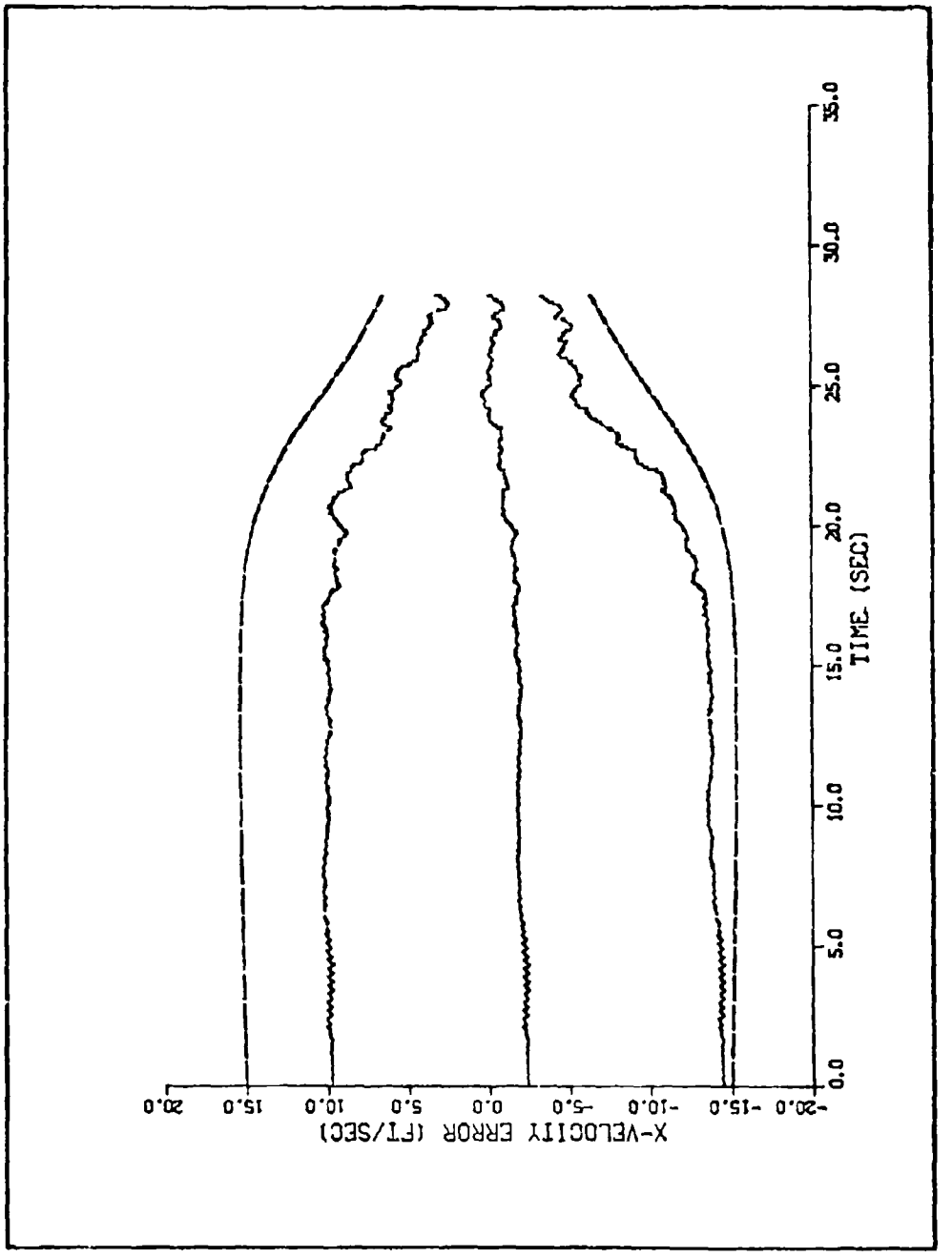

Figure C-8. Both Seekers, Different Seed for Random Number Generator

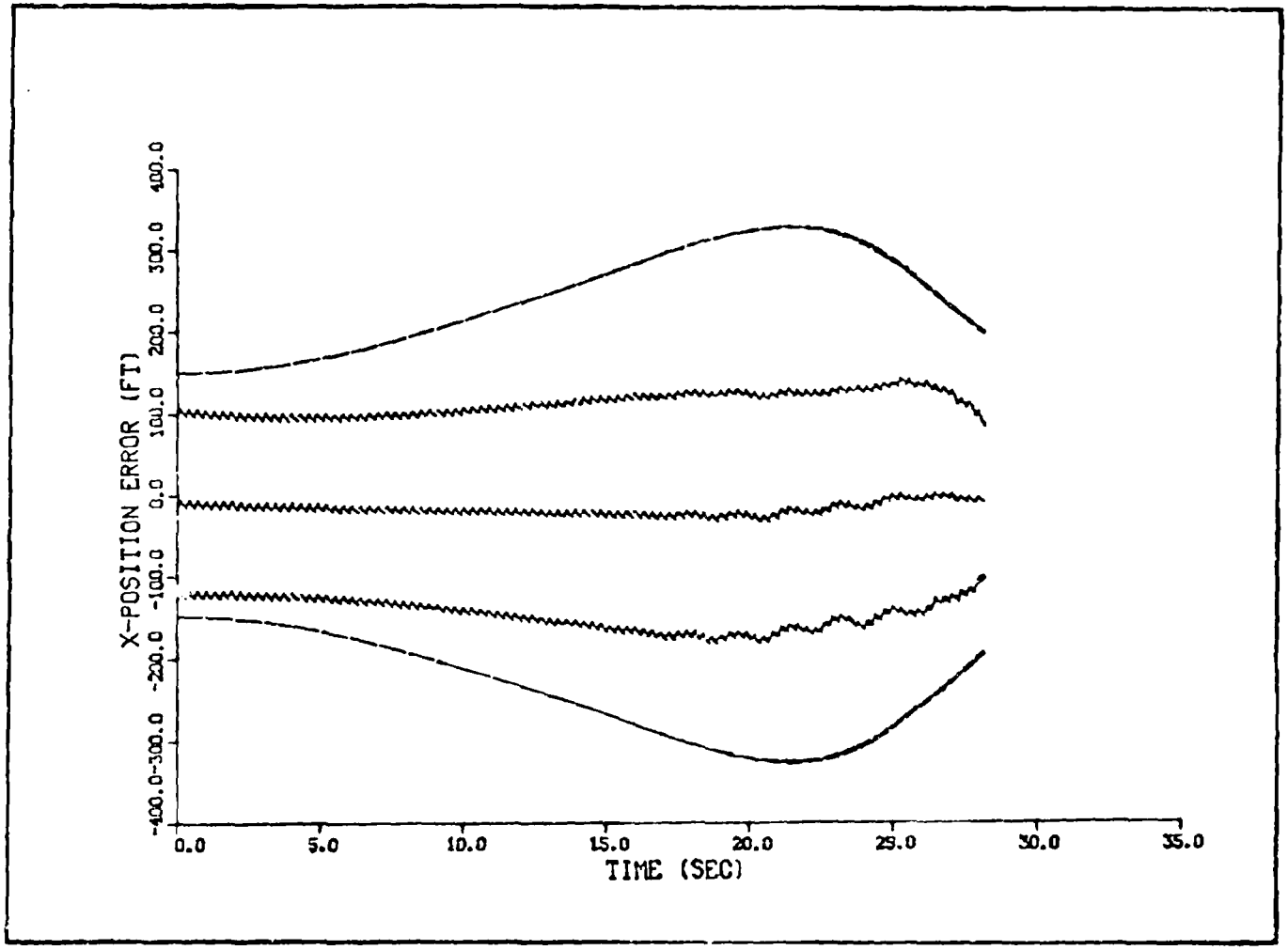

Figure C-9. Strapdown Seeker Only, B_1=.00125 rad^2

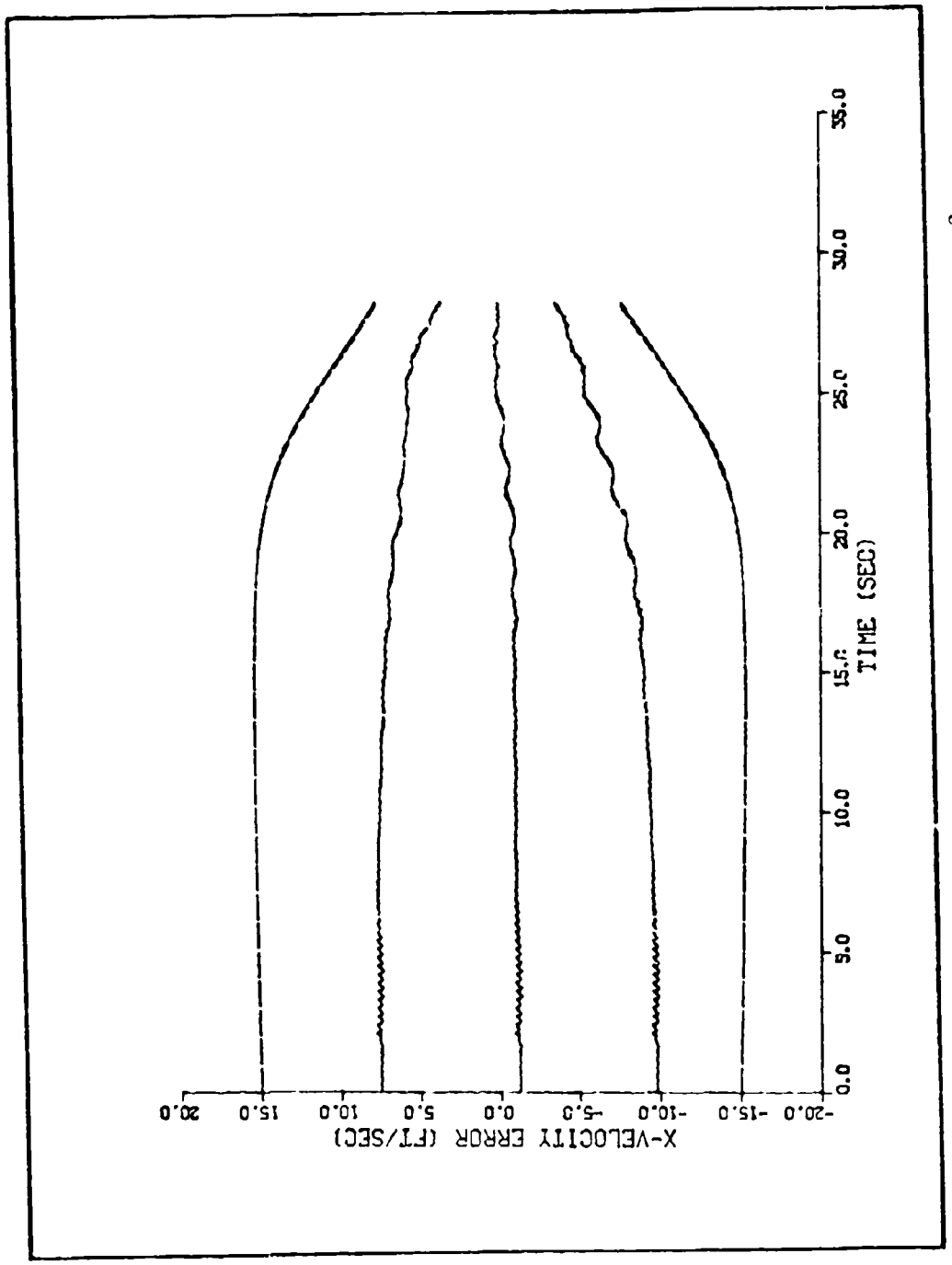

Figure C-10. Strapdown Seeker Only, $R_1 = .00125$ rad^2

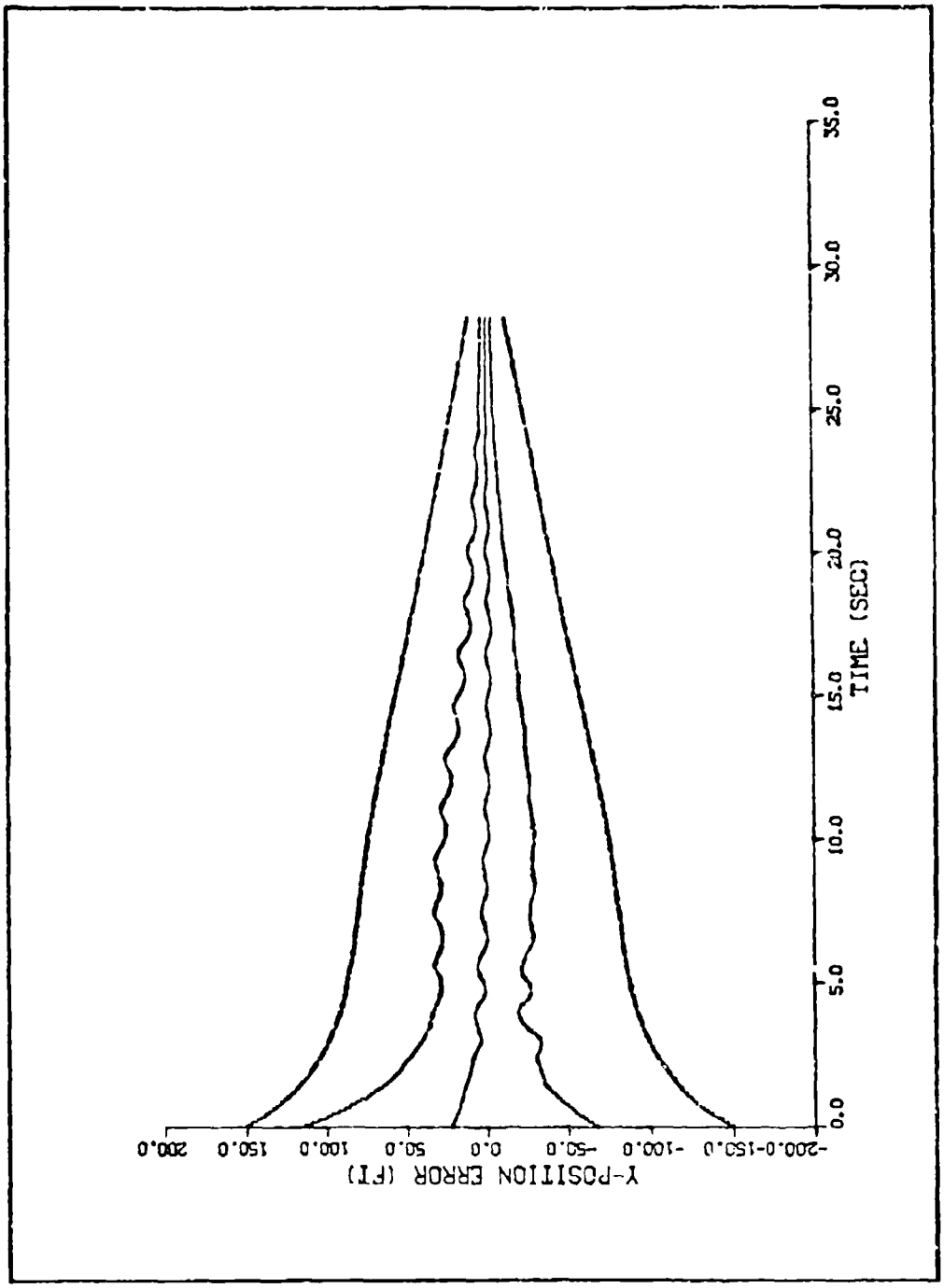

Figure C-11. Strapdown Seeker Only, $R_1 = .00125$ rad^2

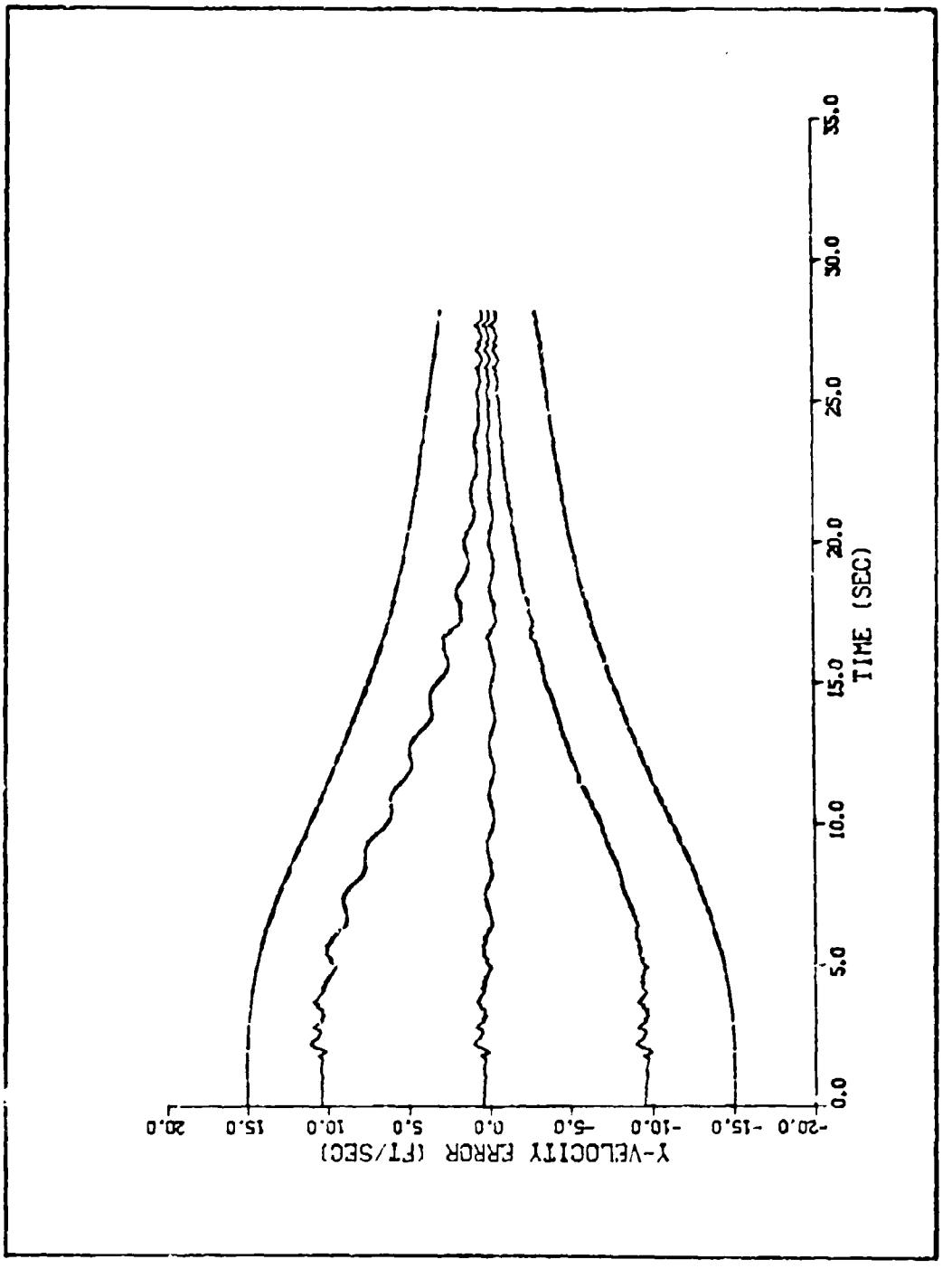

Figure C-12. Strapdown Seeker Only, $R_J = .00125$ rad^2

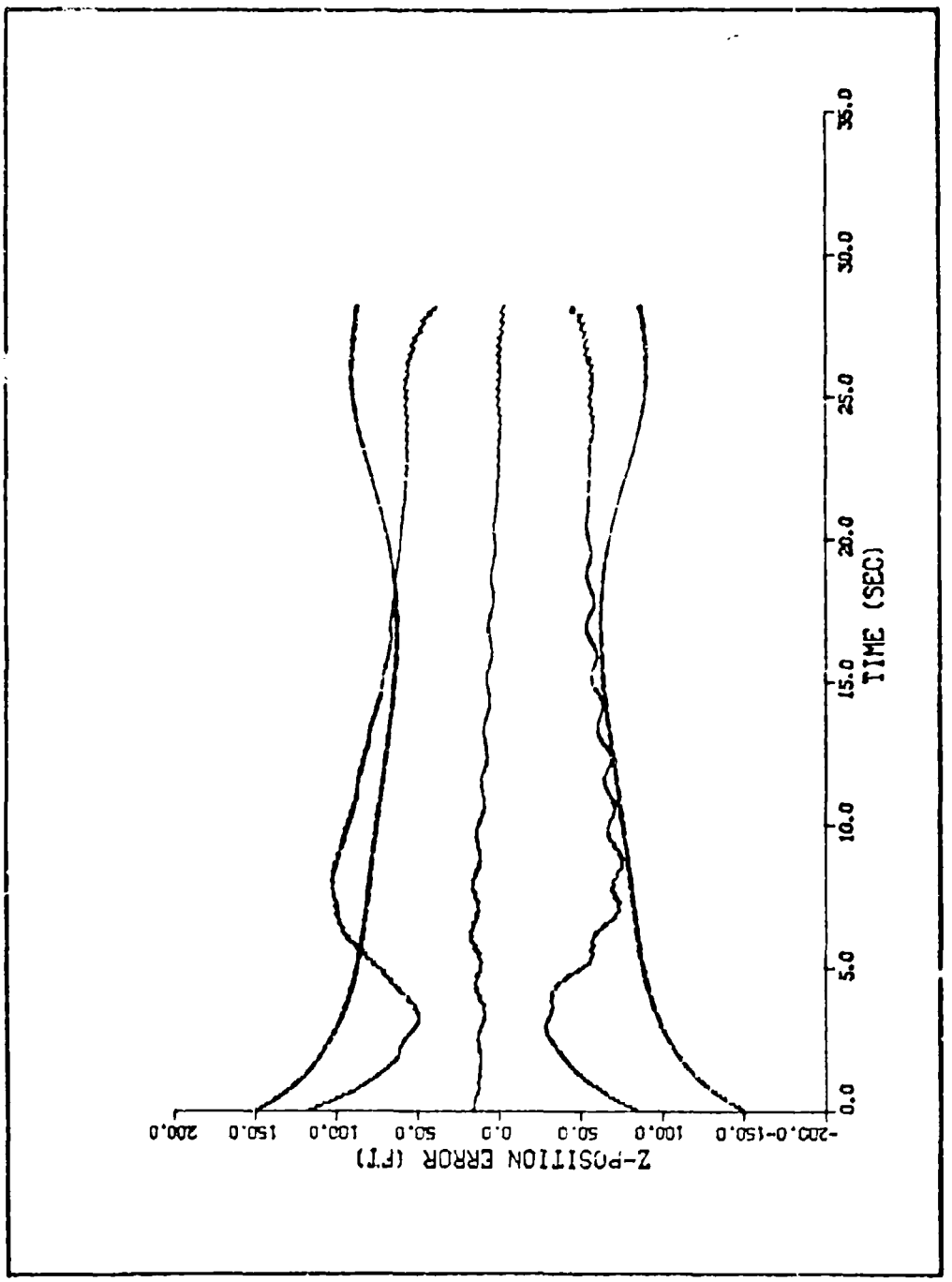

Figure C-13. Strapdown Seeker Only, R_1=.00125 rad^2

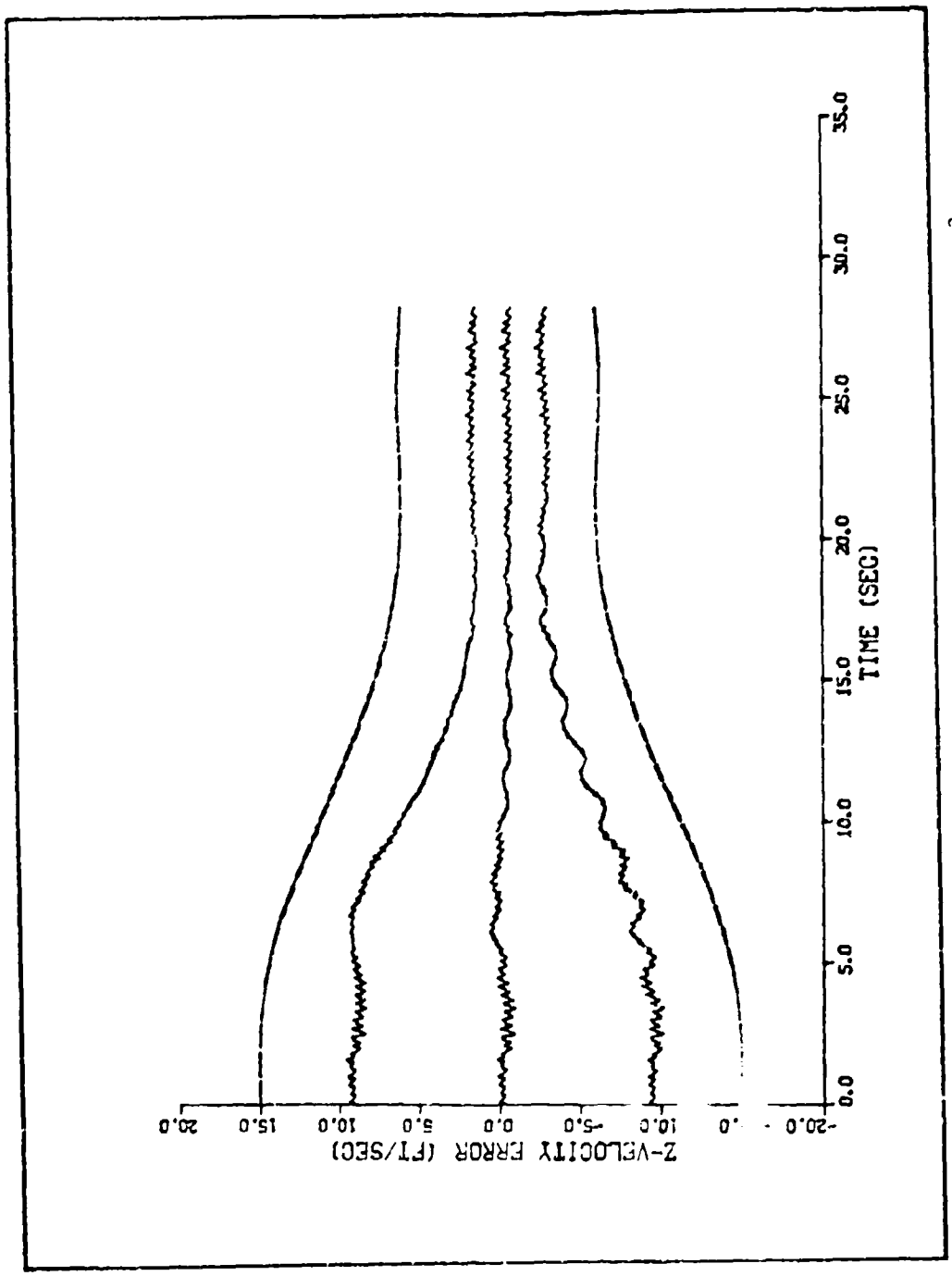

Figure C-14. Strapdown Seeker Only, $R_1 = .00125$ rad^2

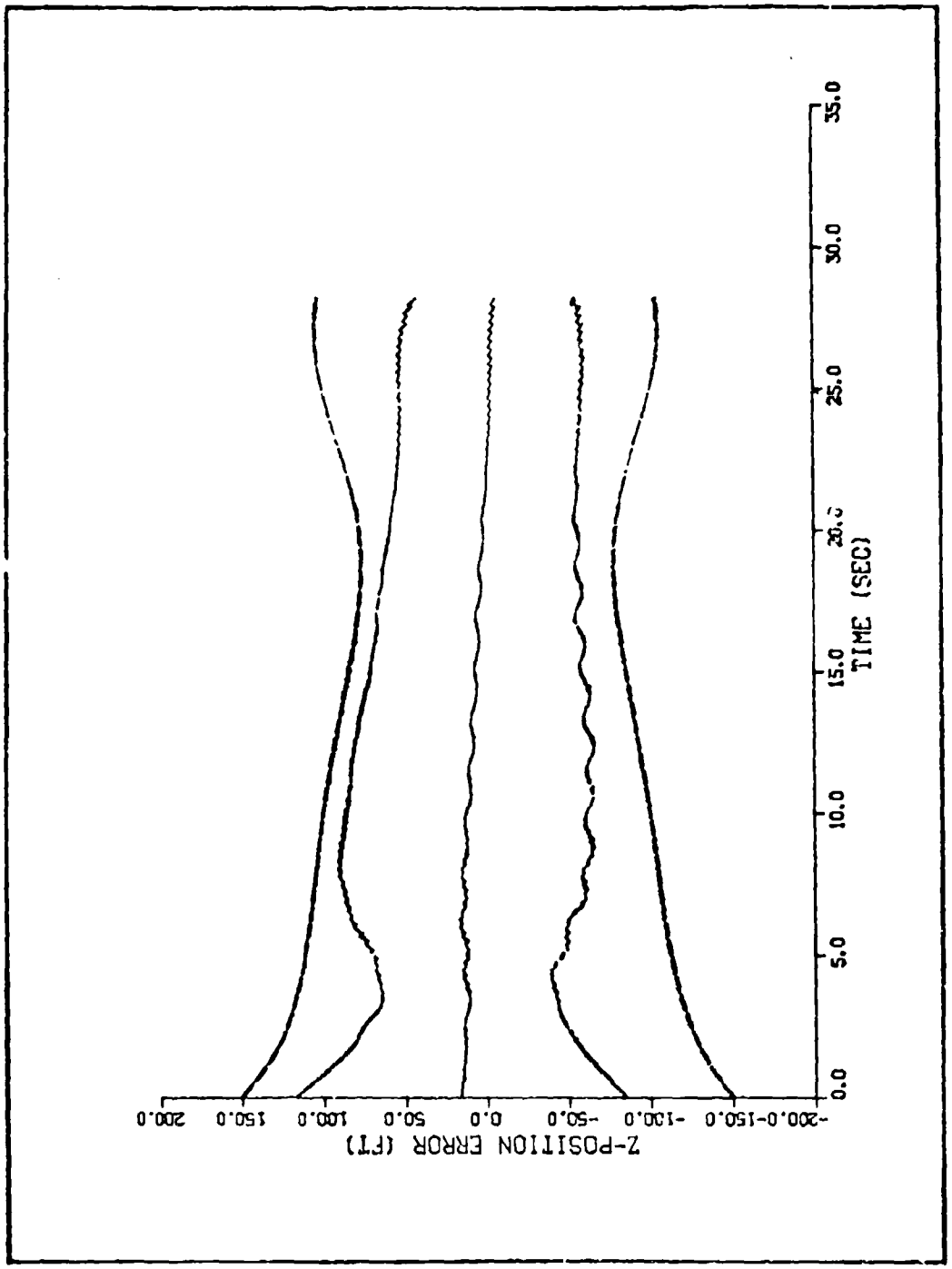

Figure C-15. Strapdown Seeker Only, $R_1 = .0028$ rad^2

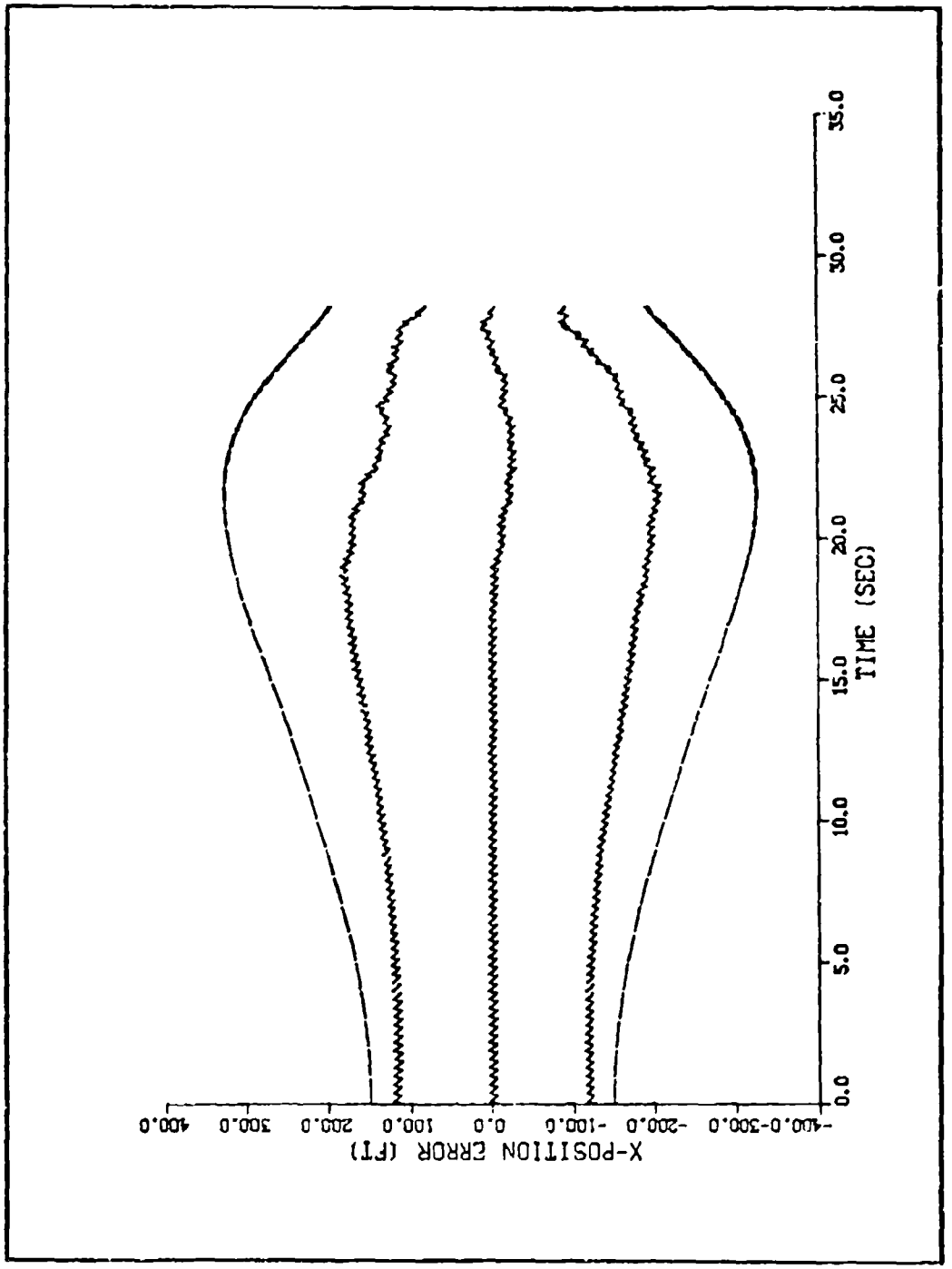

Figure C-16. Gimballed Seeker, Angle Only, R_3=.00125 rad^2

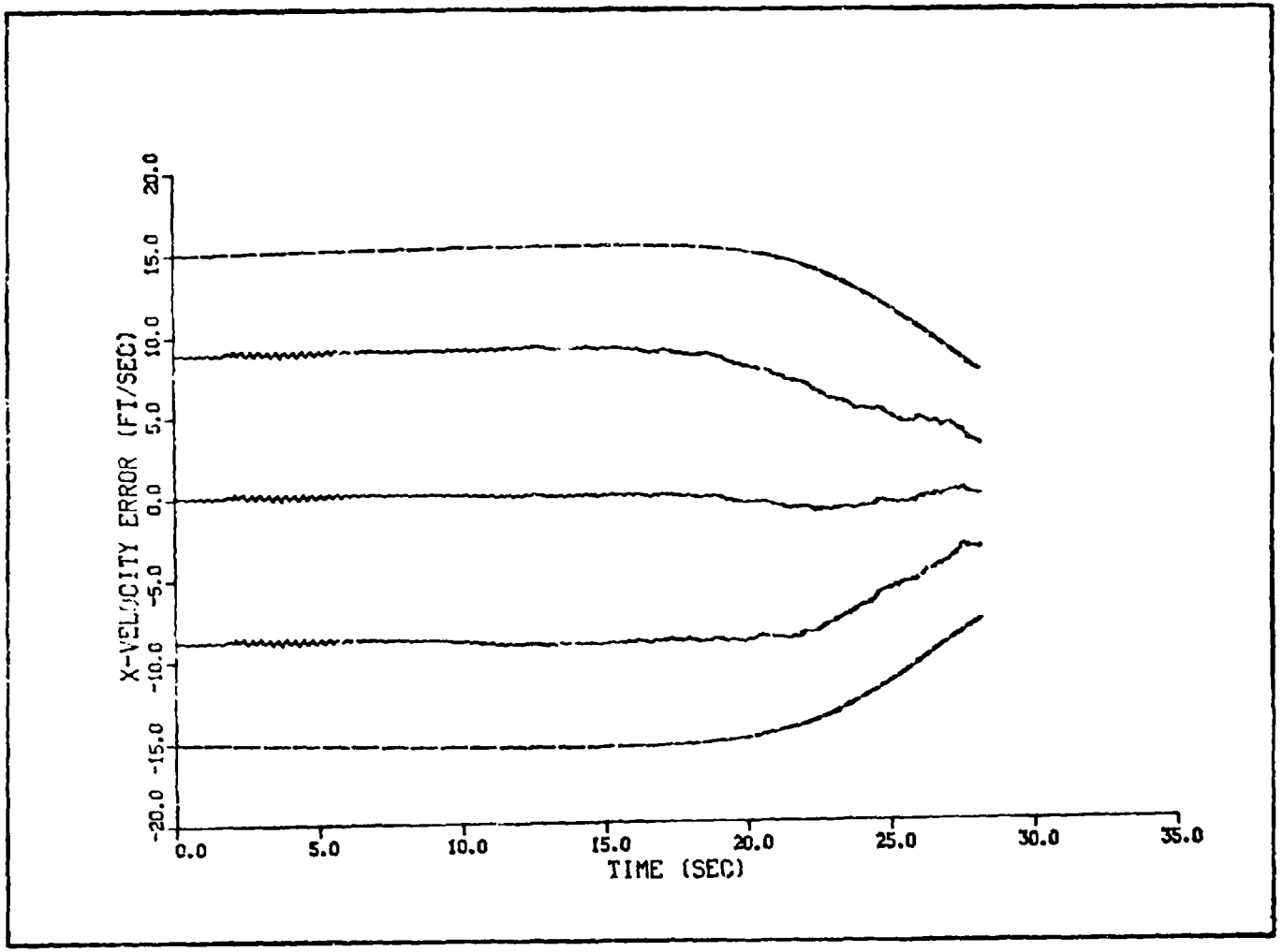

Figure C-17. Gimballed Seeker, Angle Only, R_3=.00125 rad^2

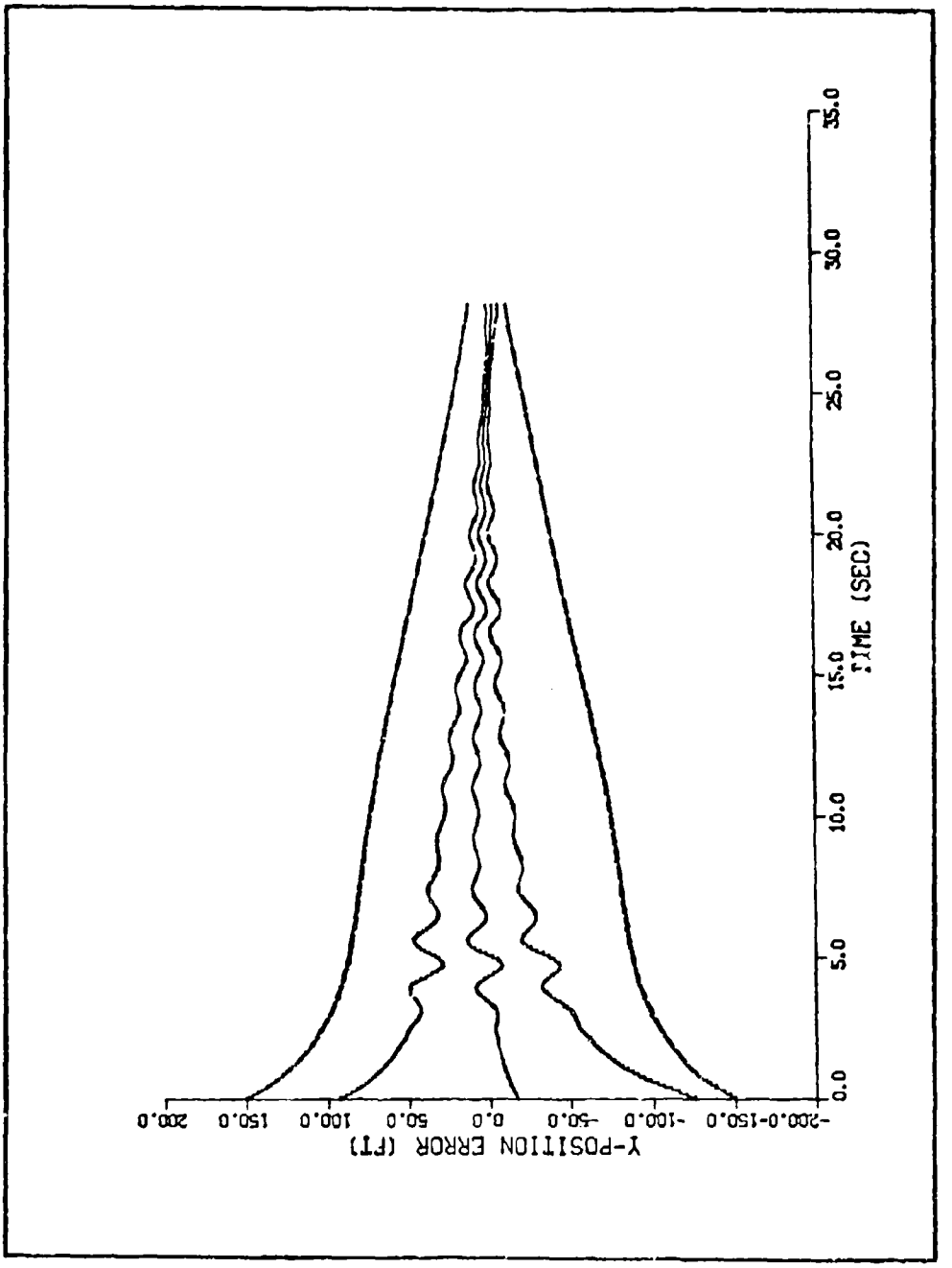

Figure C-18. Gimballed Seeker, Angle Only, $R_3 = .00125$ rad^2

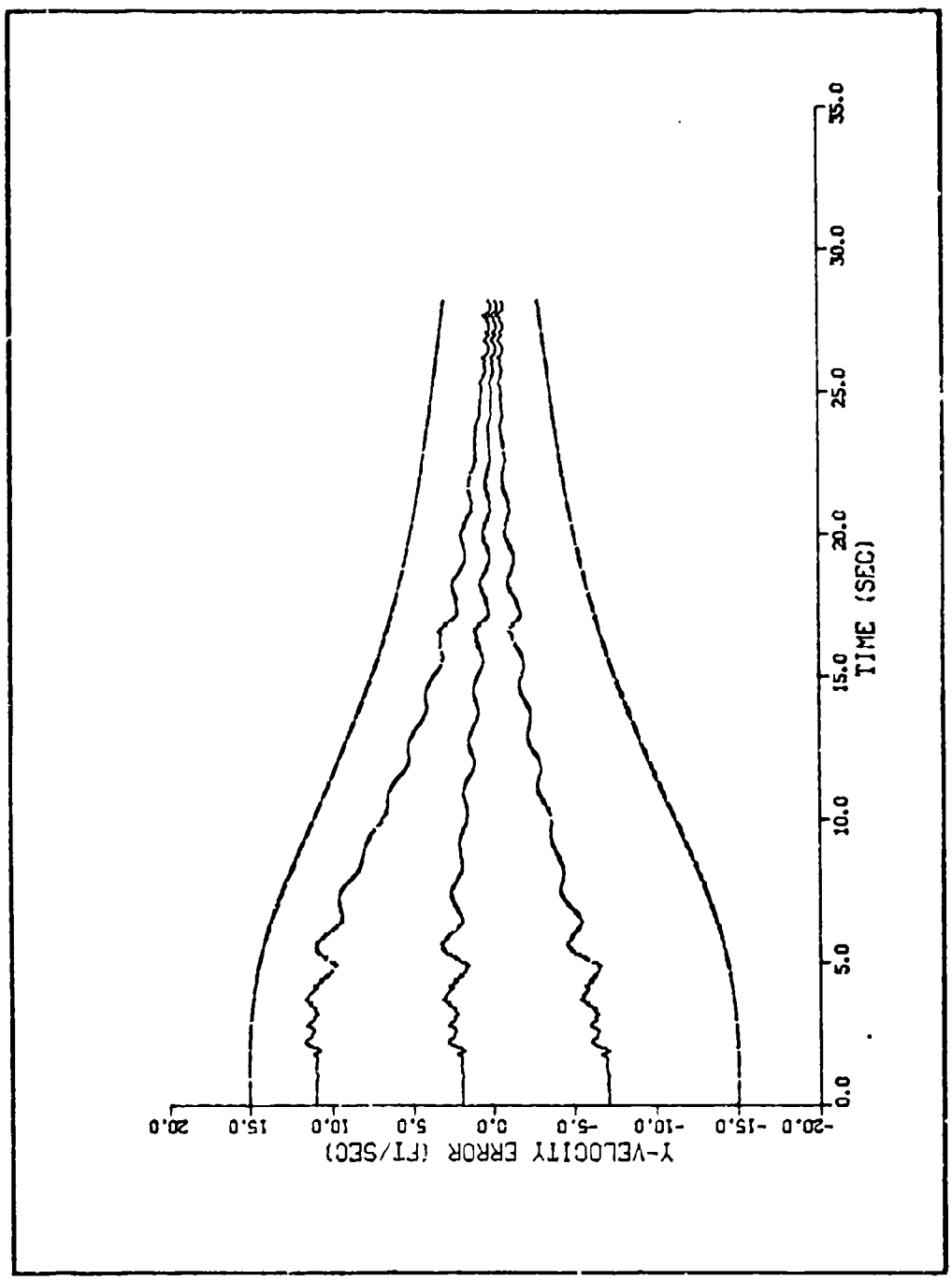

Figure C-19. Gimballed Seeker, Angle Only, R_3=.00125 rad^2

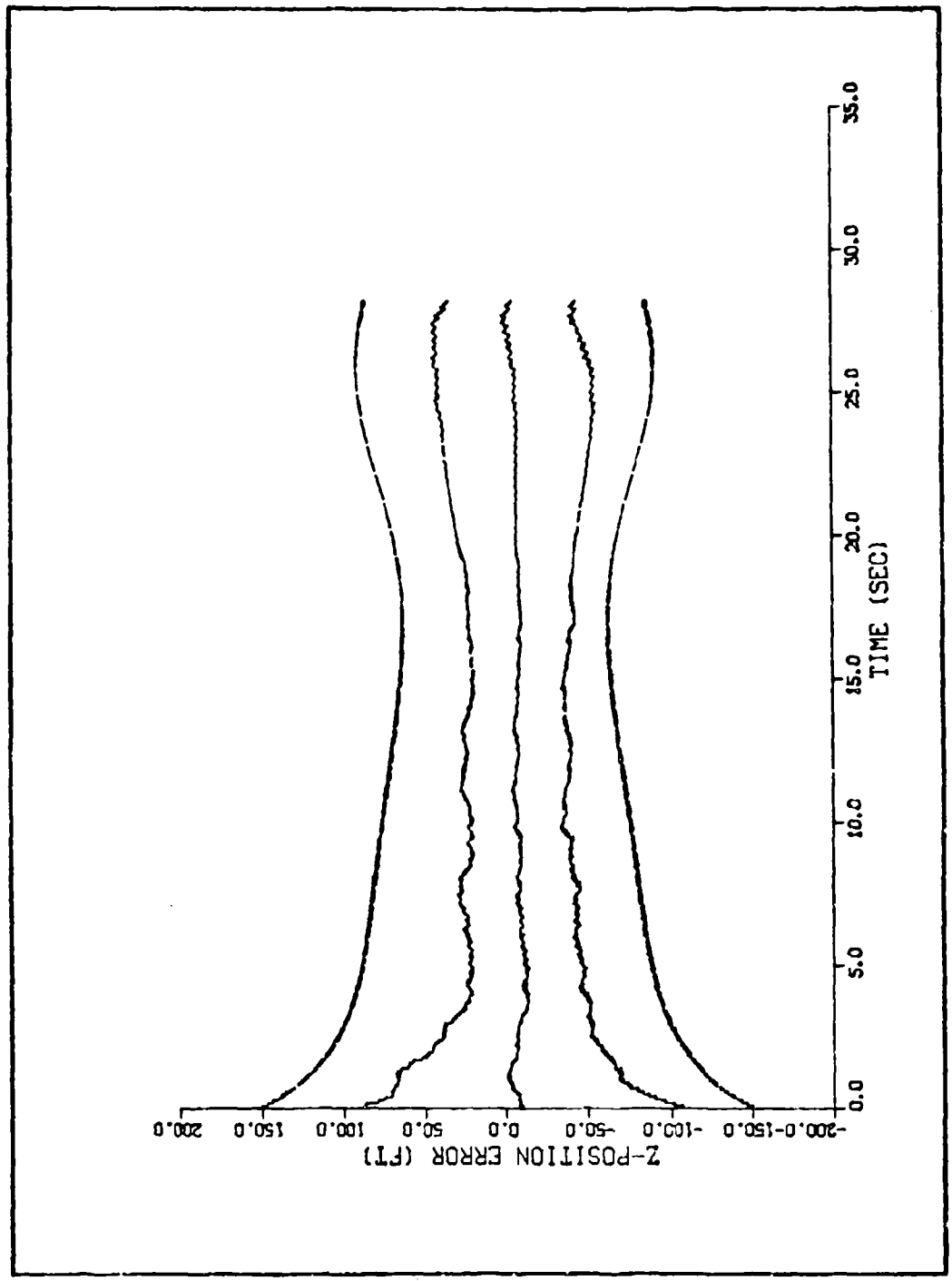

Figure C-20. Gimballed Seeker, Angle Only, $R_3 = .00125$ rad^2

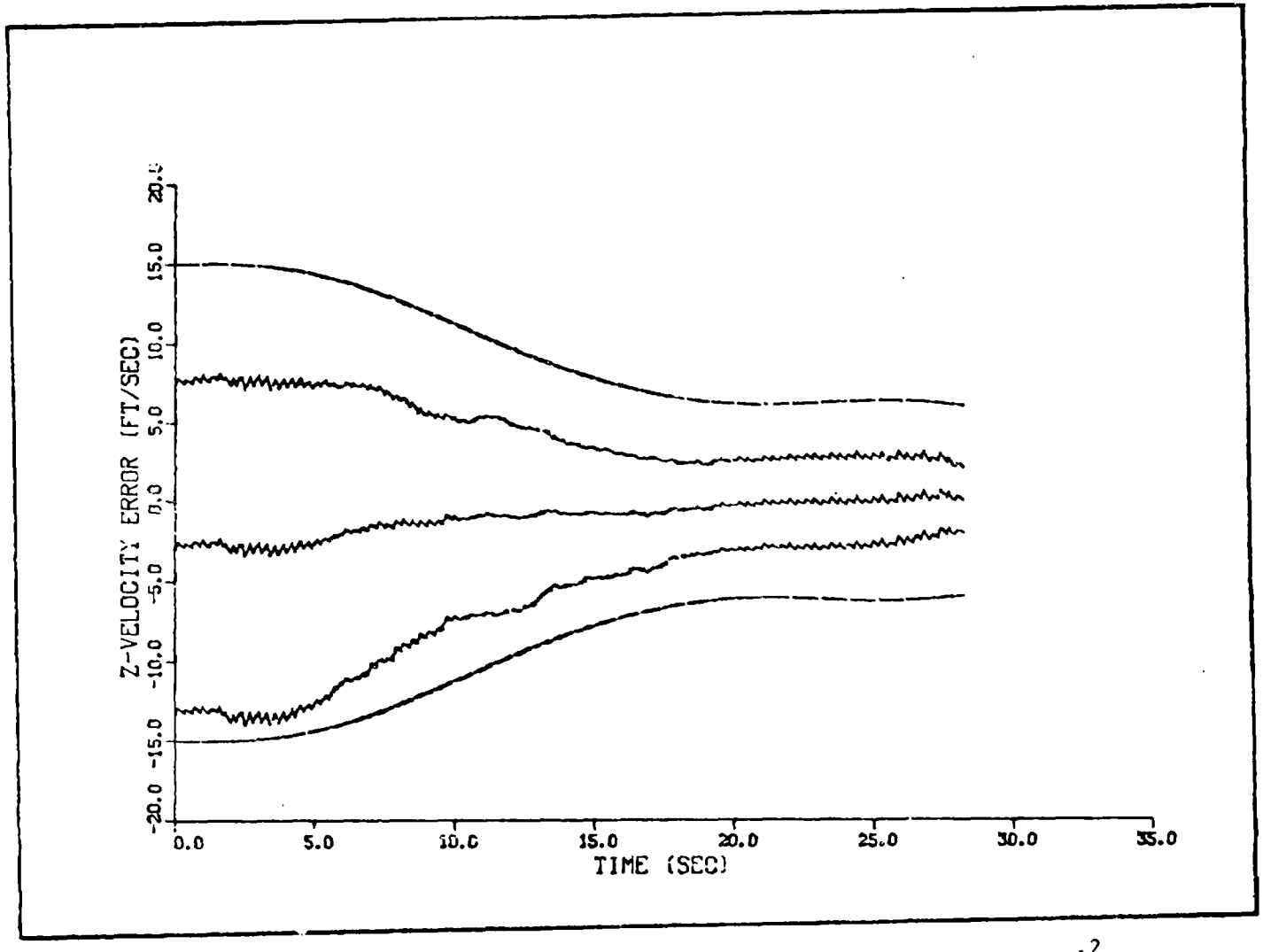

Figure C-21. Gimballed Seeker, Angle Only, R_3=.00125 rad^2

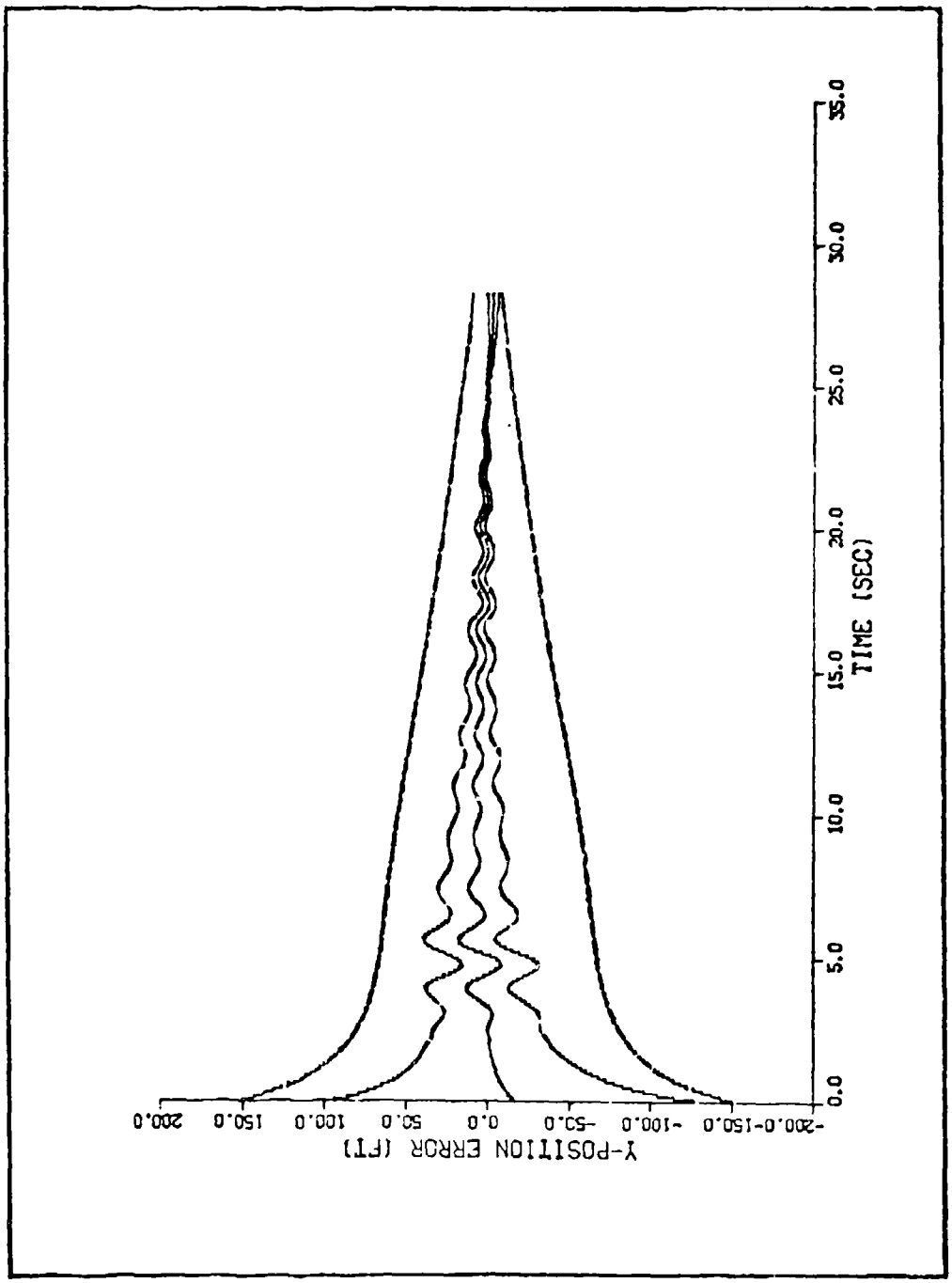

Figure C-22. Gimballed Seeker, Angle Only, $R_3 = .000556$ rad^2

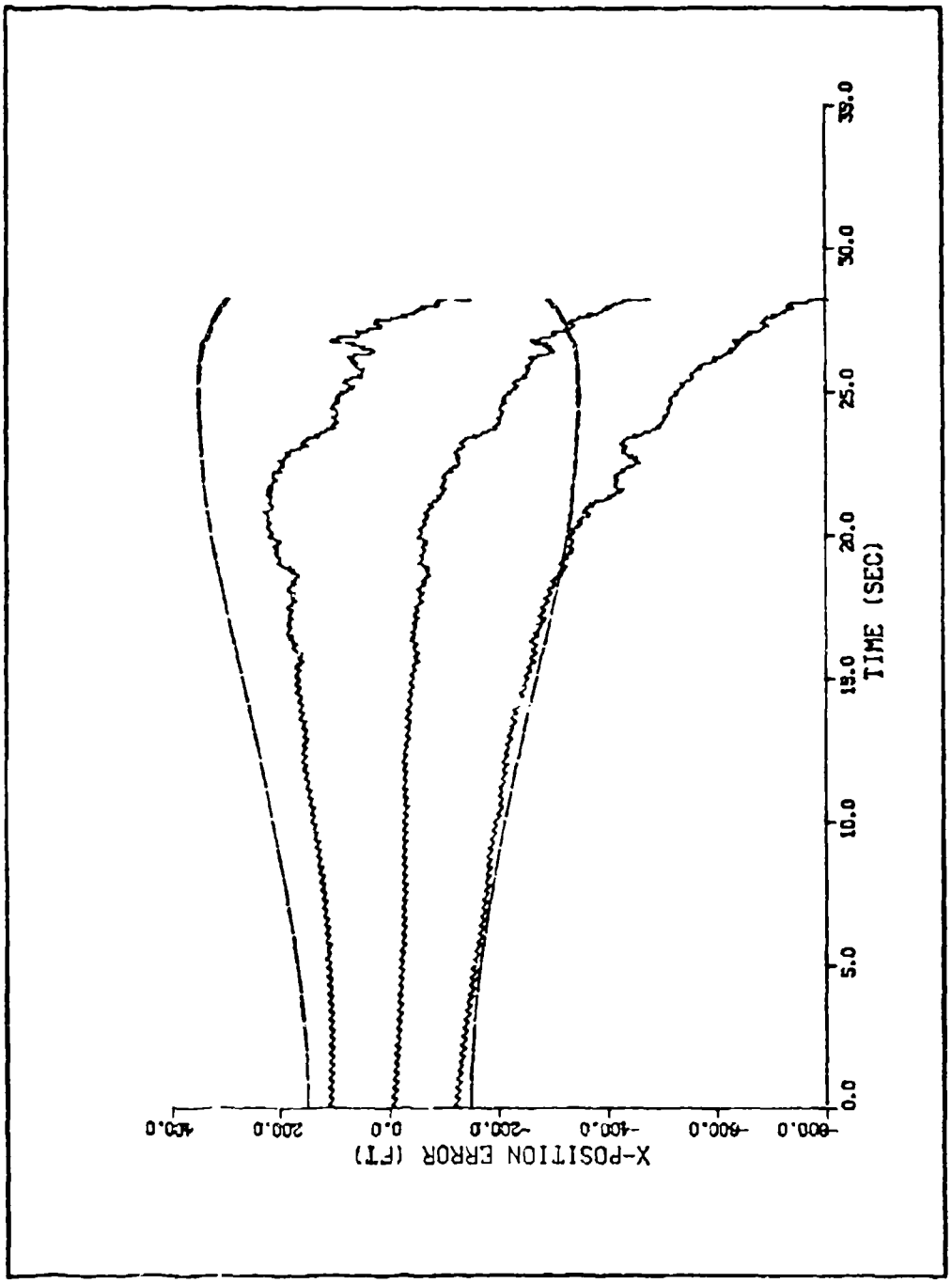

Figure C-23. Gimballed Seeker, Angle-Rate Only, R_ζ=.00125 rad^2

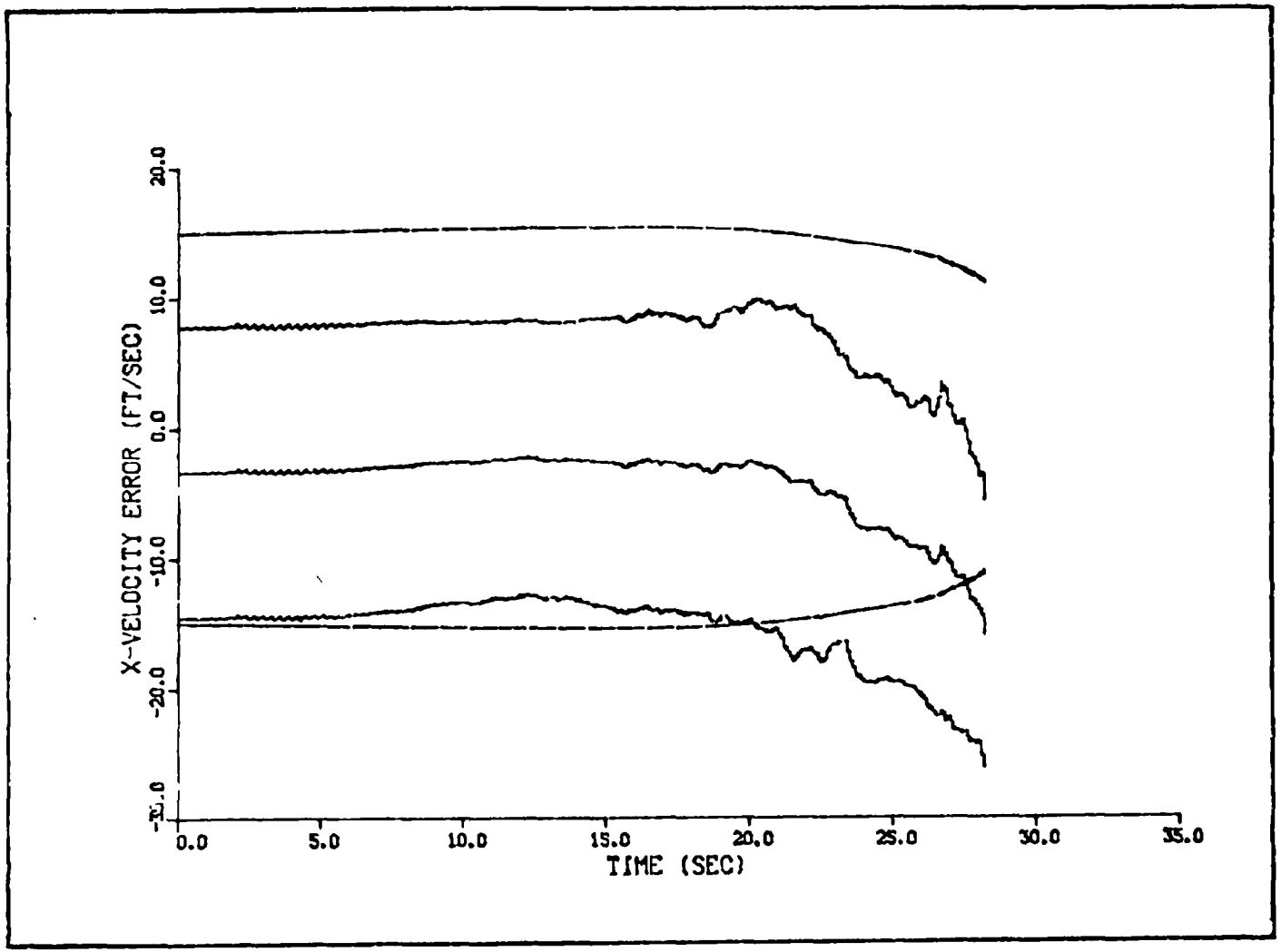

Figure C-24. Gimballed Seeker, Angle-Rate Only, R_5=.00125 rad^2

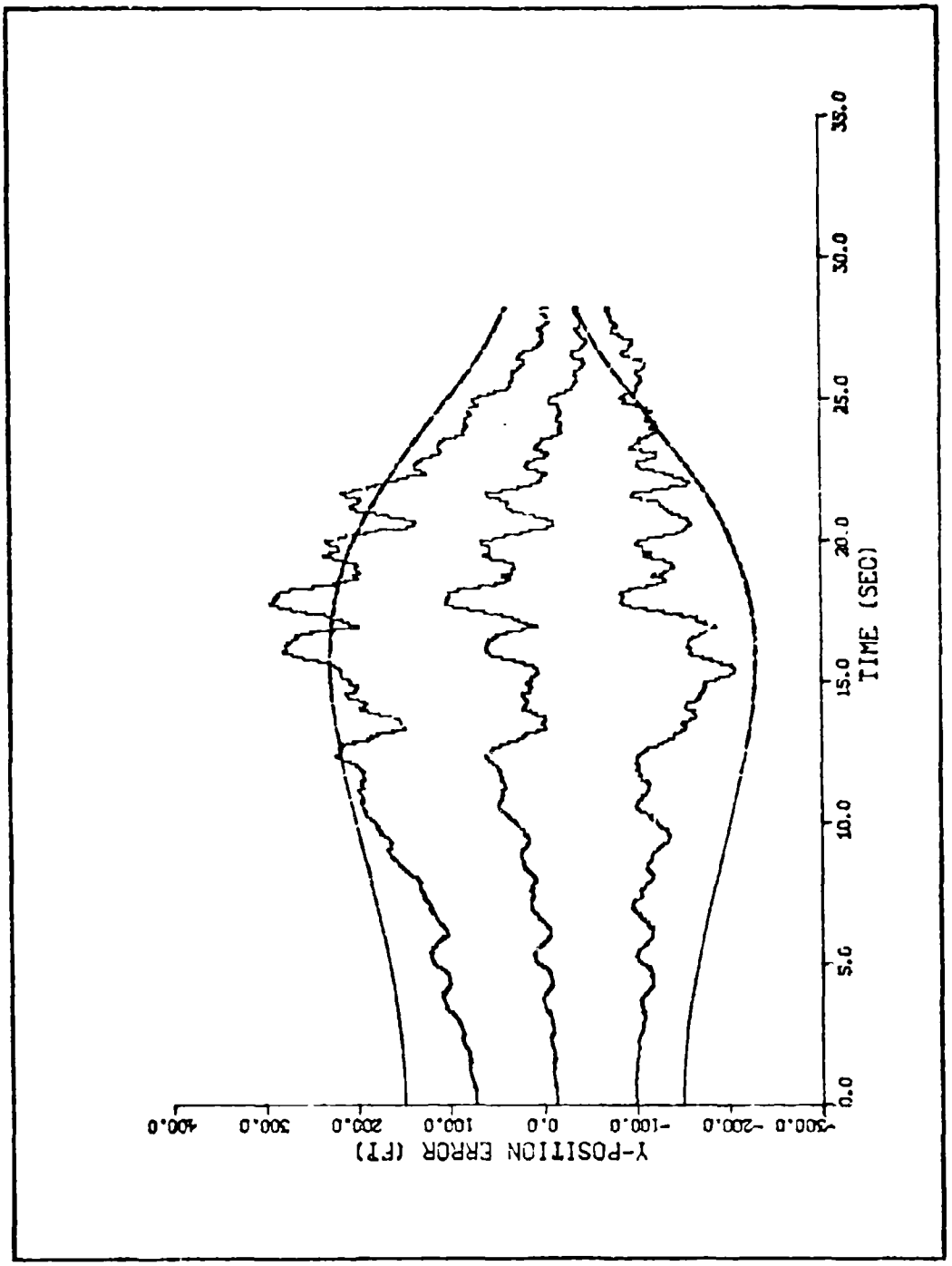

Figure C-25. Gimballed Seeker, Angle-Rate Only, R_5=.00125 rad^2

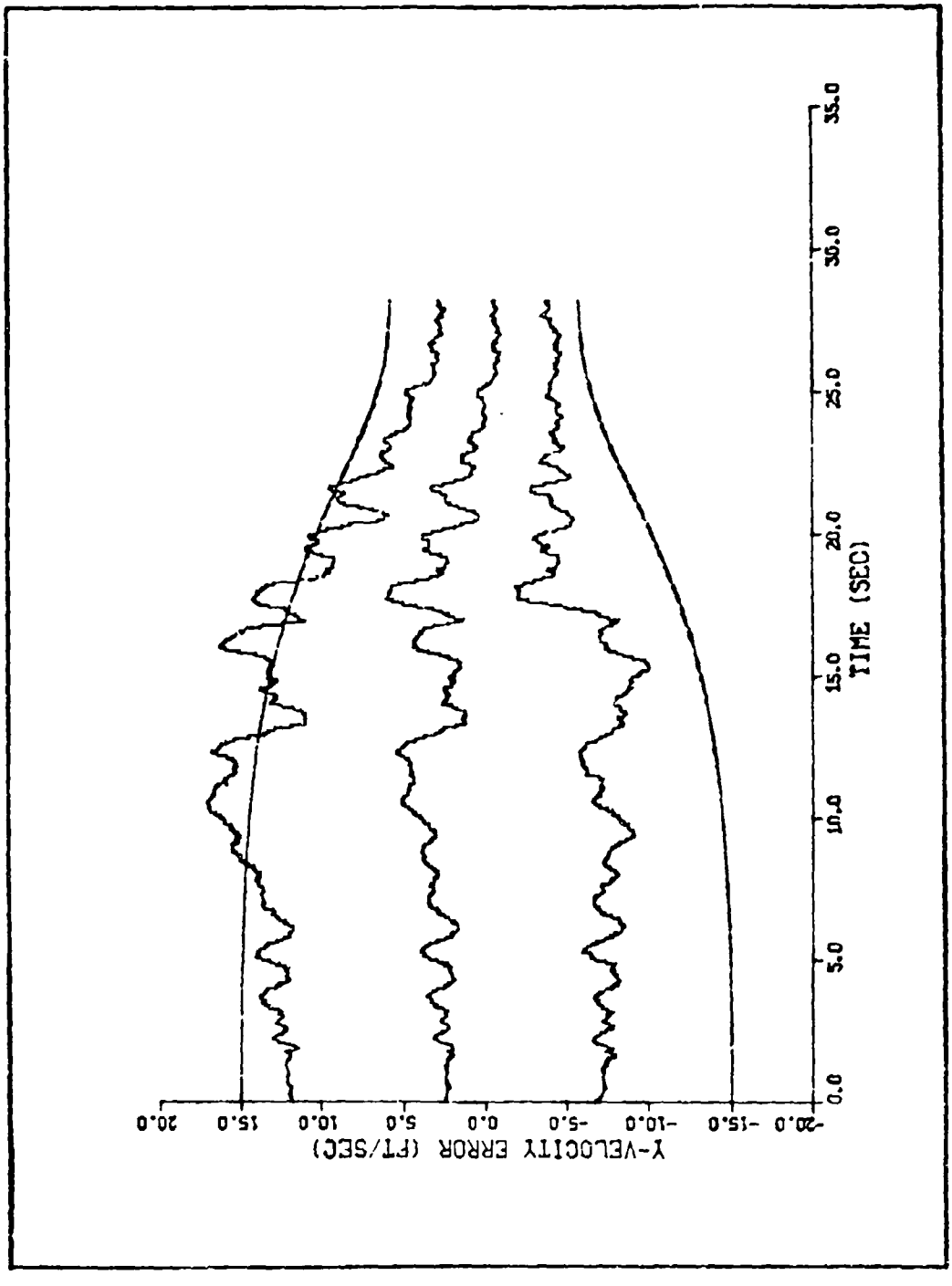

Figure C-26. Gimballed Seeker, Angle-Rate Only, R_S=.00125 rad^2

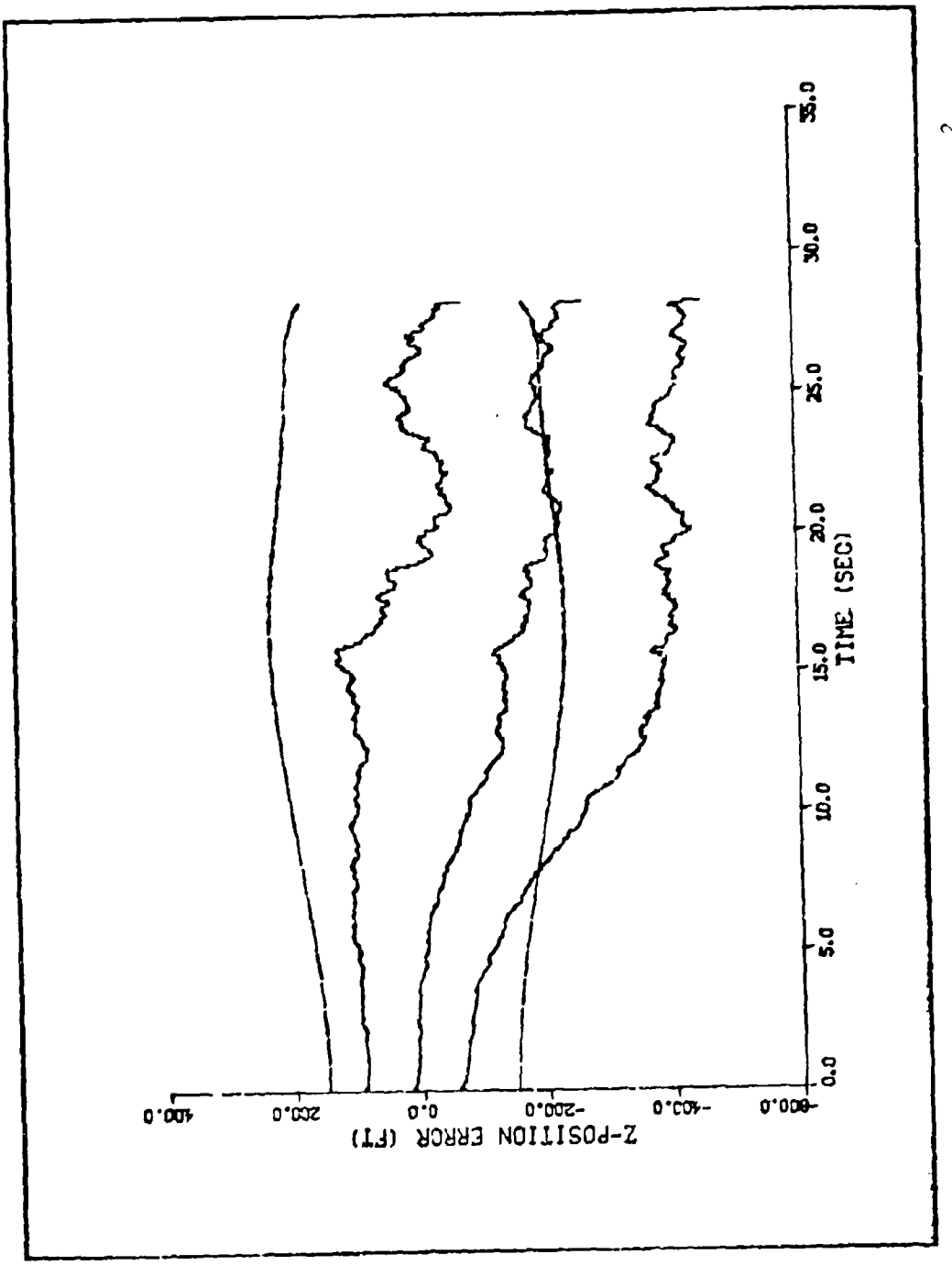

Figure C-27. Gimballed Seeker, Angle-Rate Only, $R_S = .00125$ rad^2

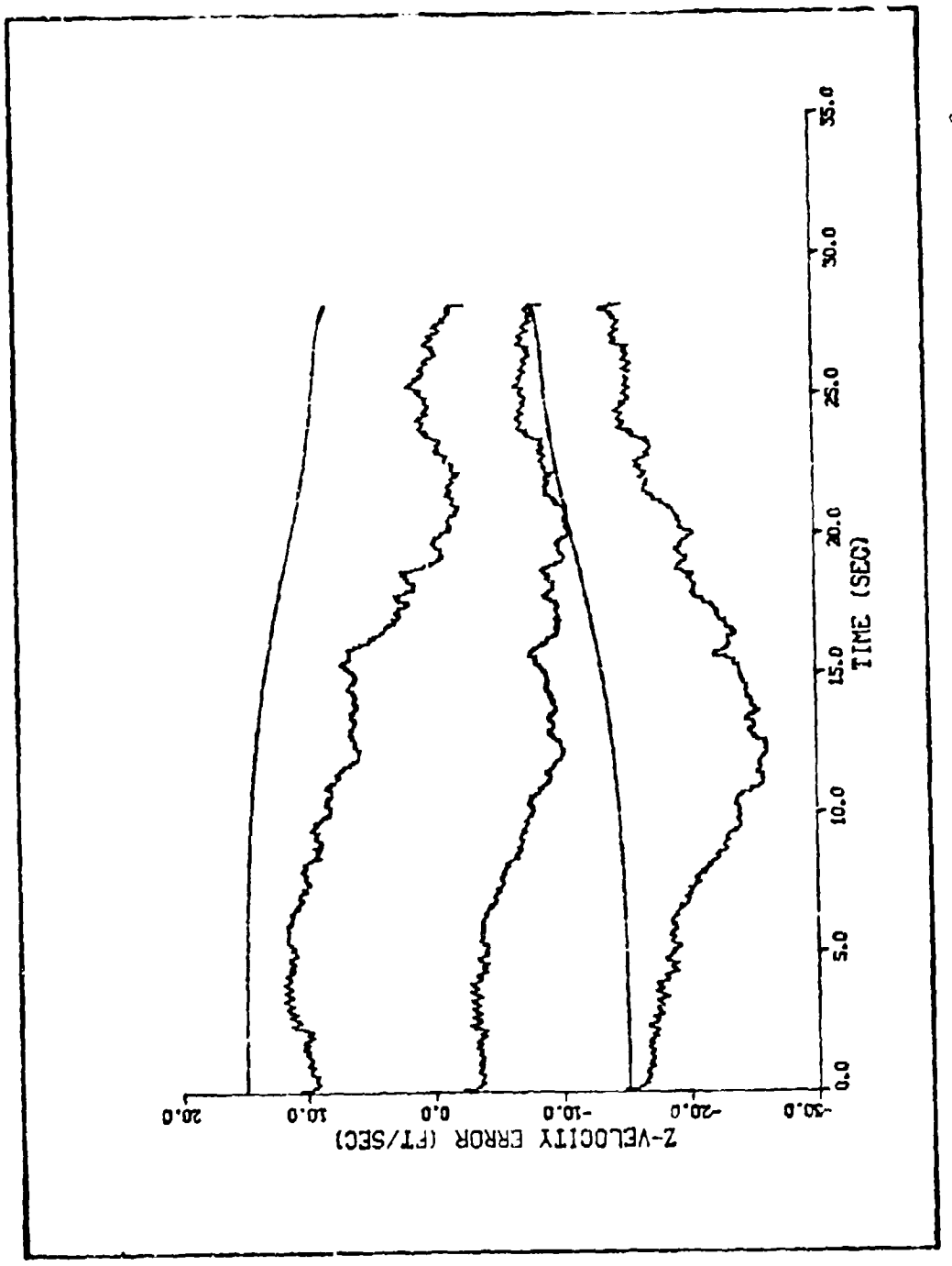

Figure C-28. Gimballed Seeker, Angle-Rate Only, R_S=.00125 rad^2

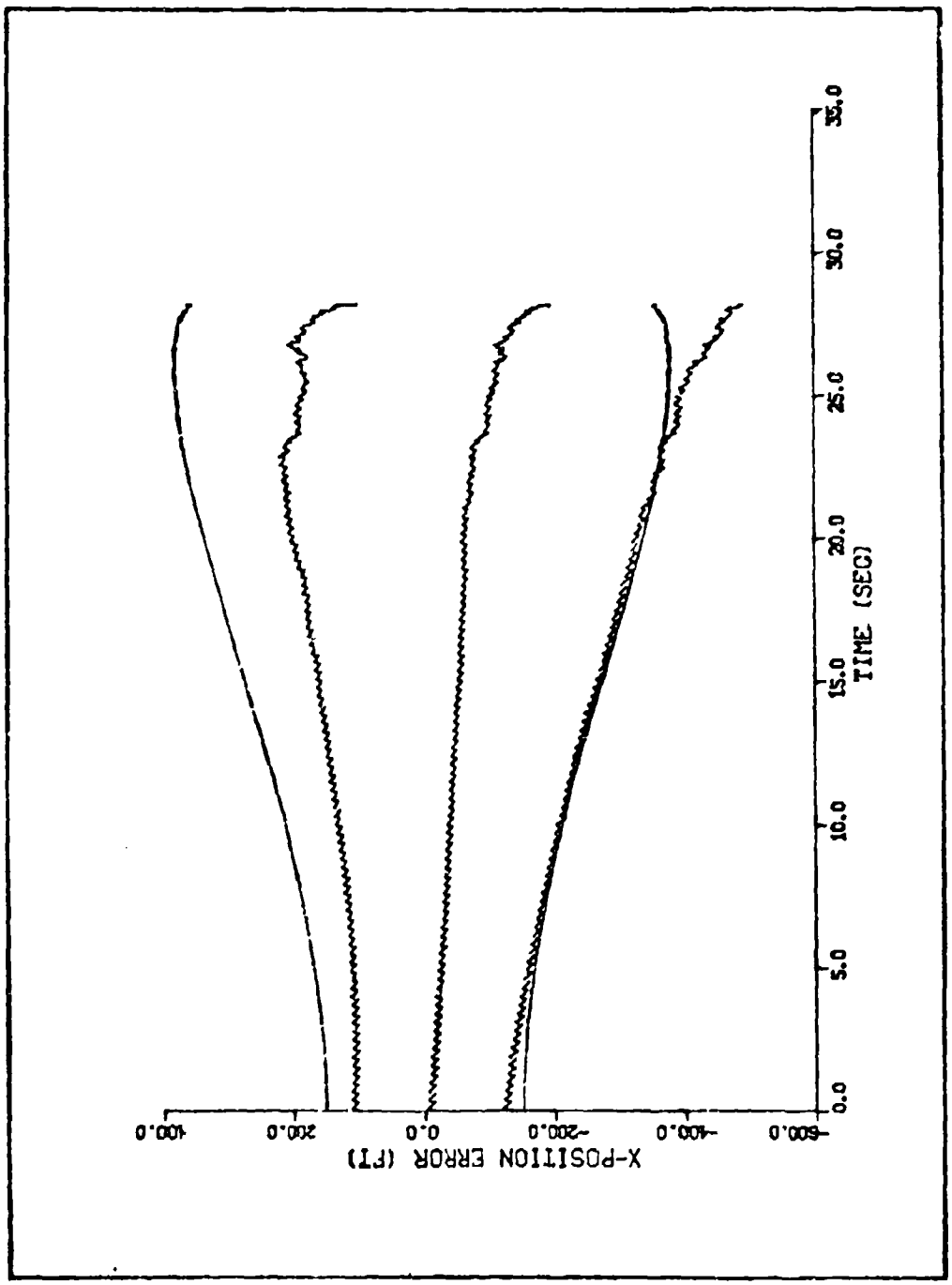

Figure C-29. Gimballed Seeker, Angle-Rate Only, R_5=.0078 rad^2

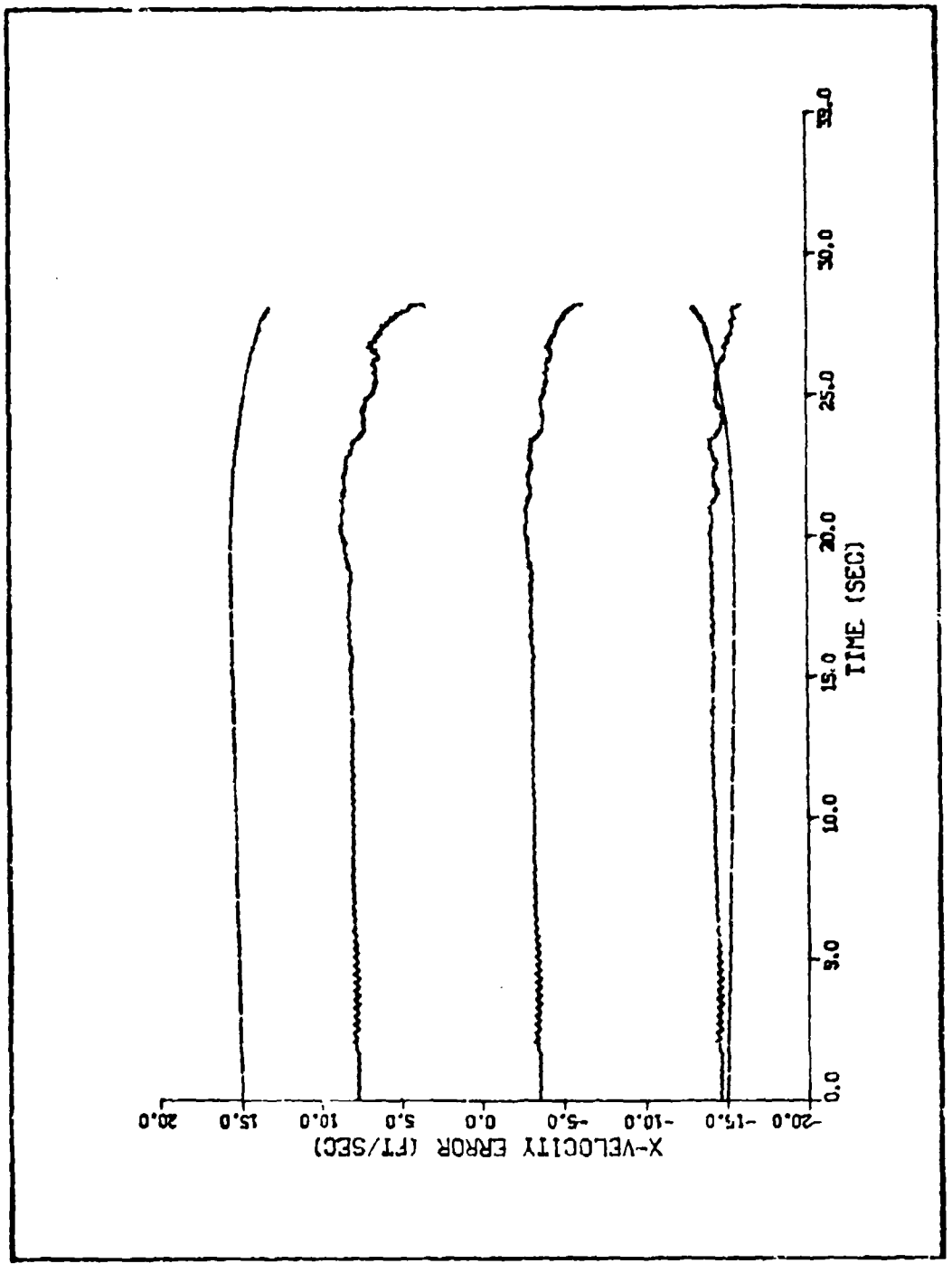

Figure C-30. Gimballed Seeker, Angle-Rate Only, R_5=.0078 rad^2

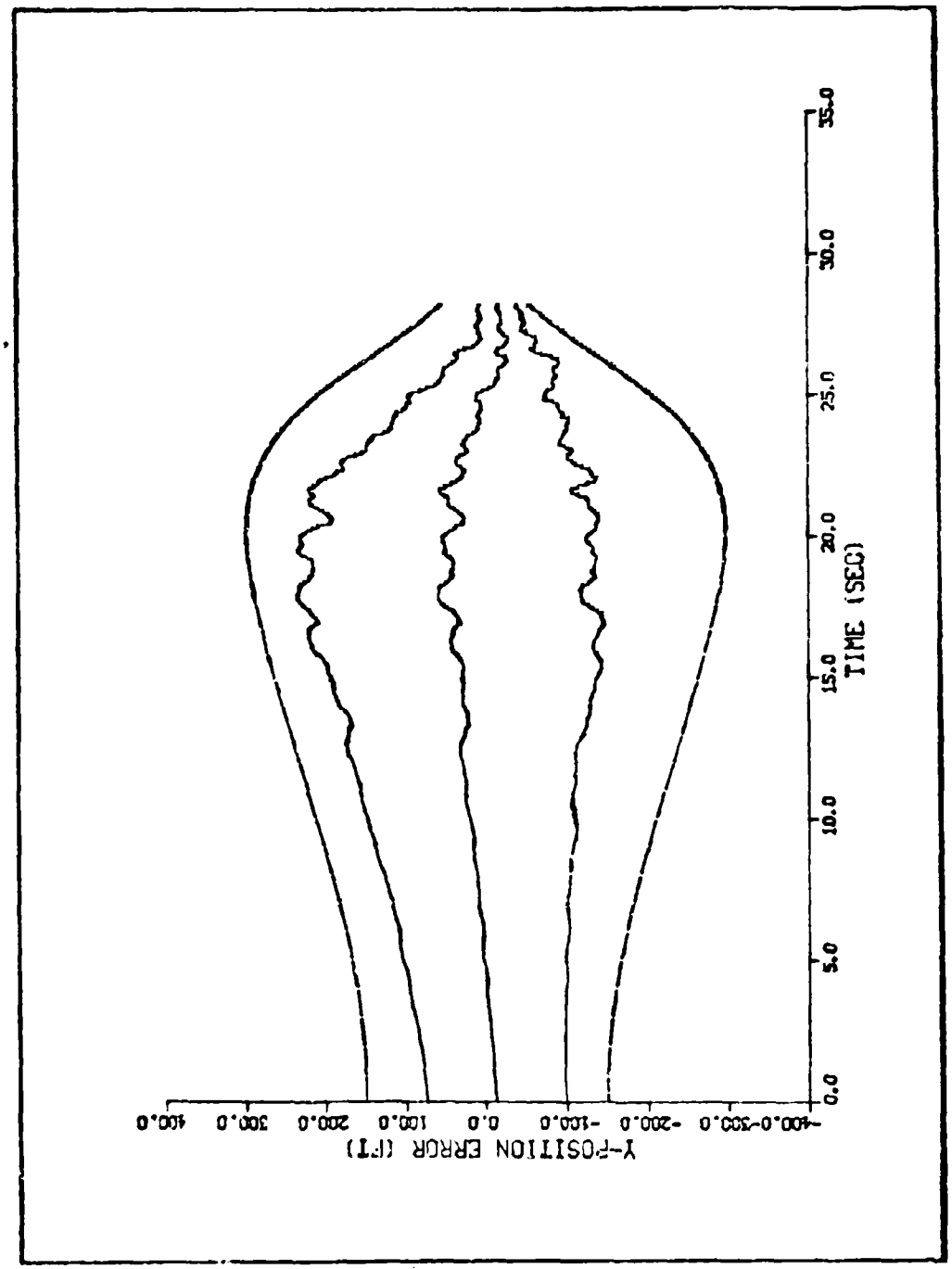

Figure C-31. Gimballed Seeker, Angle-Rate Only, P_5=.0078 rad^2

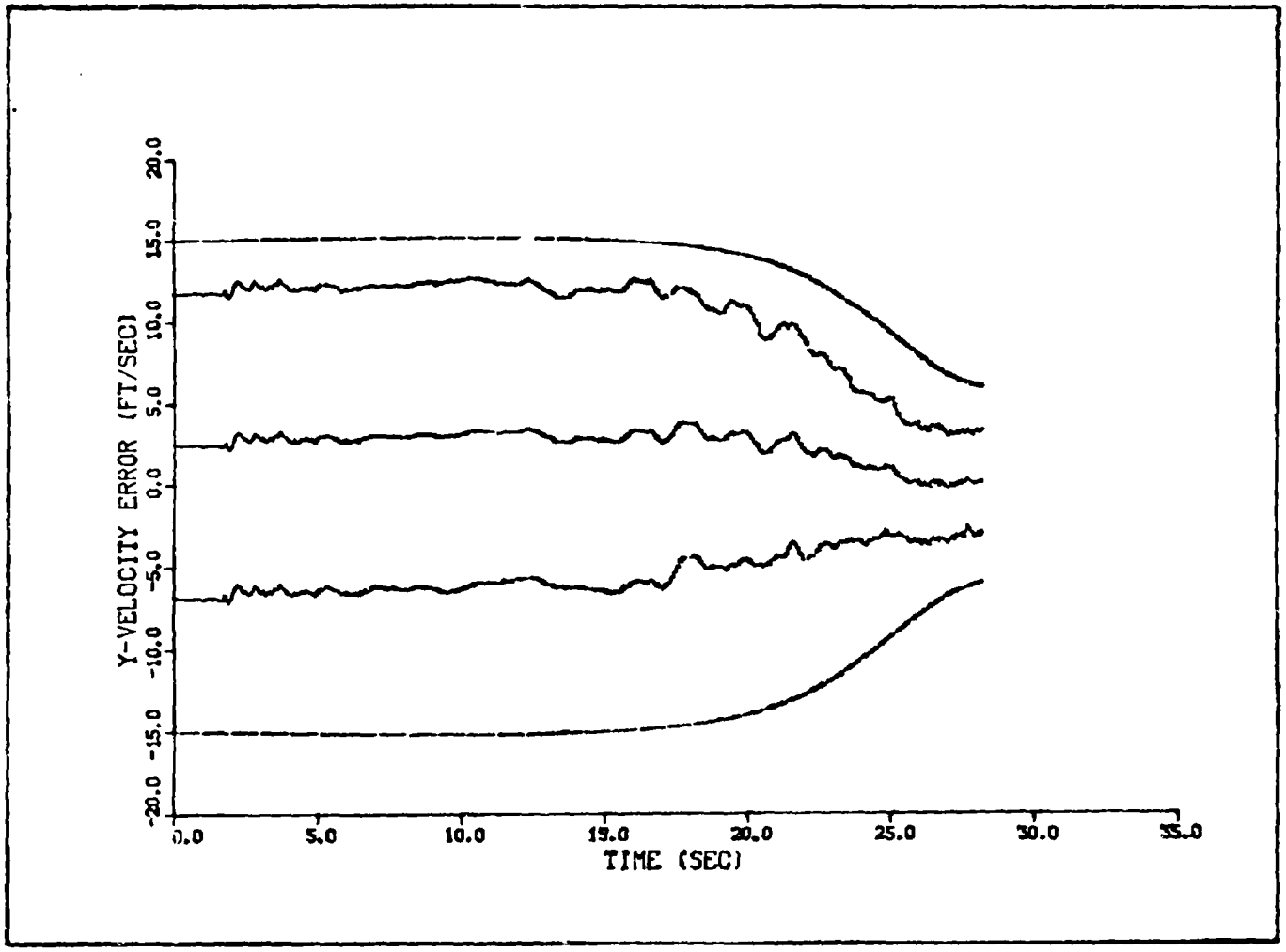

Figure C-32. Gimballed Seeker, Angle-Rate Only, R_S=.0078 rad^2

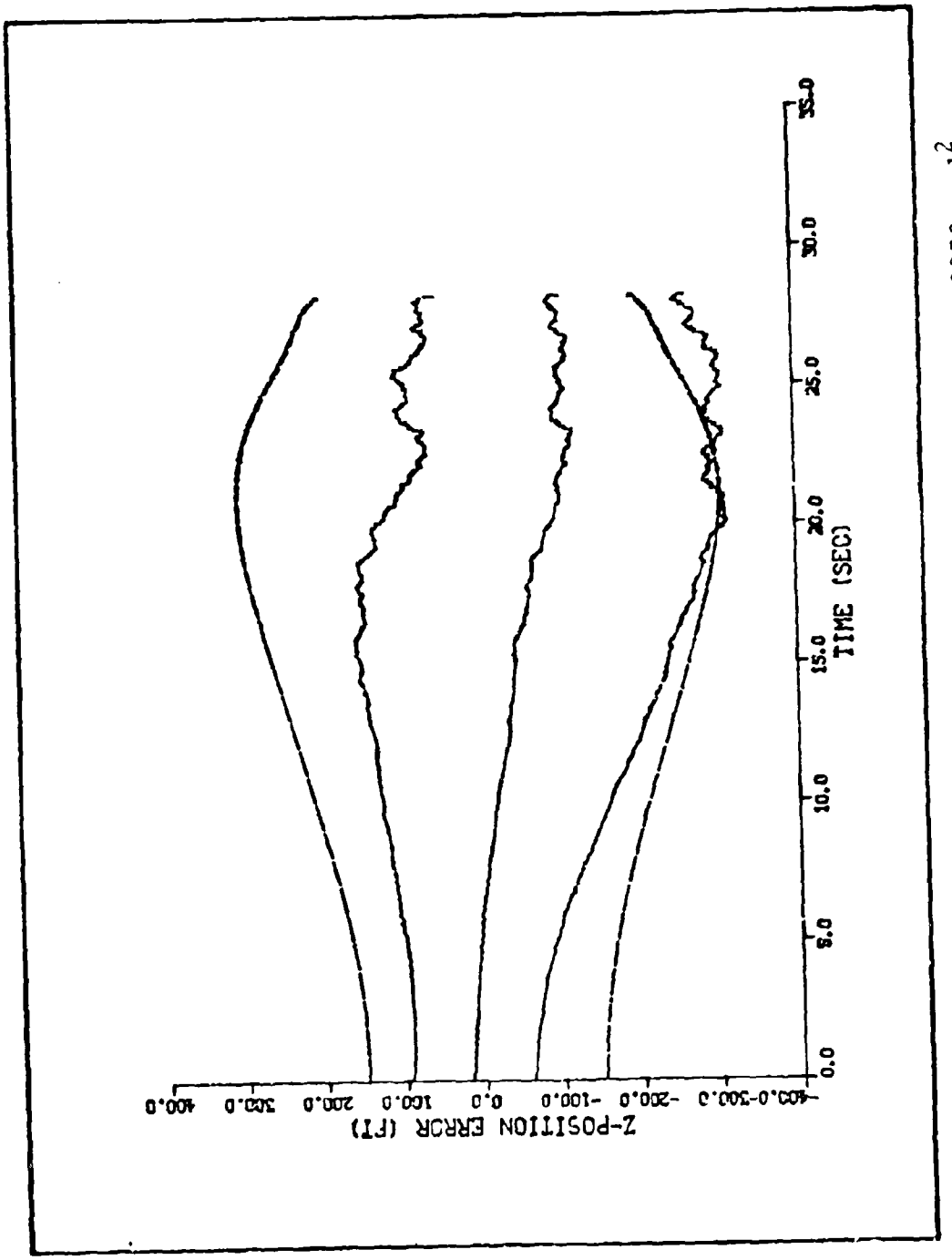

Figure C-33. Gimballed Seeker, Angle-Rate Only, R_5=.0078 rad^2

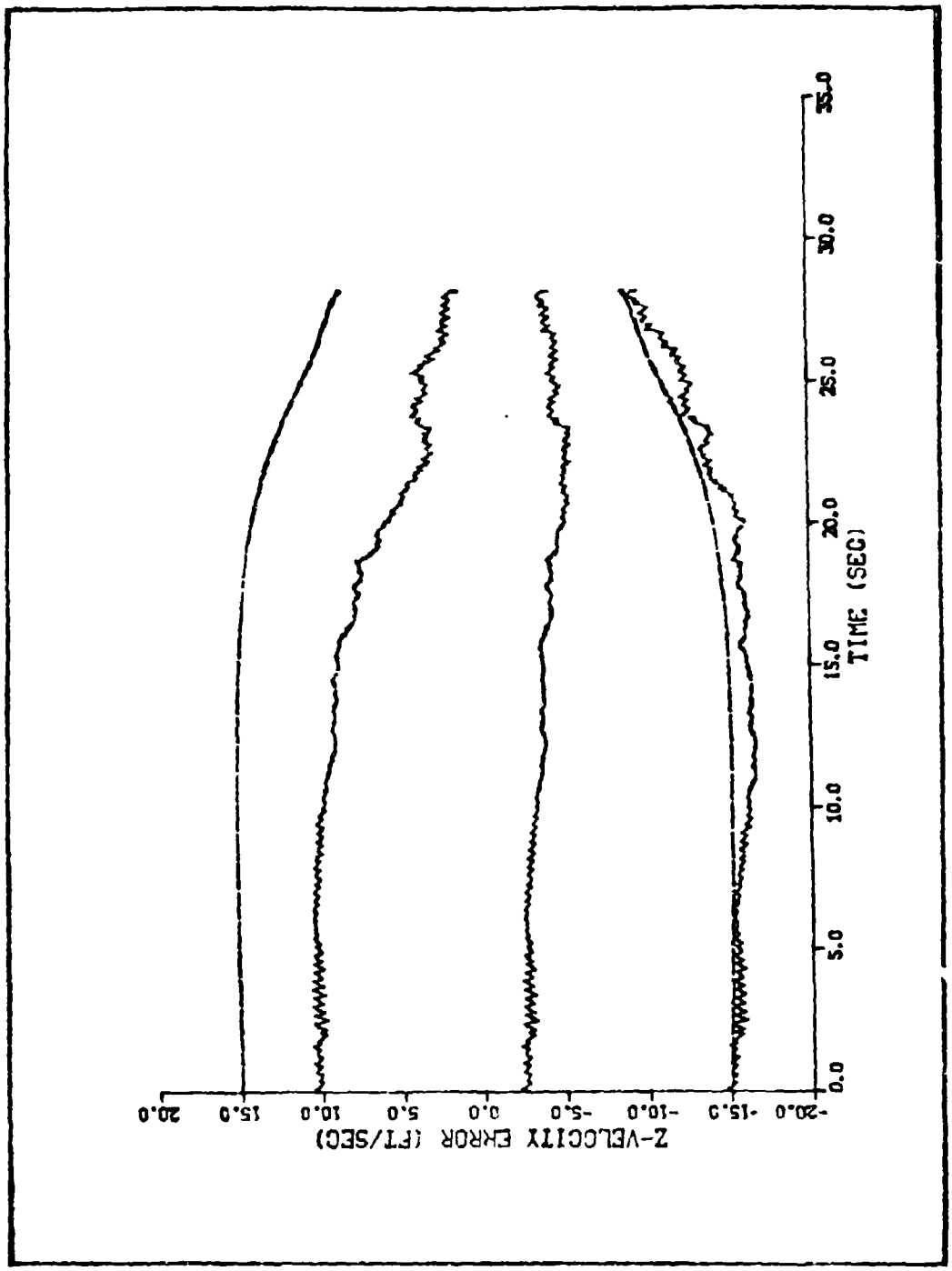

Figure C-34. Gimballed Seeker, Angle-Rate Only, R_5=.0078 rad^2

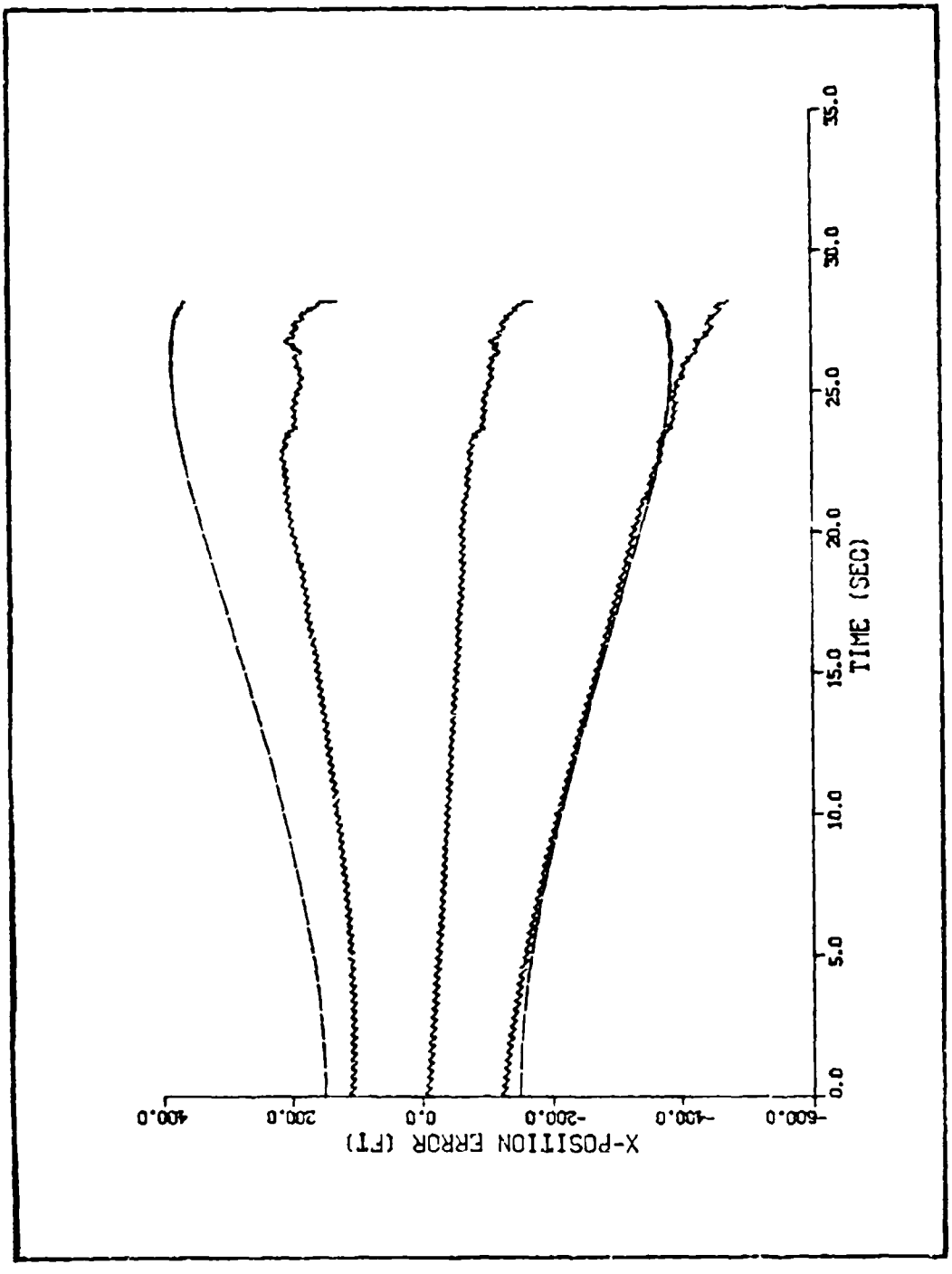

Figure C-35. Gimballed Seeker, Angle-Rate Only, R_S=.01125 rad^2

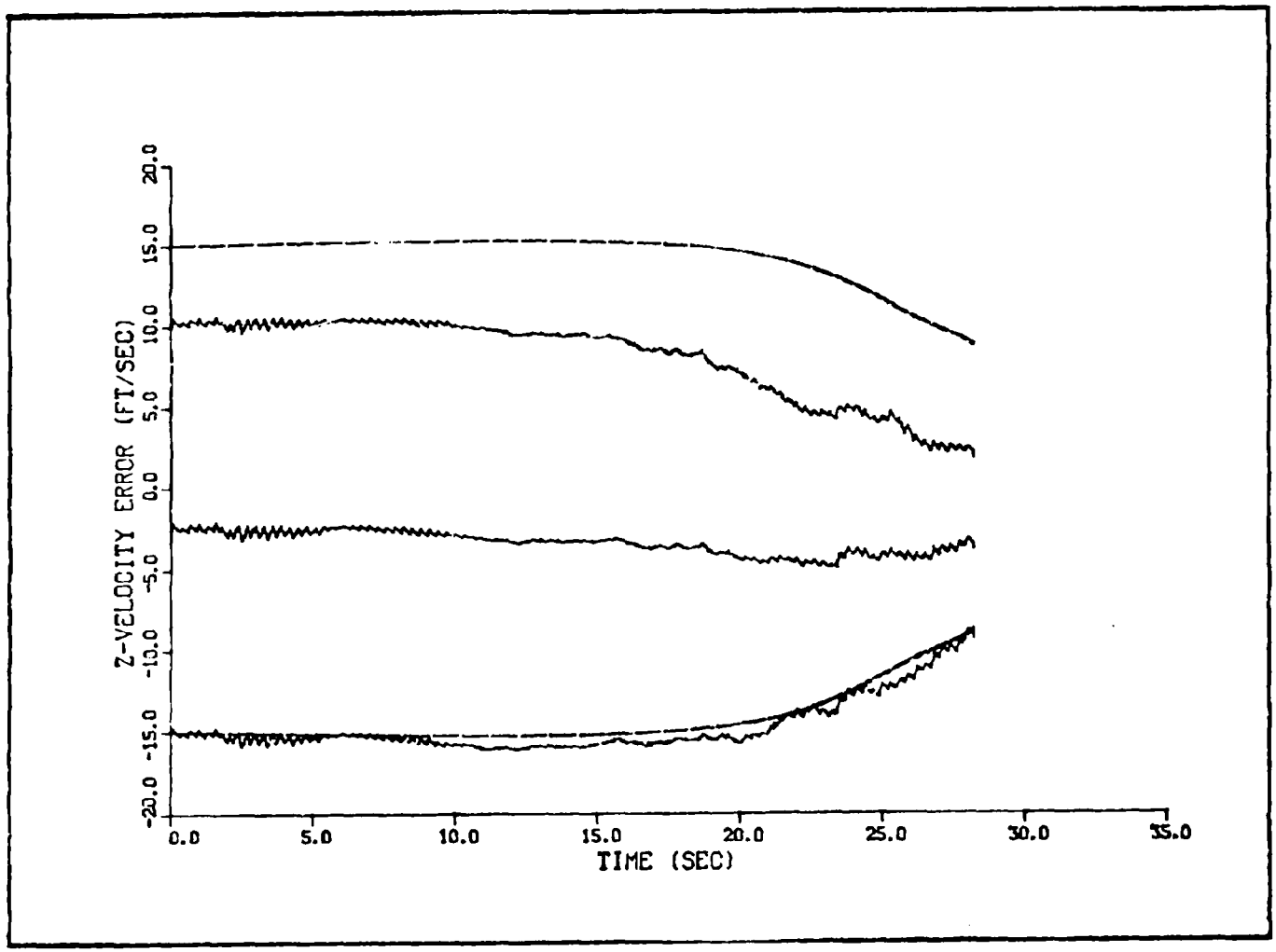

Figure C-36. Gimballed Seeker, Angle-Rate Only, R_5=.01125 rad^2

APPENDIX D

Plots for the Results

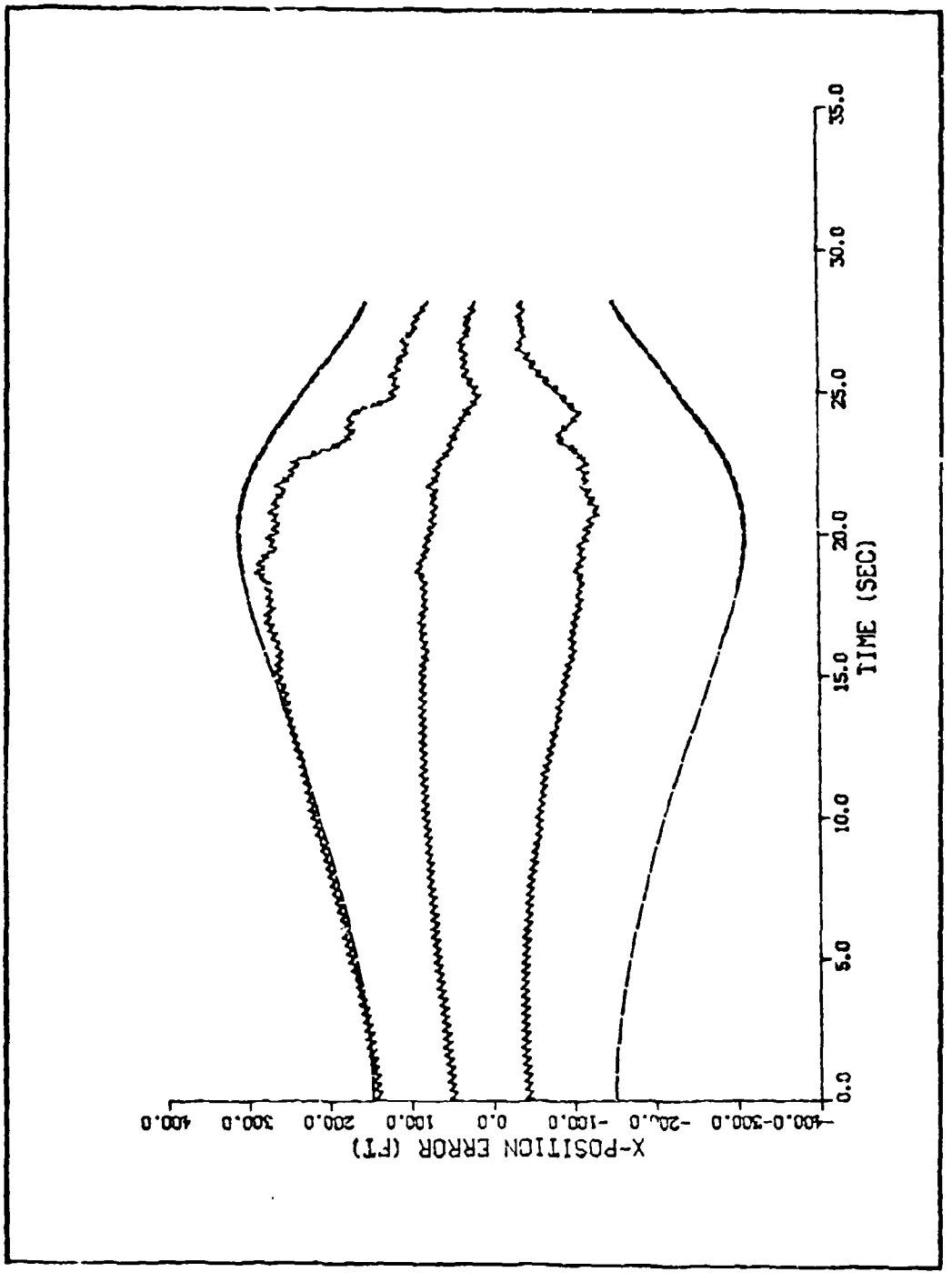

Figure D-1. Both Seekers Throughout Flight

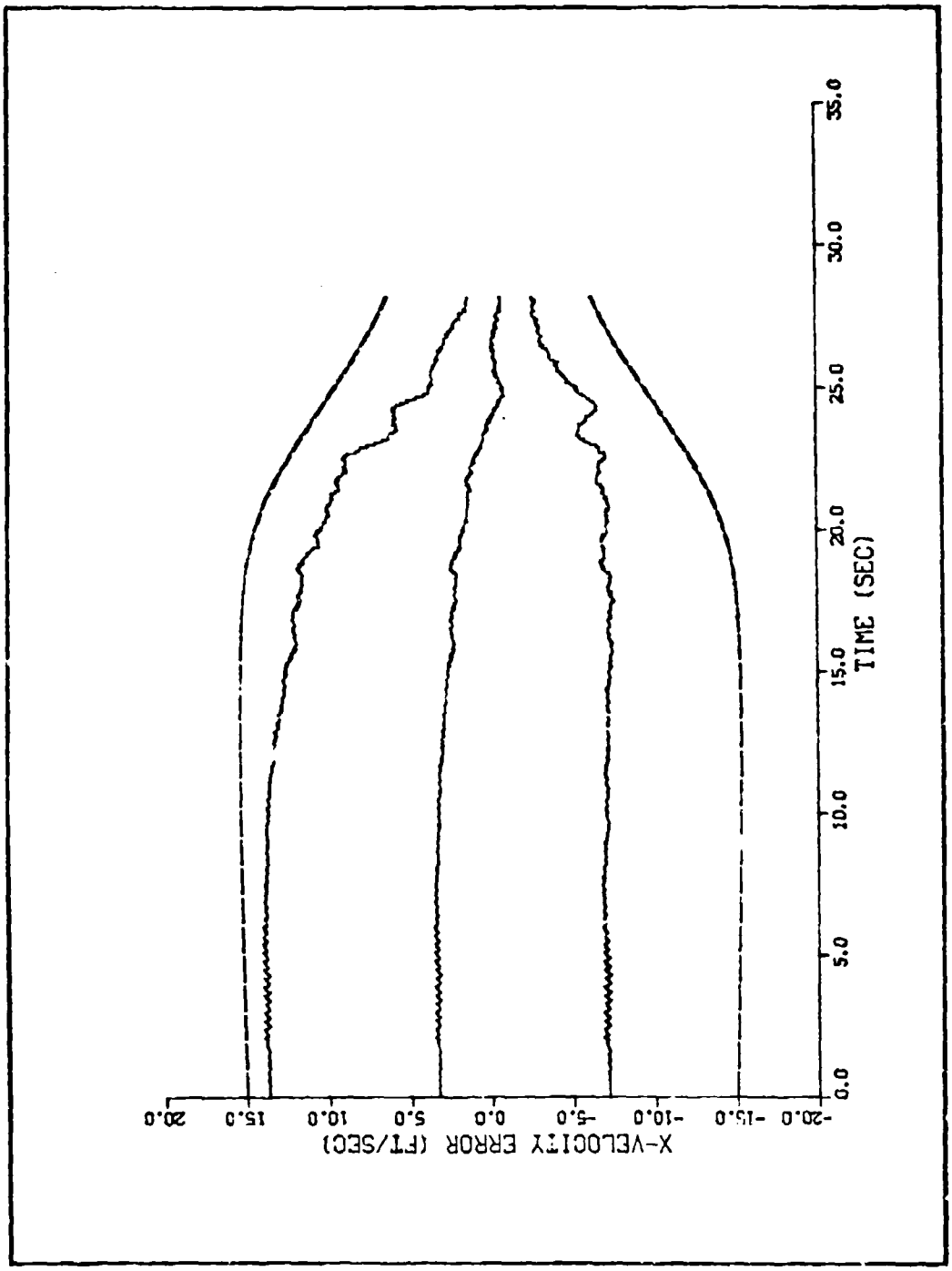

Figure D-2. Both Seekers Throughout Flight

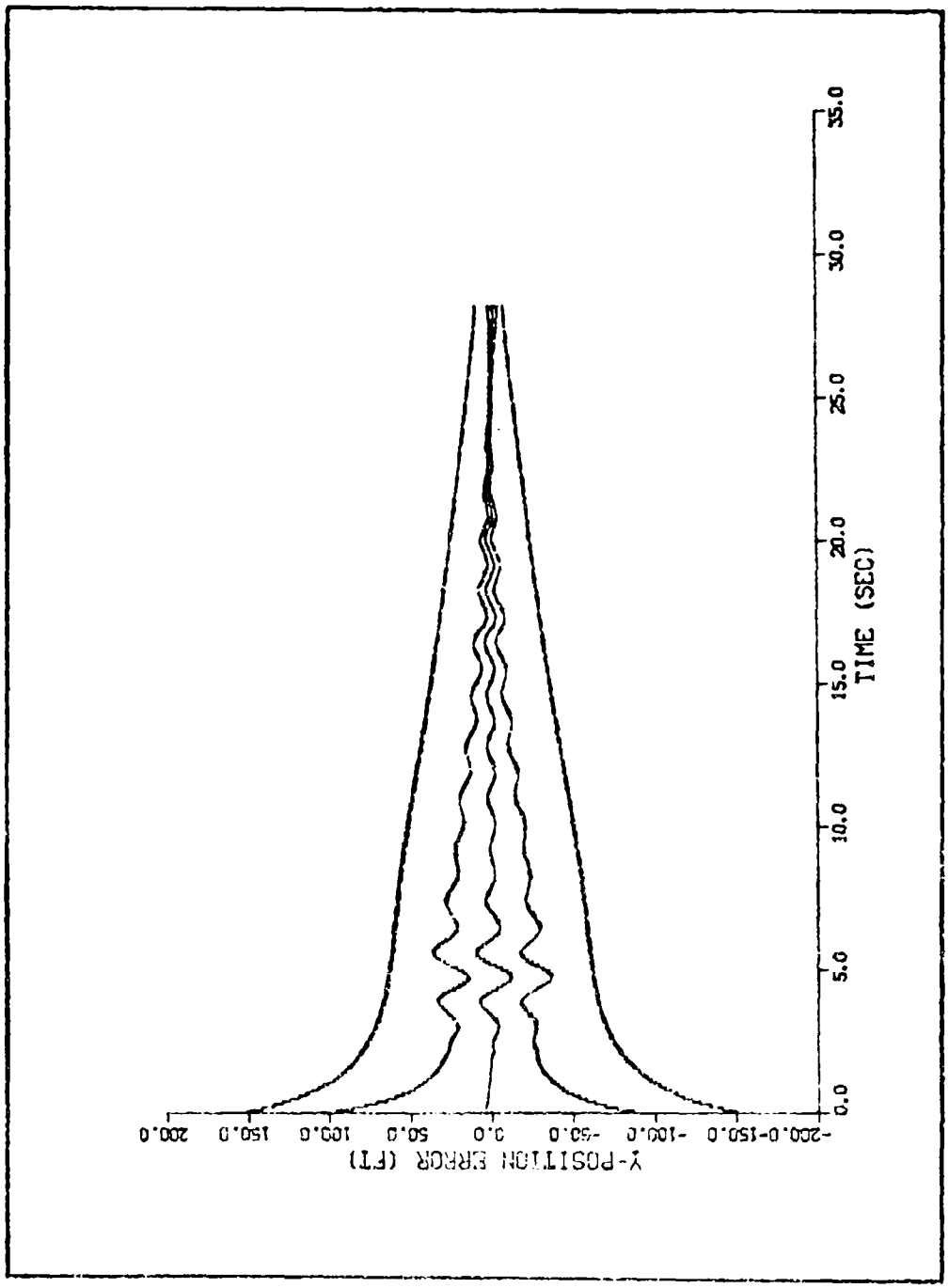

Figure D-3. Both Seekers Throughout Flight

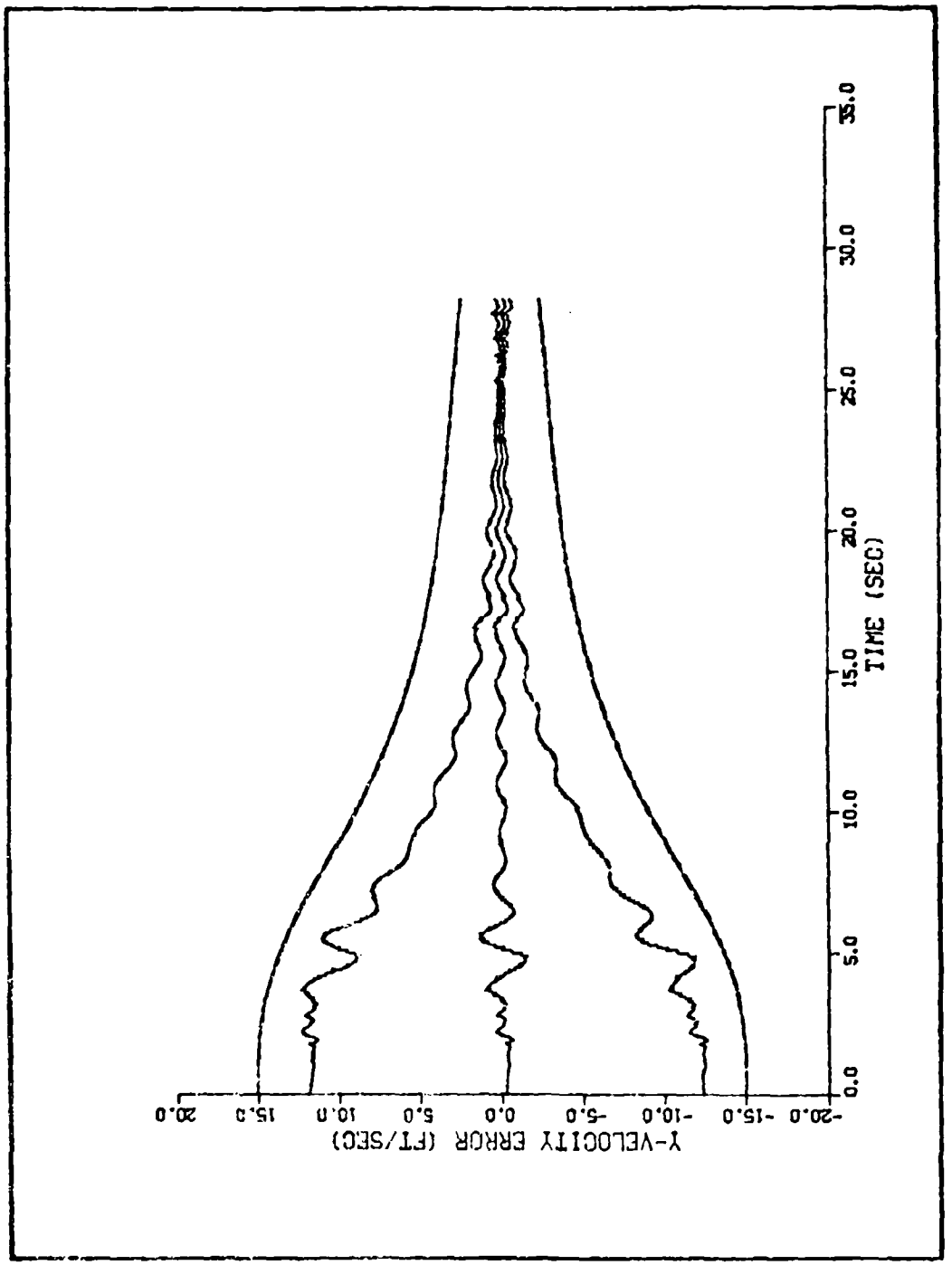

Figure D-4. Both Seekers Throughout Flight

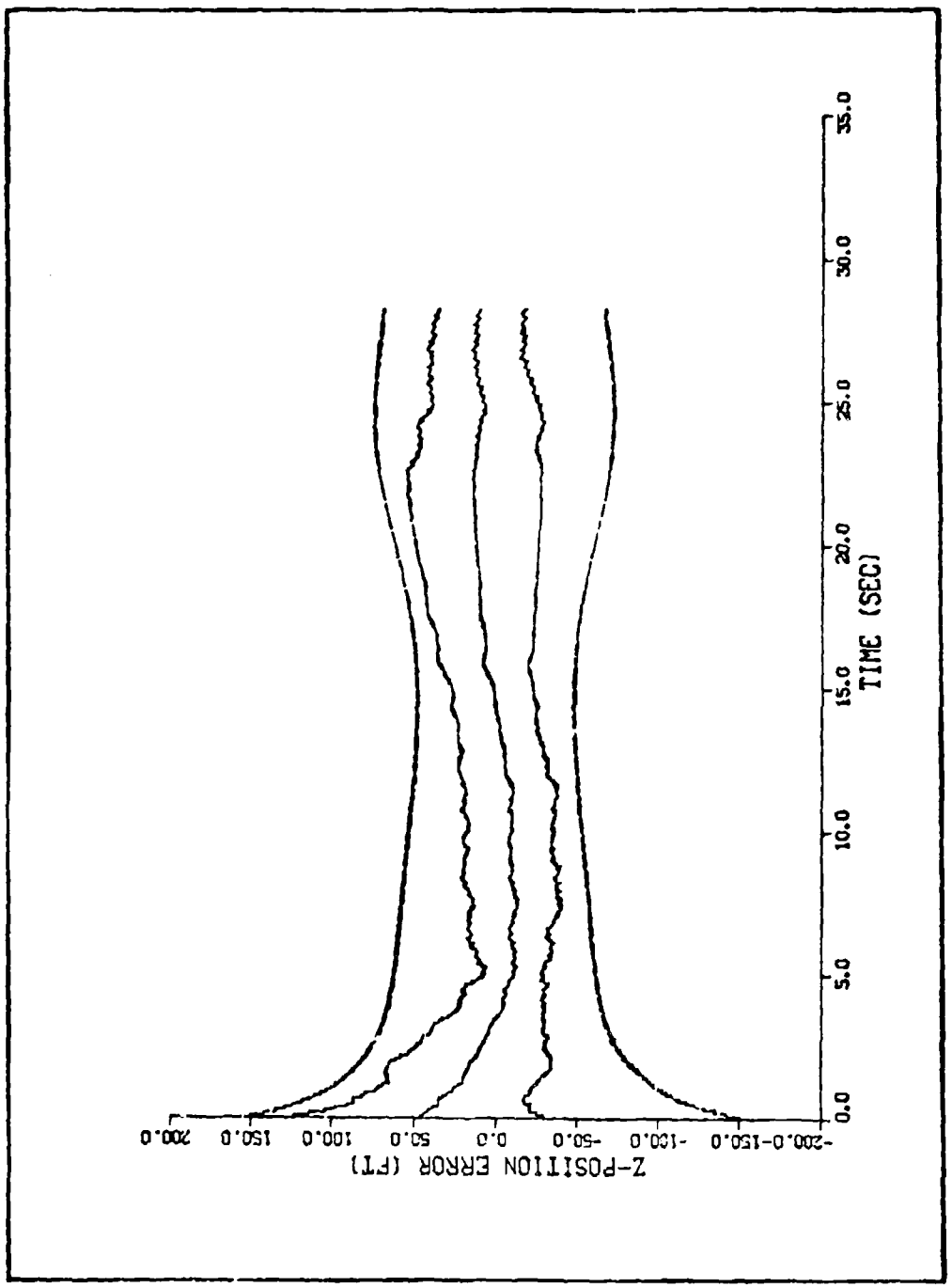

Figure D-5. Both Seekers Throughout Flight

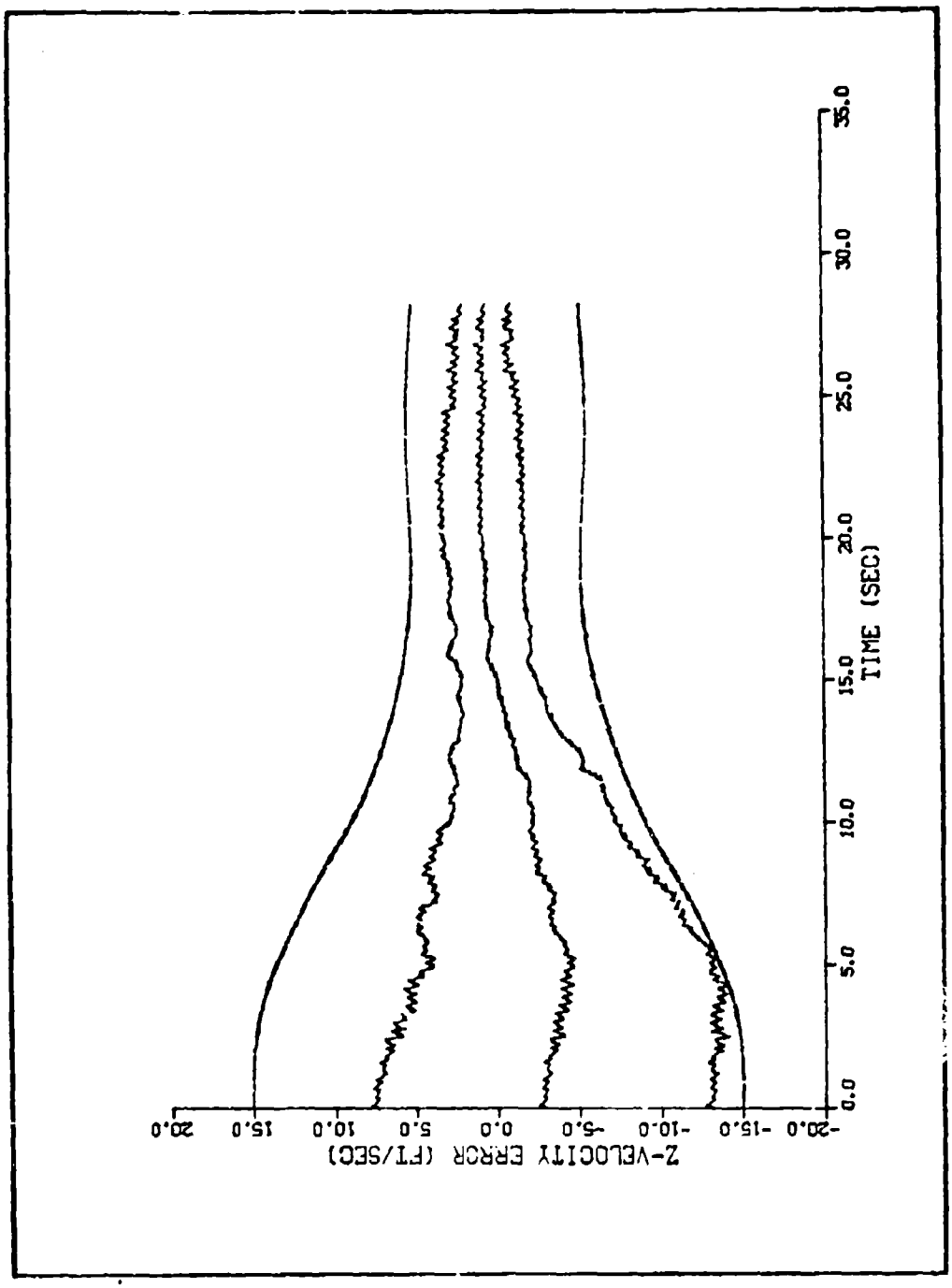

Figure D-6. Both Seekers Throughout Flight

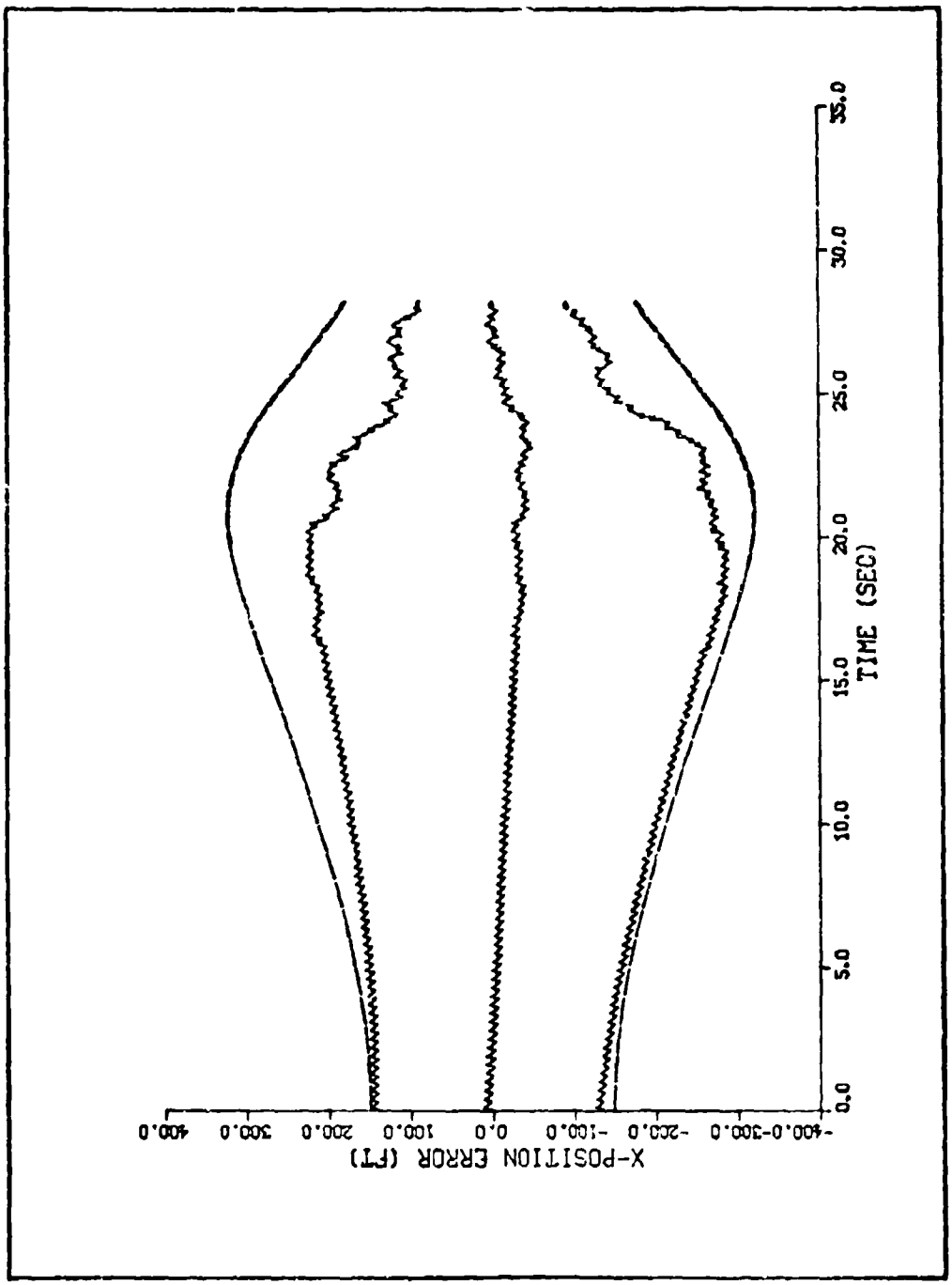

Figure D-7. Strapdown Only Initially, Switch to Gimballed at 16 sec

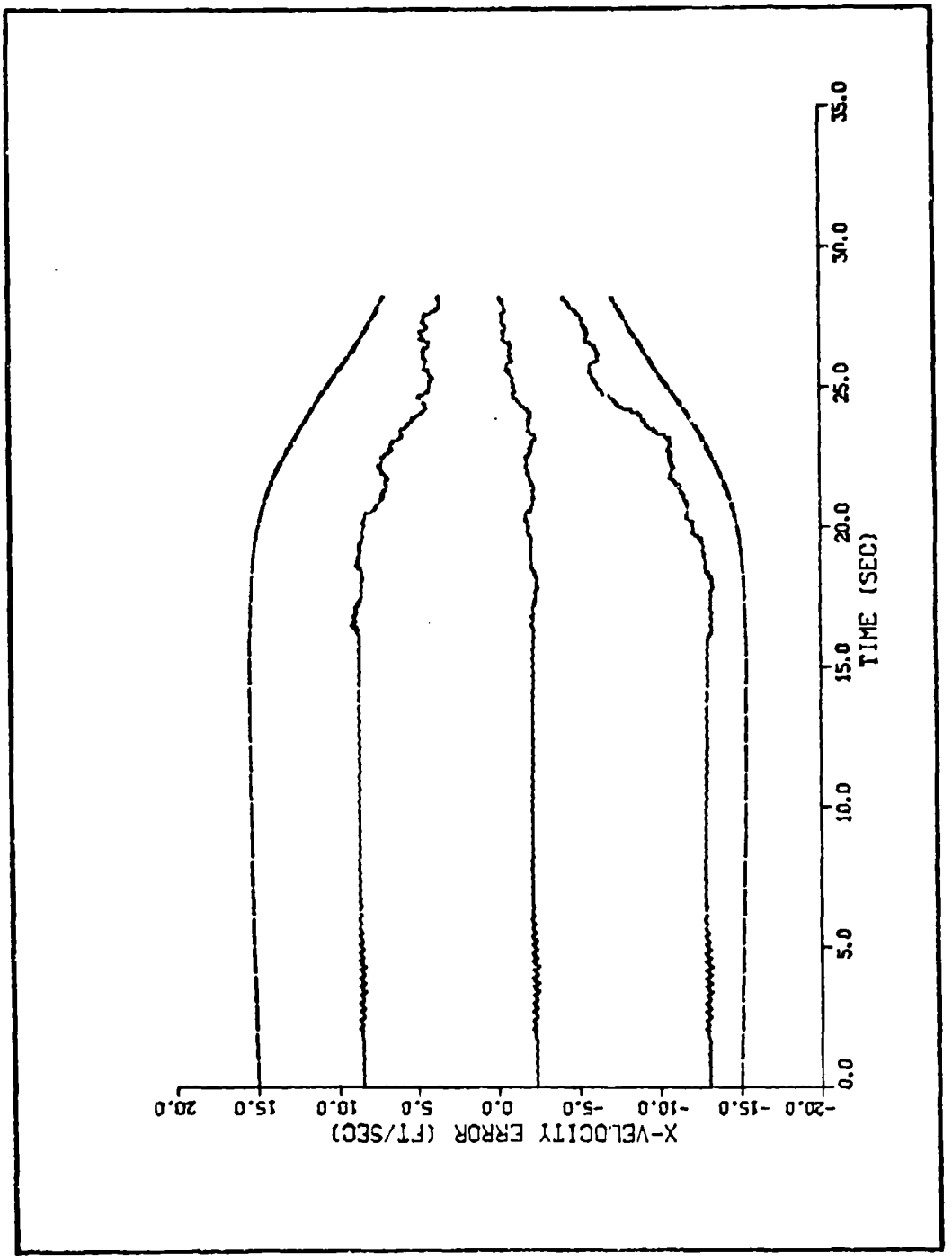

Figure D-8. Strapdown Only Initially, Switch to Gimballed at 16 sec

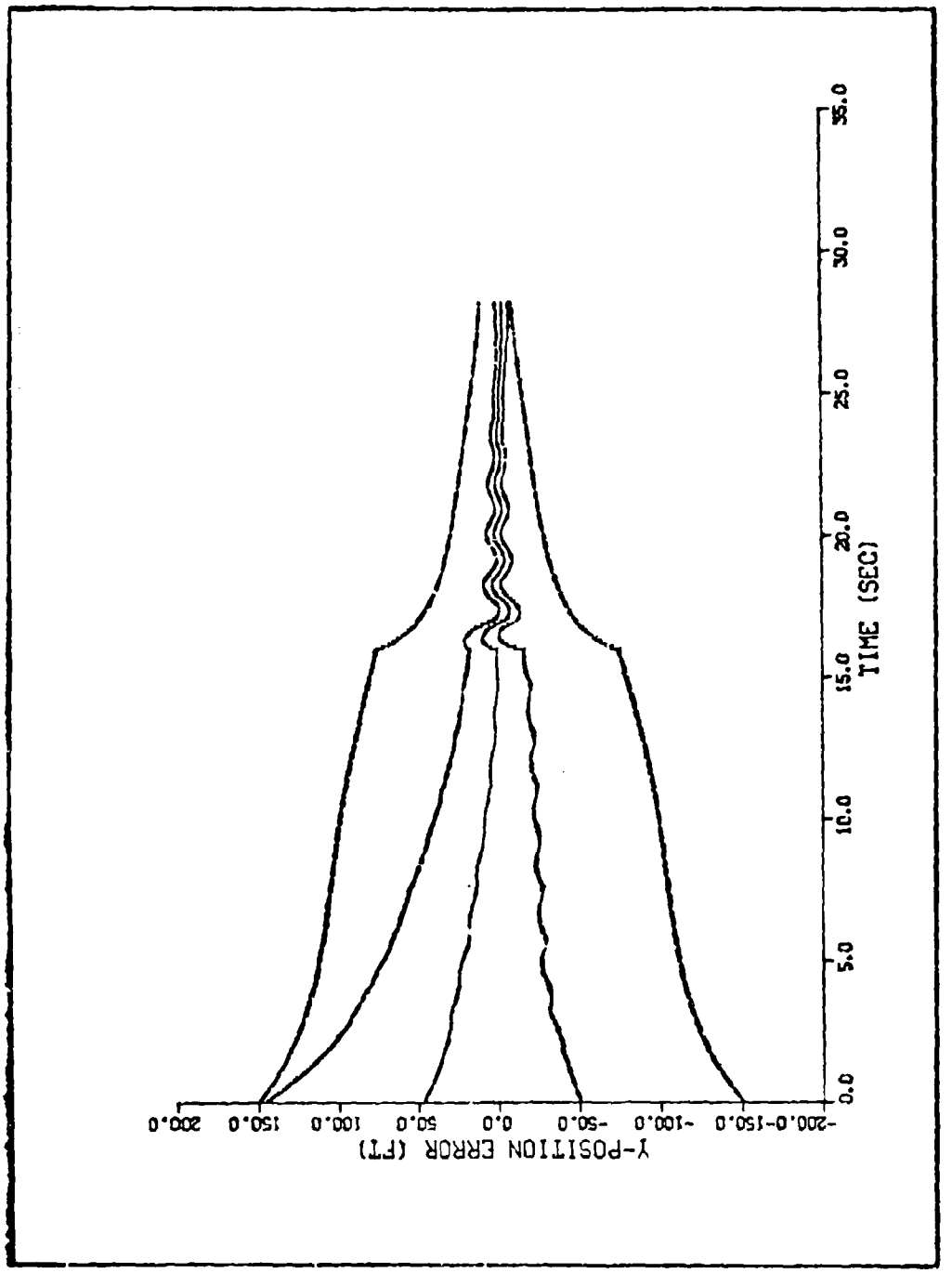

Figure D-9. Strapdown Only Initially, Switch to Gimballed at 16 sec

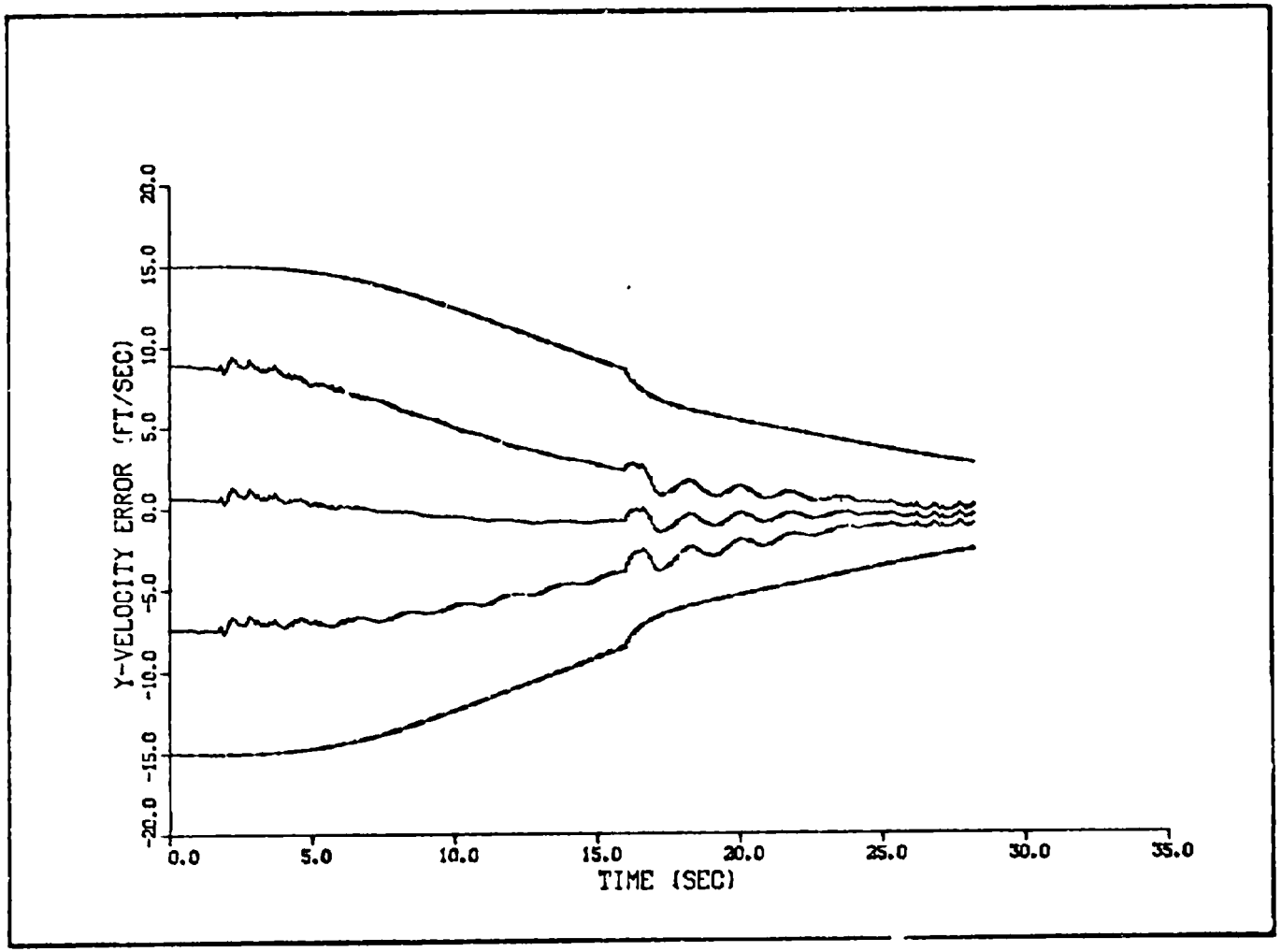

Figure D-10. Strapdown Only Initially, Switch to Gimballed at 16 sec

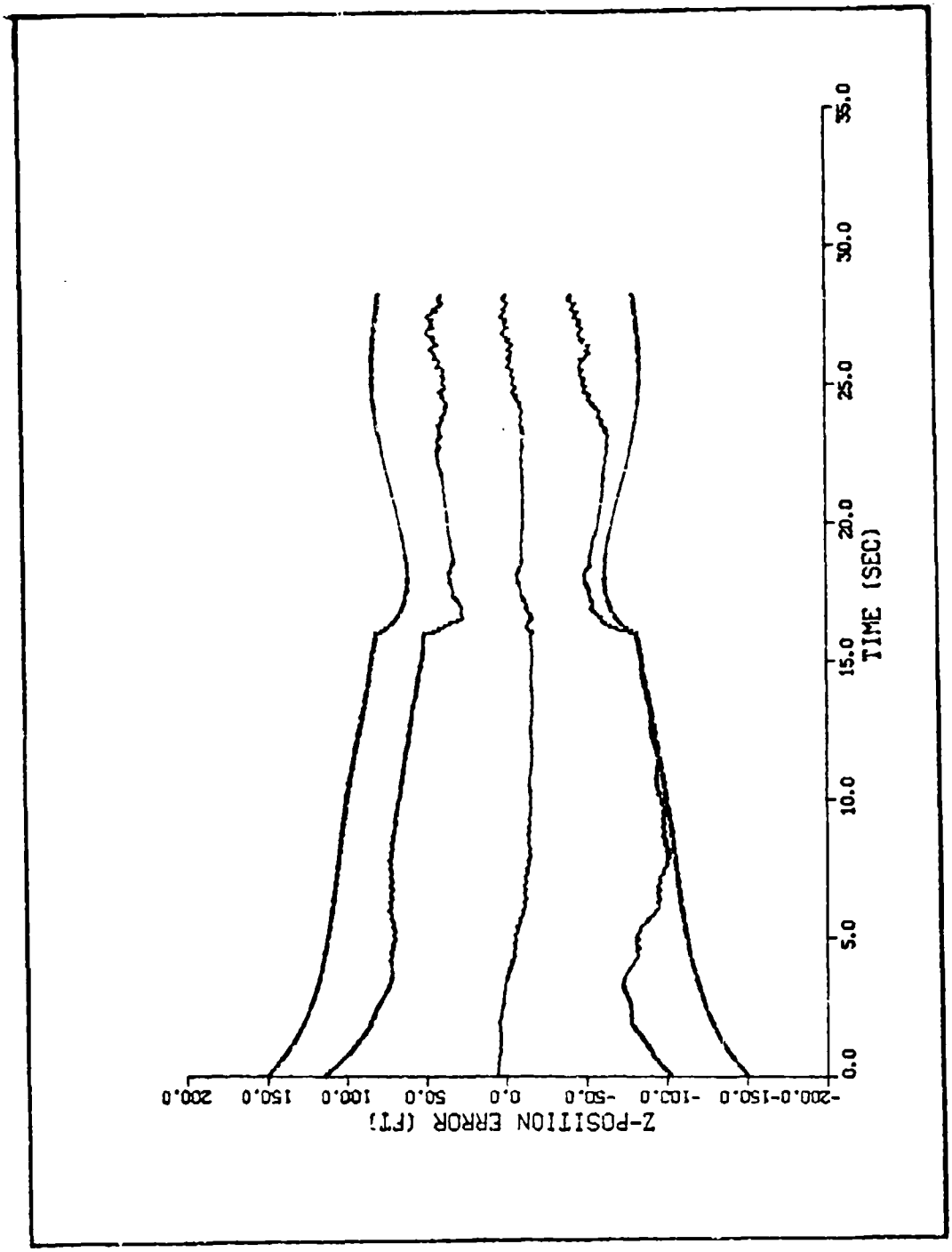

Figure D-11. Strapdown Only Initially, Switch to Gimballed at 16 sec

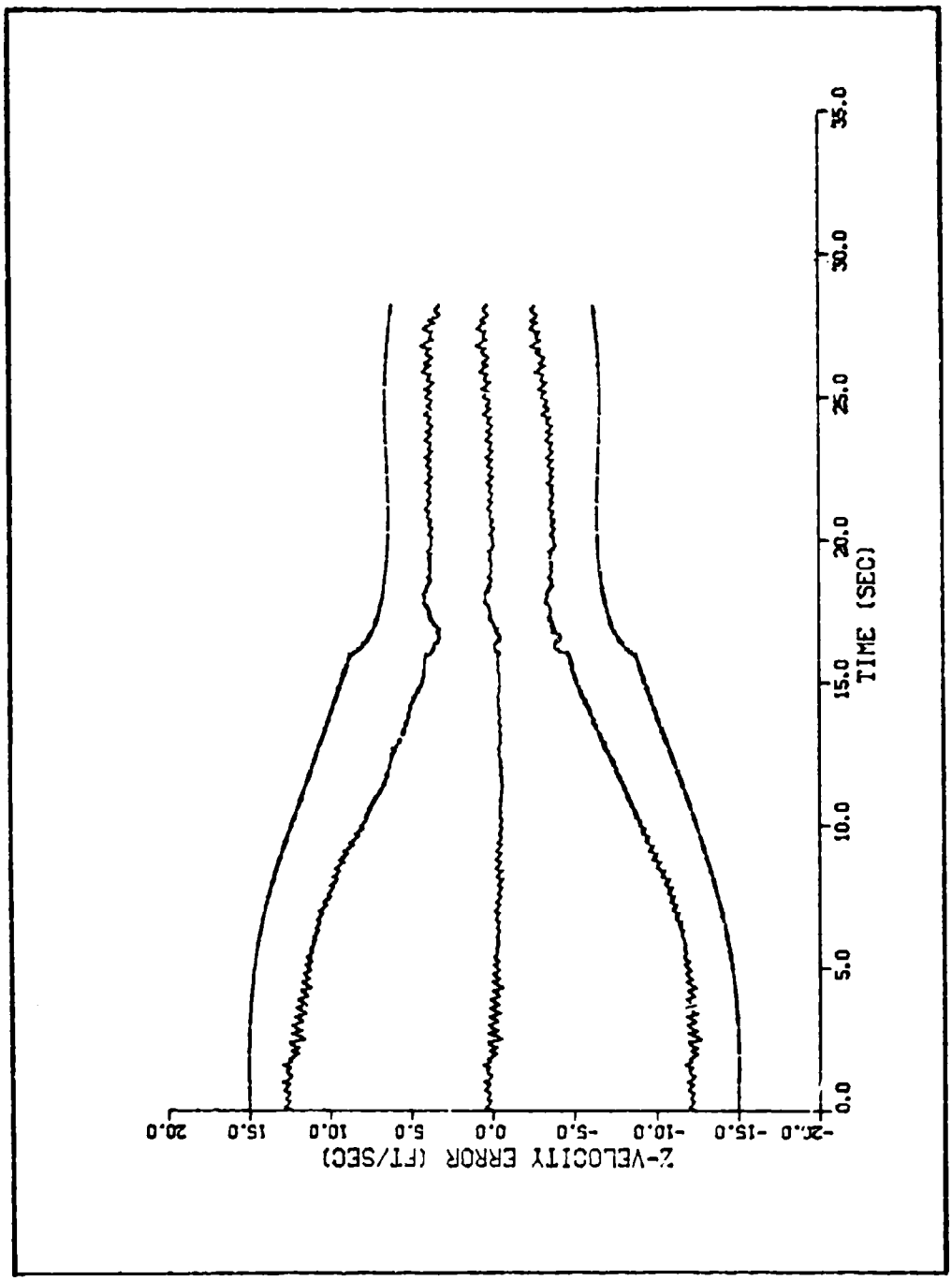

Figure D-12. Strapdown Only Initially, Switch to Gimballed at 16 sec

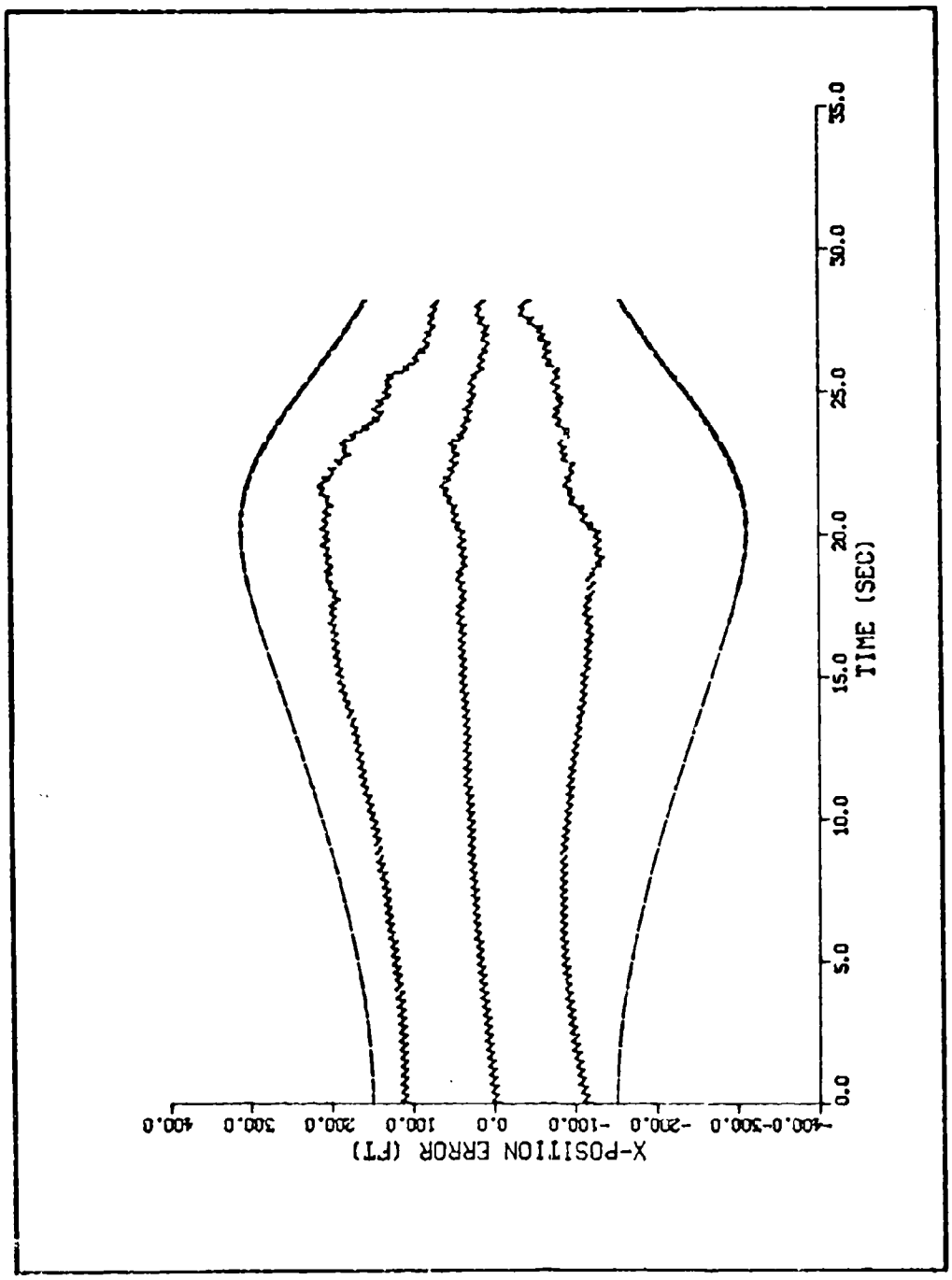

Figure D-13. Both Seekers Initially, Strapdown Off at 16 sec

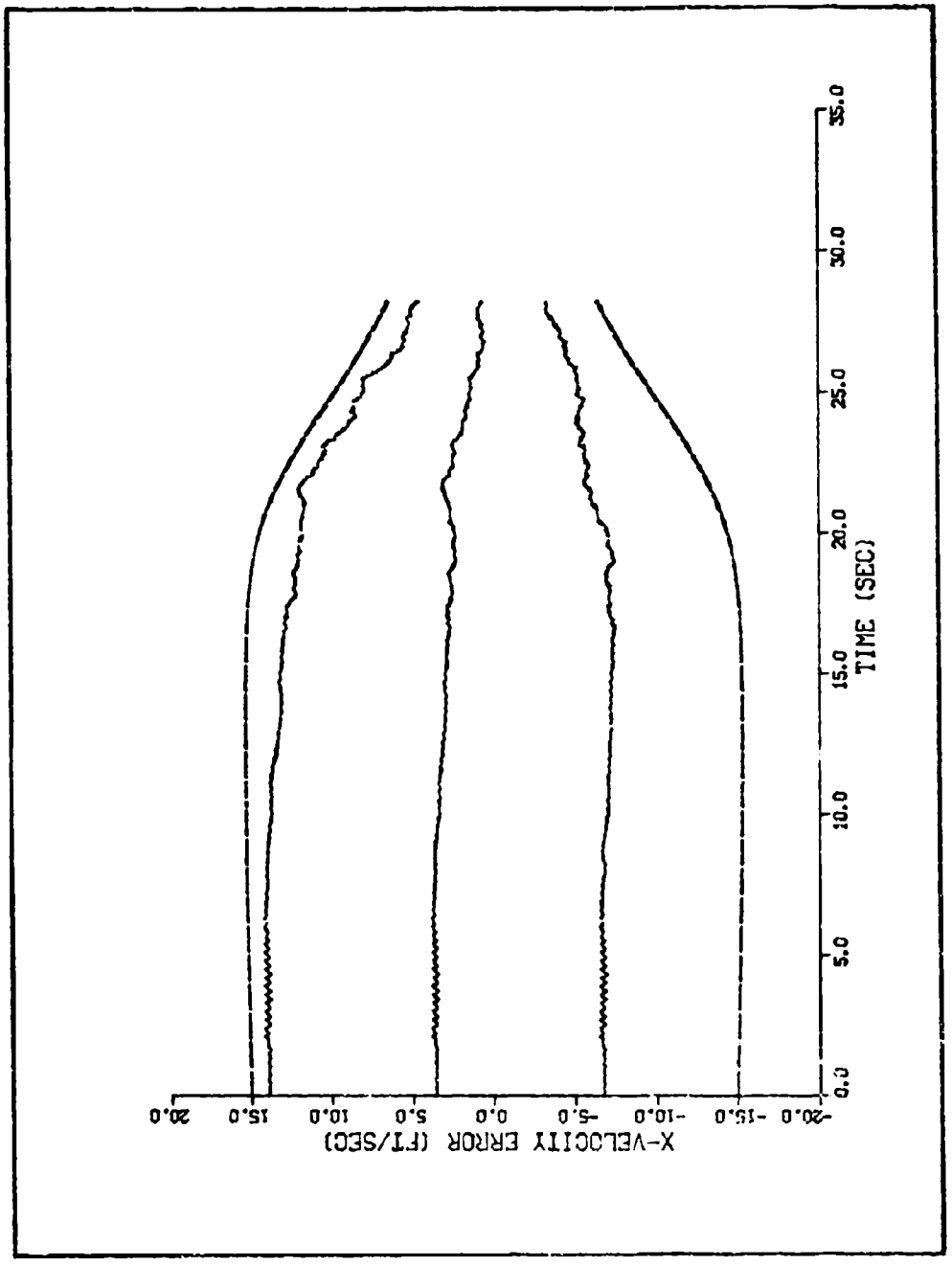

Figure D-14. Both Seekers Initially, Strapdown Off at 16 sec

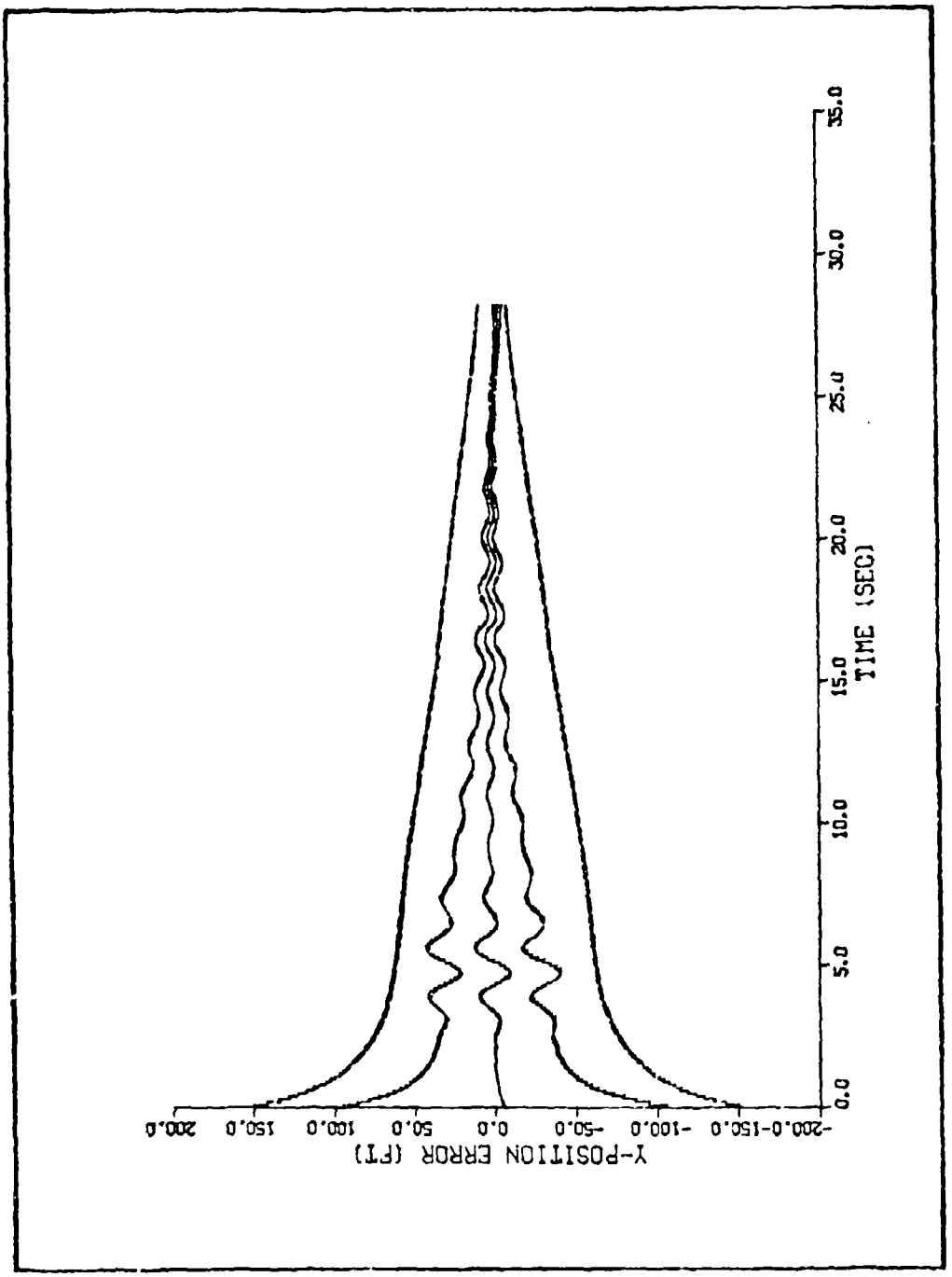

Figure D-15. Both Seekers Initially, Strapdown Off at 16 sec

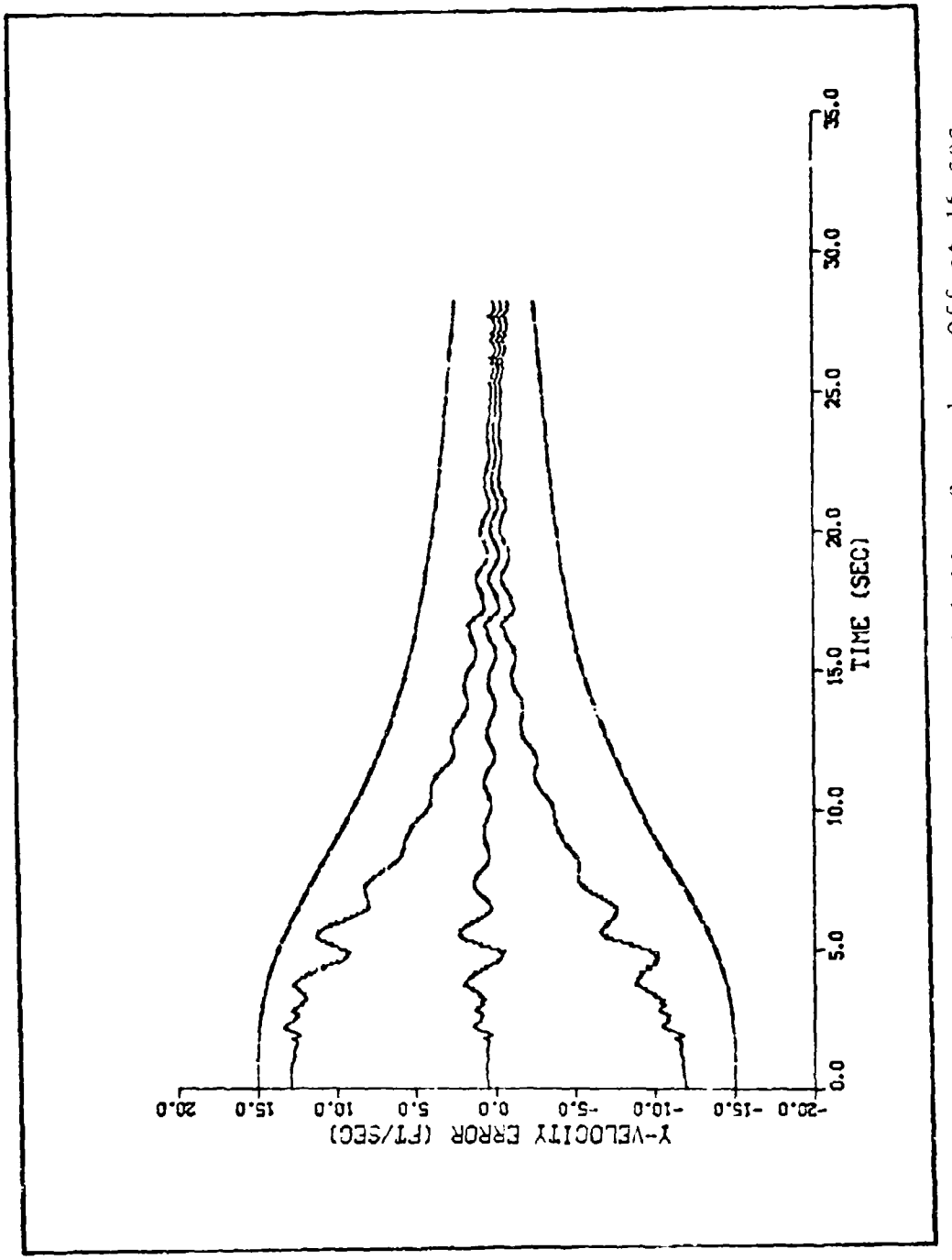

Figure D-16. Both Seekers Initially, Strapdown Off at 16 sec

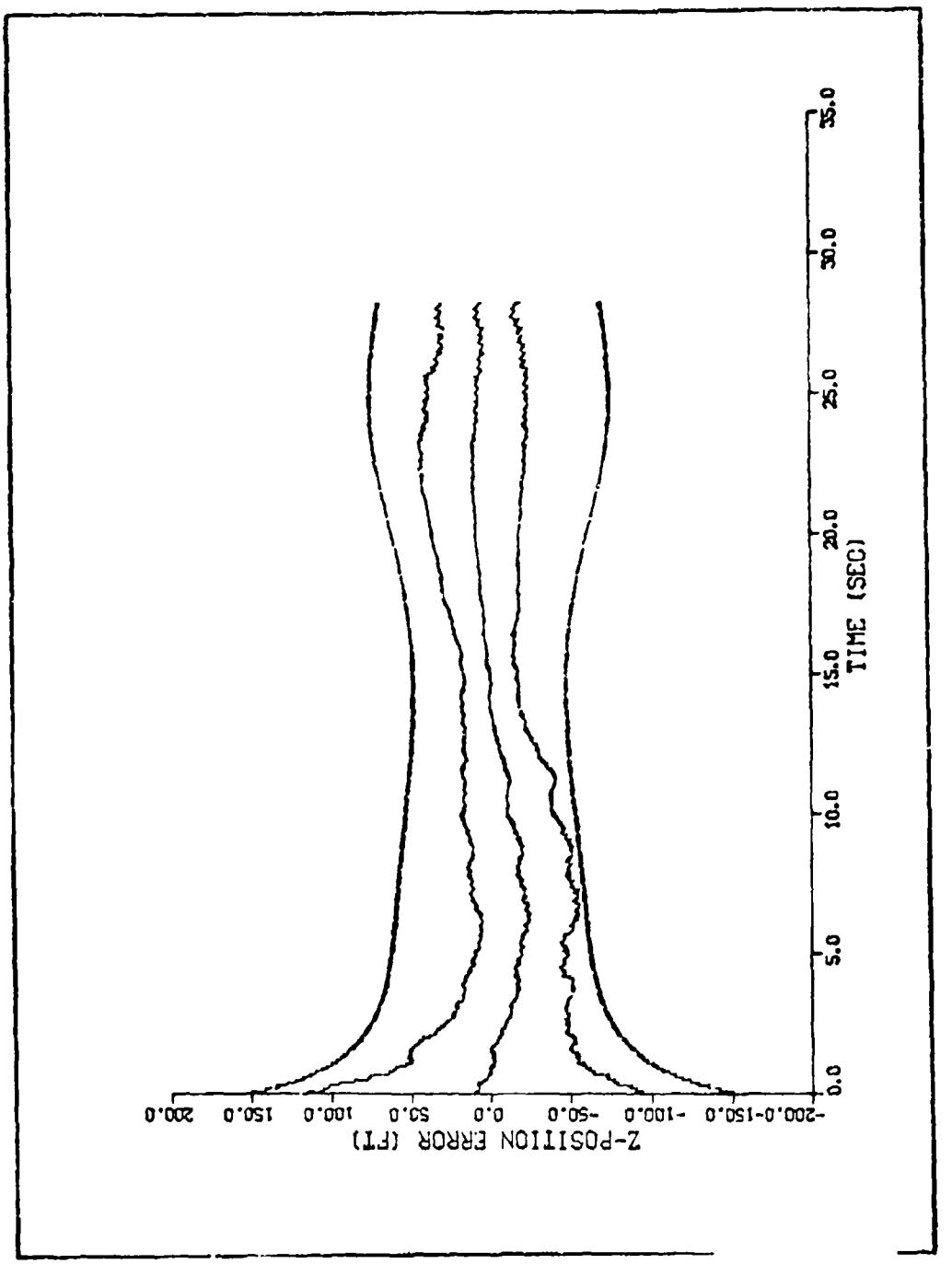

Figure D-17. Both Seekers Initially, Strapdown Off at 16 sec

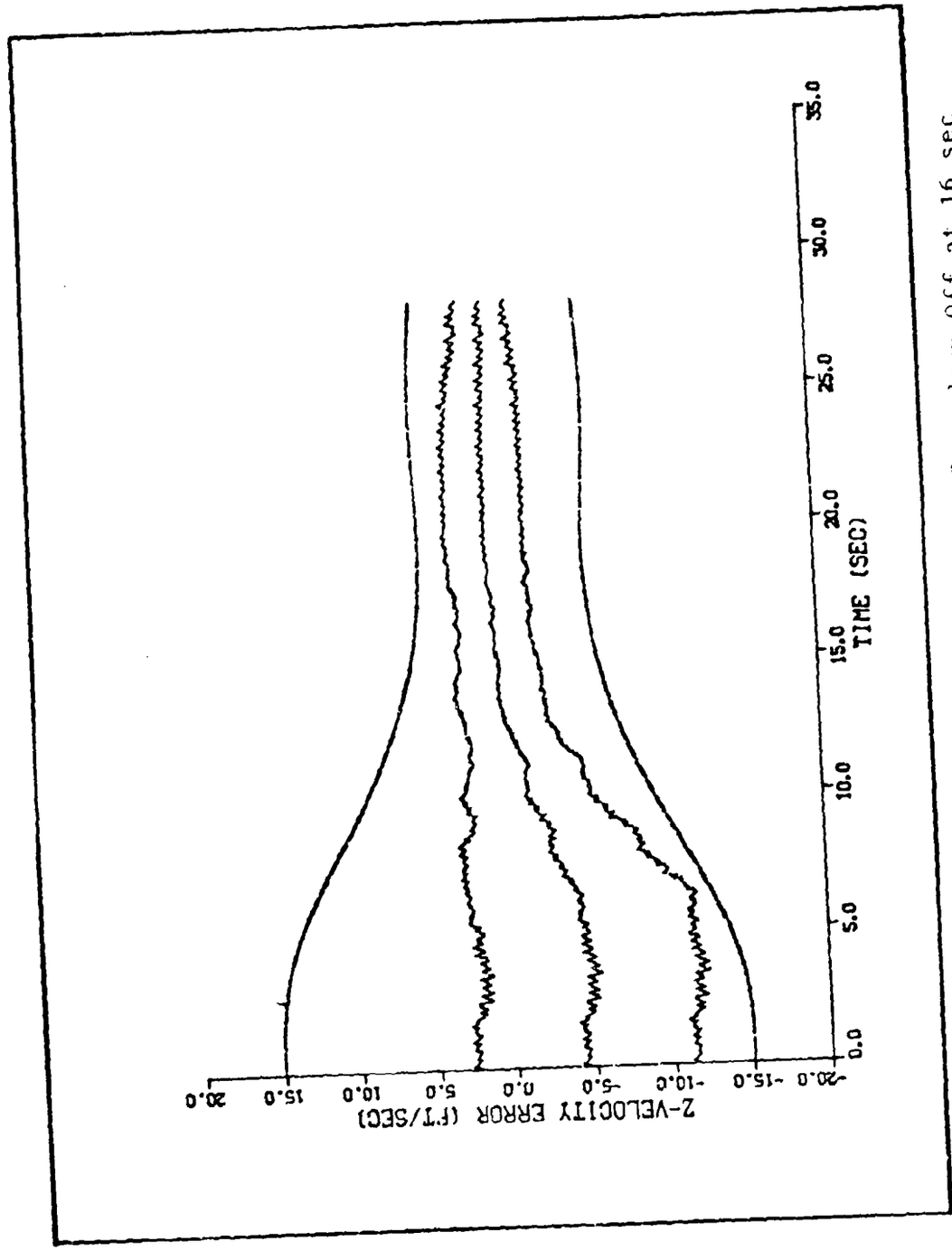

Figure D-18. Both Seekers Initially, Strapdown Off at 16 sec

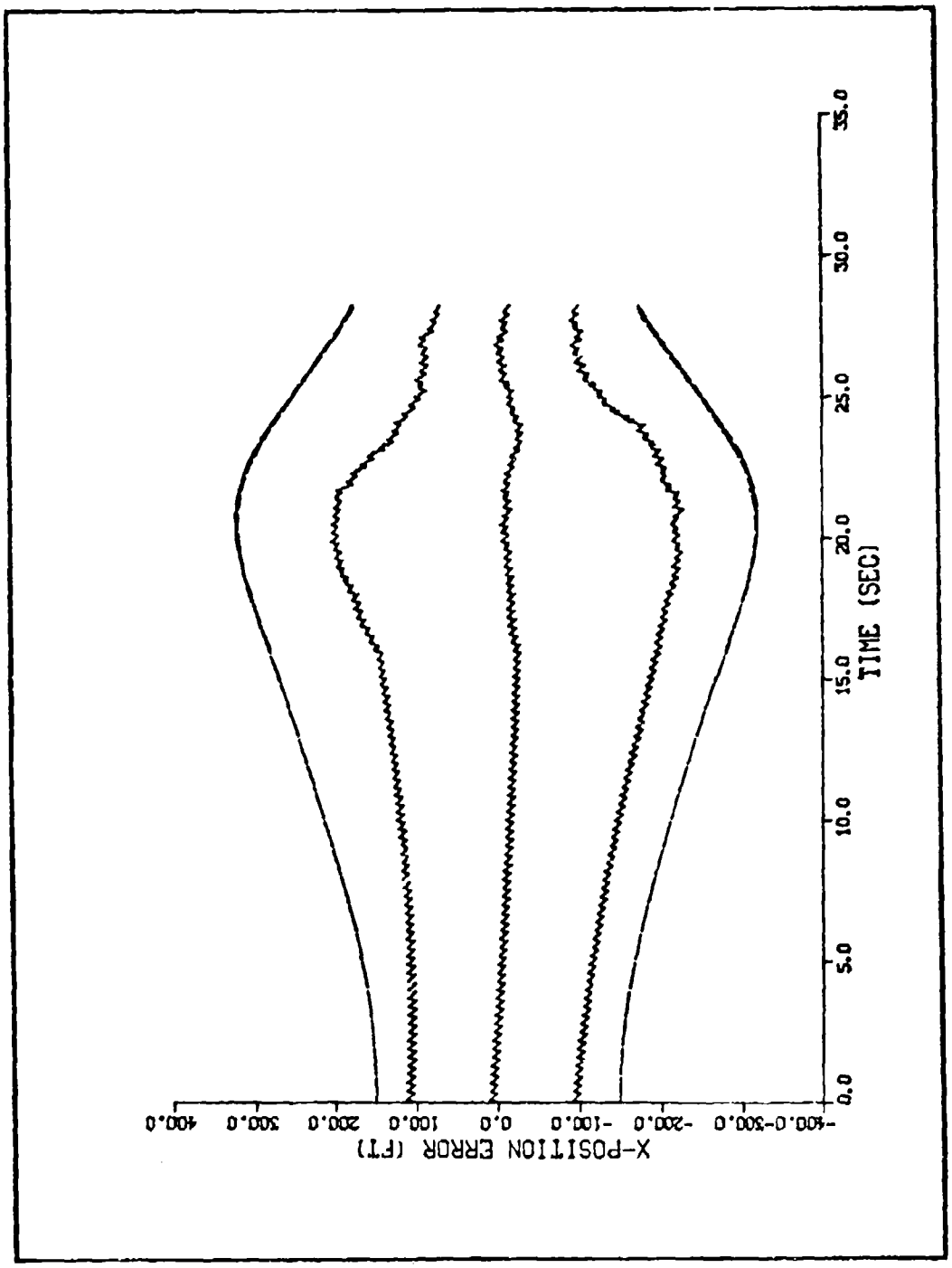

Figure D-19. Strapdown Only Initially, Gimballed On at 16 sec

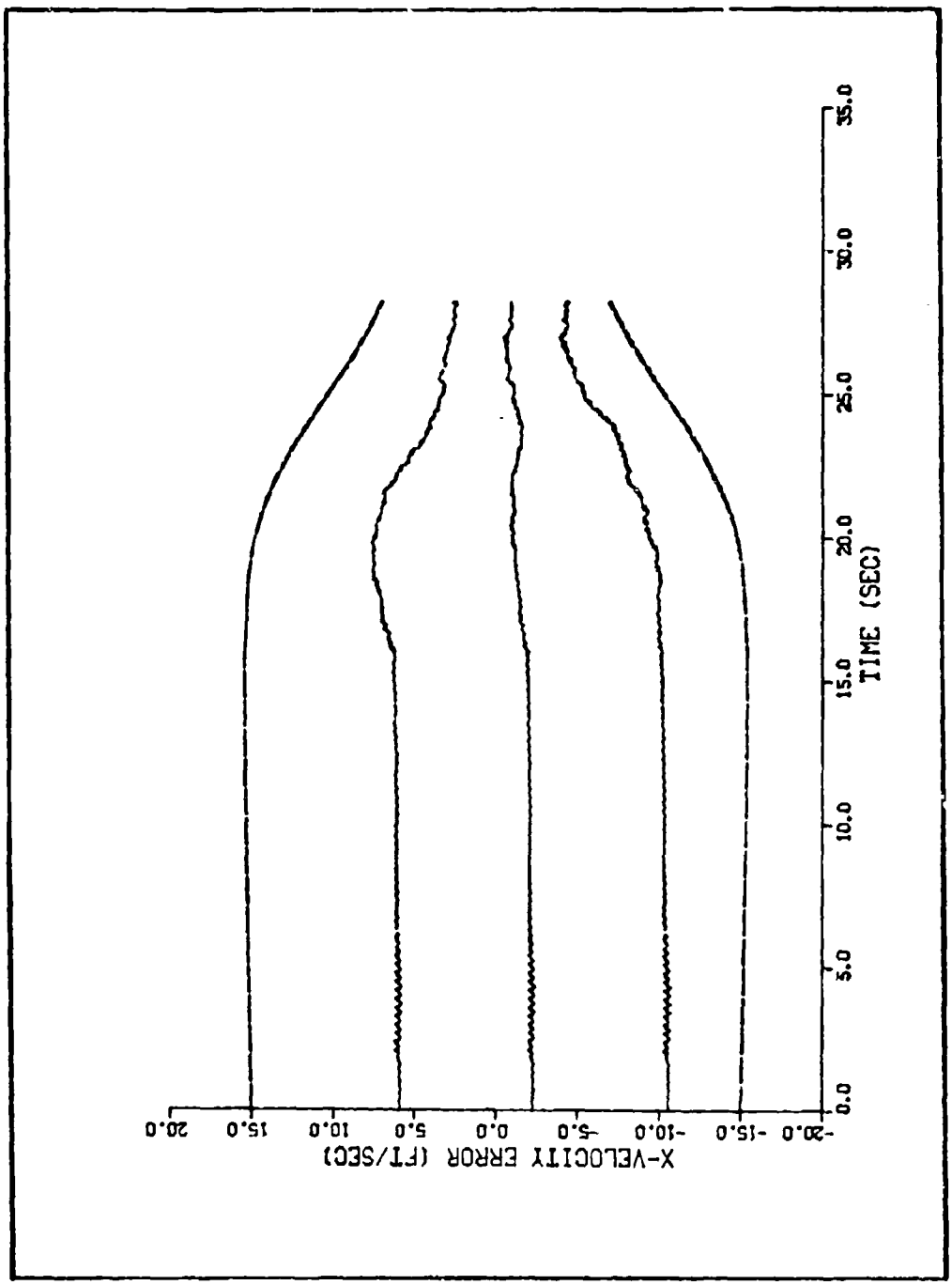

Figure D-20. Strapdown Only Initially, Gimballed On at 16 sec

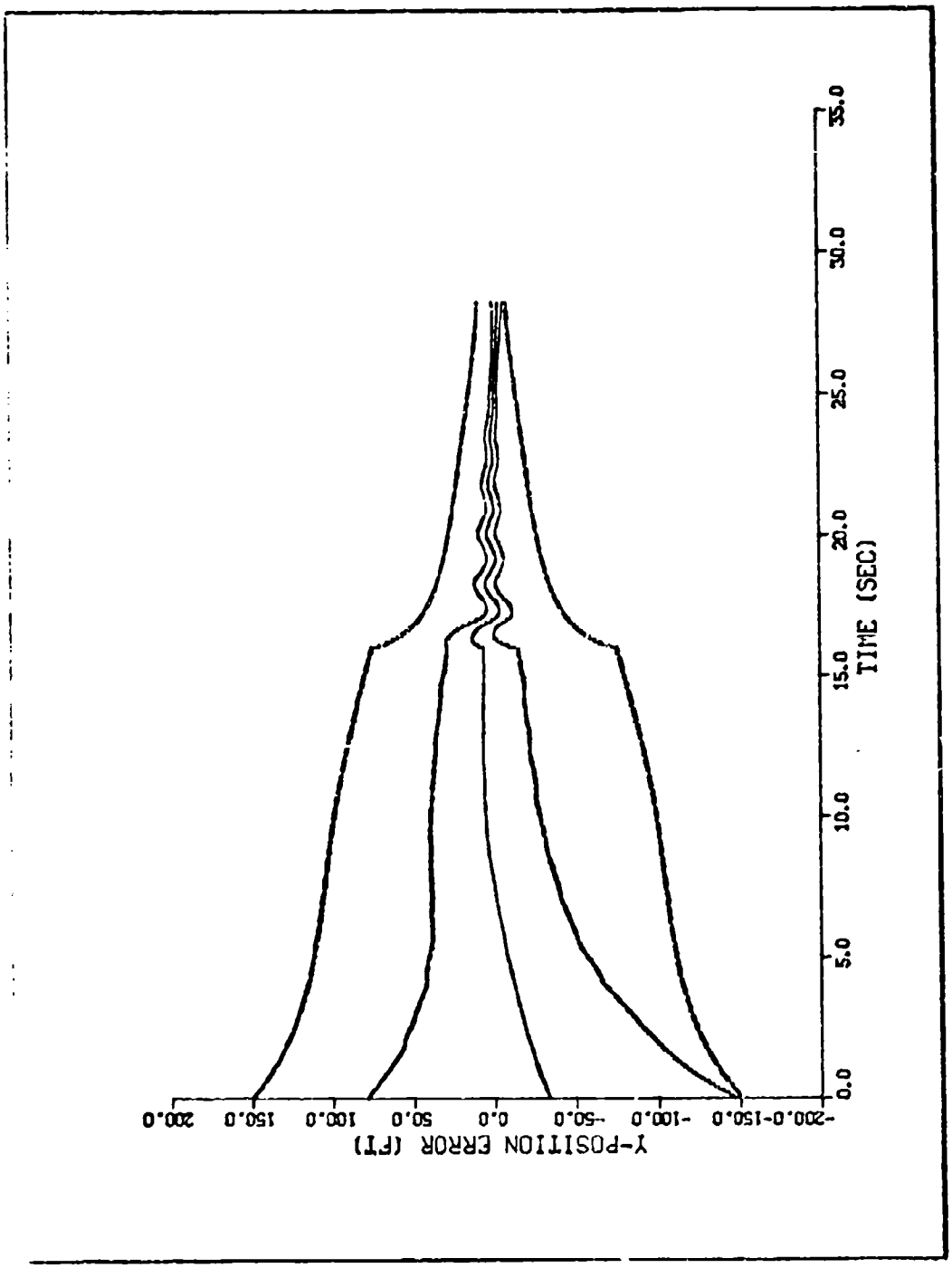

Figure D-21. Strapdown Only Initially, Gimballed On at 16 sec

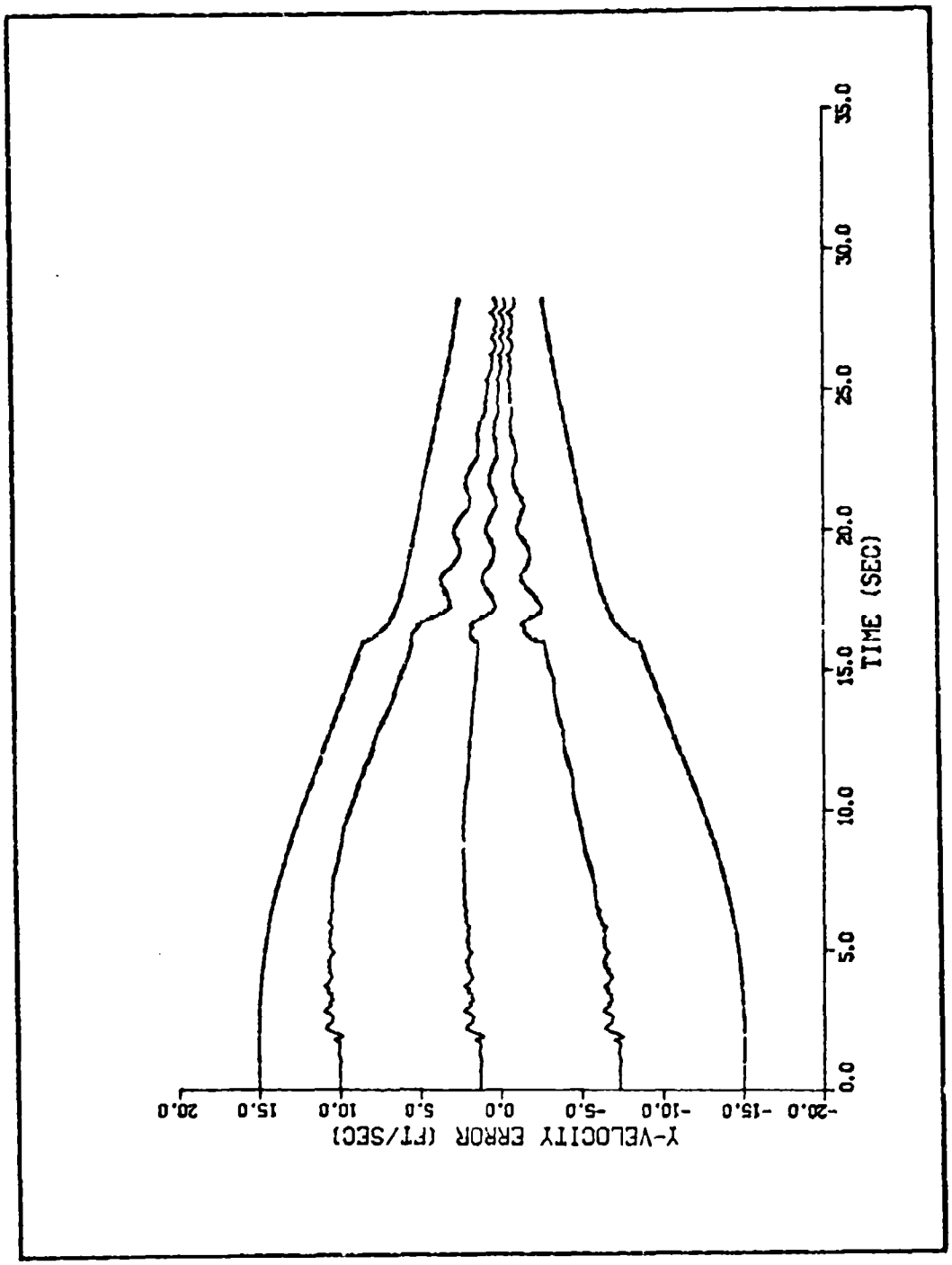

Figure D-22. Strapdown Only Initially, Gimballed On at 16 sec

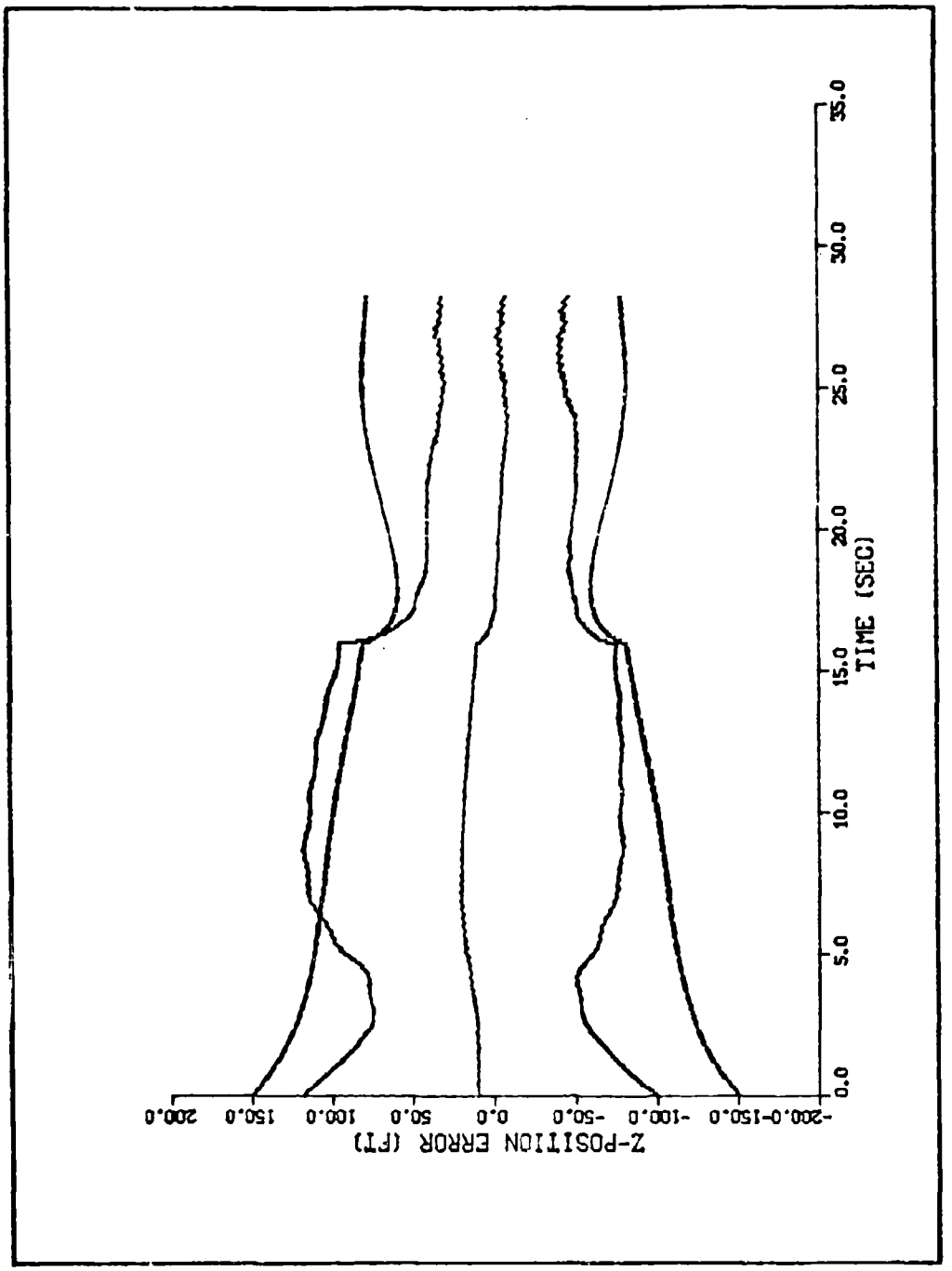

Figure D-23. Strapdown Only Initially, Gimballed On at 16 sec

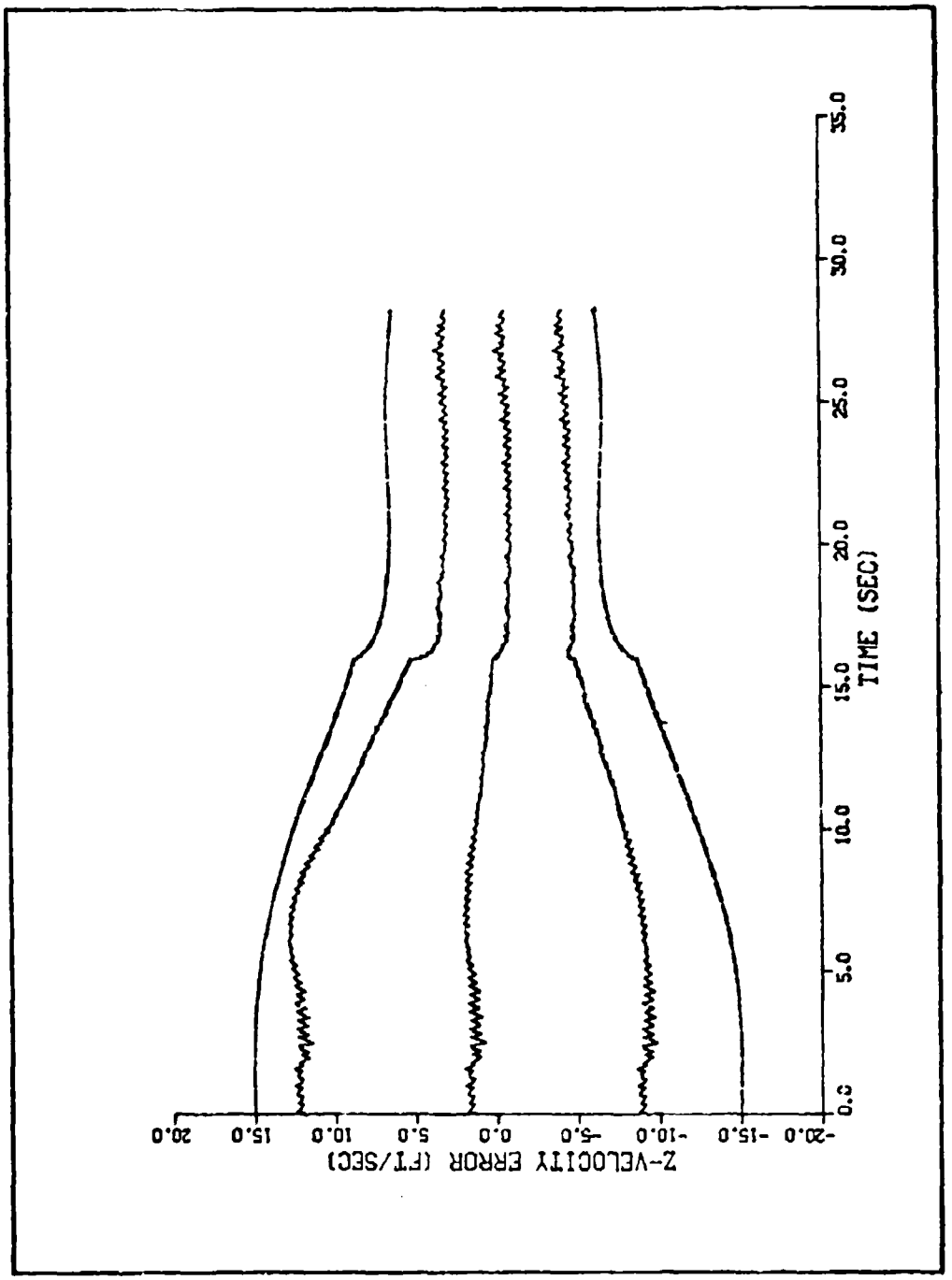

Figure D-24. Strapdown Only Initially, Gimballed On at 16 sec

VITA

Andrew C. Weston was born on 14 August 1959 in Chattanooga, Tennessee. He graduated from high school in Barnwell, South Carolina in 1977 and attended The Citadel, Charleston, South Carolina, from which he received the degree of Bachelor of Science in Electrical Engineering in May 1981. Upon graduation he received his commission and entered the School of Engineering, Air Force Institute of Technology in June 1981. His next assignment is with the Applications Branch of the Avionics Laboratory, Wright-Patterson Air Force Base. He is a member of IEEE and Tau Beta Pi.

Permanent address: 107 Woodlawn Avenue
Union, S. Carolina 29379

unclassified

SECURITY CLASSIFICATION OF THIS PAGE (When Data Entered)

REPORT DOCUMENTATION PAGE	READ INSTRUCTIONS BEFORE COMPLETING FORM
1. REPORT NUMBER: AFIT/GE/EE/82D-70	2. GOVT ACCESSION NO: A124723
3. RECIPIENT'S CATALOG NUMBER:	
4. TITLE (and Subtitle): DUAL-SEEKER MEASUREMENT PROCESSING FOR TACTICAL MISSILE GUIDANCE	5. TYPE OF REPORT & PERIOD COVERED: MS Thesis
	6. PERFORMING ORG. REPORT NUMBER:
7. AUTHOR(s): Andrew C. Weston, 2Lt USAF	8. CONTRACT OR GRANT NUMBER(s):
9. PERFORMING ORGANIZATION NAME AND ADDRESS: Air Force Institute of Technology (AFIT-EN) Wright-Patterson AFB, Ohio 45433	10. PROGRAM ELEMENT, PROJECT, TASK AREA & WORK UNIT NUMBERS:
11. CONTROLLING OFFICE NAME AND ADDRESS: Terminal Guidance Group, Armament Laboratory Eglin AFB, Florida 32542	12. REPORT DATE: December 1982
	13. NUMBER OF PAGES: 172
14. MONITORING AGENCY NAME & ADDRESS (if different from Controlling Office):	15. SECURITY CLASS. (of this report): Unclassified
	15a. DECLASSIFICATION DOWNGRADING SCHEDULE:

16. DISTRIBUTION STATEMENT (of this Report)

Approved for public release; distribution unlimited

17. DISTRIBUTION STATEMENT (of the abstract entered in Block 20, if different from Report)

18. SUPPLEMENTARY NOTES

Approved for public release: IAW AFR 190-17.

LYNN E. WOLAVER
Dean for Research and Professional Development
Air Force Institute of Technology (ATC)
Wright-Patterson AFB OH 45433

19 JAN 1983

19. KEY WORDS (Continue on reverse side if necessary and identify by block number)

Air-to-Ground Tracking	Gimballed Seeker
Dual-Seeker	Kalman Filter
Strapdown Seeker	Air-to-Ground Missile

20. ABSTRACT (Continue on reverse side if necessary and identify by block number)

The available measurements from a strapdown seeker and a gimballed seeker onboard an air-to-ground anti-radiation missile are analyzed through an extended Kalman filter simulation. Detailed models of both seekers are developed. Only angular measurements are assumed available from the seekers: angle measurements from the strapdown seeker and

DD FORM 1 JAN 73 1473 EDITION OF 1 NOV 65 IS OBSOLETE

unclassified

SECURITY CLASSIFICATION OF THIS PAGE (When Data Entered)

20. angle and angle-rate measurements from the gimballed seeker. A 6-state extended Kalman filter model is used to estimate the ground target's position and relative velocity using the seekers' measurements. Four measurement policies are compared to analyze use of the gimballed seeker early in the missile flight and loss of the strapdown seeker in midflight.

The results revealed an observability problem in one channel of the filter, that along the range vector. Analyses were made only by comparisons of performance in the other two channels. The comparisons showed insignificant degradation to filter performance through loss of the strapdown seeker at midflight, and substantial benefit from use of the gimballed seeker as early as possible in the flight.